THE UNIVERSITY OF CHICAGO

ERBIUM-ION INTEGRATION WITH SILICON PHOTONICS FOR QUANTUM MEMORY TECHNOLOGIES

A DISSERTATION SUBMITTED TO
THE FACULTY OF THE PRITZKER SCHOOL OF MOLECULAR ENGINEERING
IN CANDIDACY FOR THE DEGREE OF
DOCTOR OF PHILOSOPHY

BY
CHENG JI

CHICAGO, ILLINOIS
JUNE 2025

To my family

"The truth always turns out to be simpler than you thought"

– Richard Philip Feynman

TABLE OF CONTENTS

LIST OF FIGURES . . . viii

LIST OF TABLES . . . x

ACKNOWLEDGMENTS . . . xi

ABSTRACT . . . xiii

1 INTRODUCTION . . . 1
  1.1 Quantum Communication: Building the Network for Quantum Computers . 1
    1.1.1 The Necessity and Challenges of Quantum Communication . . . 1
    1.1.2 Quantum Repeaters with Quantum Memory: A Solution for Long-Distance Communication . . . 2
  1.2 Extending Entanglement Through Memory-Assisted Networks with Quantum Repeater . . . 4
  1.3 Rare Earth Ions: A Promising Platform for Long-Coherence Quantum Memory 7
    1.3.1 Why Rare Earth Ions Are Well-Suited for Quantum Memory . . . 7
    1.3.2 Erbium: A Telecom-Compatible Rare Earth Ion for Quantum Memory 9
  1.4 Selecting Erbium-Doped Host Materials for Quantum Memory Applications . 10
  1.5 Comparative Analysis with Other Research on Erbium based Quantum Memory 11
  1.6 Scope and Structure of This Thesis . . . 14

2 DEPOSITION TECHNIQUES FOR ERBIUM-DOPED THIN FILMS: THE FOUNDATION FOR QUANTUM MEMORY . . . 18
  2.1 Unlocking Atomic Layer Deposition (ALD): A Key Tool for Precise Thin Film Growth . . . 19
  2.2 Engineering Erbium-Doped TiO_2 Thin Films Using ALD . . . 21
  2.3 Characterization of Erbium-Doped Thin Films Deposited via ALD . . . 23
    2.3.1 Surface Roughness and Morphology . . . 24
    2.3.2 Wafer Scale Uniformity . . . 25
    2.3.3 Erbium Doping Concentration . . . 25
    2.3.4 Crystallinity and Phase Stability . . . 30
  2.4 Probing Optical Properties: Photoluminescence Excitation (PLE) Measurements of Er Emitters in the Thin Film . . . 34
  2.5 Concluding Remarks Regarding Thin-Film Deposition . . . 39

3 PHOTONIC CRYSTAL CAVITIES INTEGRATION: ADVANCING SCALABLE QUANTUM PHOTONIC PLATFORMS . . . 41
  3.1 Physics behind Photonics Cavity – an Overview of Cavity Quantum Electrodynamics (QEDs) . . . 41
  3.2 Photonics Design and Simulation for Quantum Memory . . . 45
    3.2.1 The Photonic Crystal Cavity Design and Simulation . . . 45

    - 3.2.2 The Waveguide to Fiber Coupling Design and Simulation 47
  - 3.3 Photonic Crystal Cavity Fabrication and Integration: Realizing Quantum Memory in Scalable Photonic Devices 50
  - 3.4 Concluding Remarks of Cavity Design and Fabrication 53

- 4 OPTICAL MEASUREMENT OF INTEGRATED PHOTONIC DEVICES: PROBING QUANTUM MEMORY EMITTERS 54
  - 4.1 Nanocavity-mediated Purcell Enhancement of ALD of Er:TiO_2 Thin Films . 55
    - 4.1.1 Optical setup for photonic device measurements 55
    - 4.1.2 Cavity Benchmark 56
    - 4.1.3 Spectral Diffusion Linewidth Measurement through TSHB 57
    - 4.1.4 Optical lifetime and Purcell Enhancement 61
    - 4.1.5 Conclusion of this section 62
  - 4.2 Anomalous Purcell Decay of Strongly Driven Inhomogeneous Emitters Coupled to a Cavity 63
    - 4.2.1 Photonic Cavity and Waveguide Characterization 63
    - 4.2.2 PLE measurements 64
    - 4.2.3 Anomalous Purcell Double-peak Decay 65
    - 4.2.4 Conclusion of This Section 67

- 5 ISOLATING A SINGLE ERBIUM ION: THE INITIAL STEP FOR QUANTUM MEMORY QUBIT READOUT 69
  - 5.1 Materials and Devices Preparation 69
  - 5.2 Optical Emission and Lifetime Dynamics 71
  - 5.3 Isolated Single Ion Emission Analysis 73
  - 5.4 Single Photon Linewidth Characterization 73
  - 5.5 Concluding Remarks of This Chapter 74

- 6 EXPLORING DYNAMIC QUENCHING IN SINGLE-PHOTON AVALANCHE PHOTODETECTORS: A NOVEL PASSIVE QUENCHING METHOD WITH ADAPTIVE RESISTIVE SWITCHING 76
  - 6.1 Introduction: Understanding Quenching Mechanisms in SPAD 77
    - 6.1.1 Working Principles of the SPAD Passive Quenching 77
    - 6.1.2 How Adaptive Resistive Switch Effective in This System 79
  - 6.2 ARS Devices Fabrication and Measurement 80
    - 6.2.1 ARS Fabrication Process 80
    - 6.2.2 Packaging and Electrical Characterization 81
  - 6.3 Measurements of Avalanche Quenching Dynamics 83
    - 6.3.1 Experimental Setup 83
    - 6.3.2 Characterization of SPAD Performance Integrated with ARS 84
    - 6.3.3 Comparison with Conventional Passive Quenching 87
  - 6.4 Simulation and Analysis of ARS-Based Quenching Mechanisms in SPADs . . 90
    - 6.4.1 The Circuit Design for Simulation 90
    - 6.4.2 Model of ARS 93

6.4.3 Simulation Results and Analysis 94
6.5 Concluding Remarks of This Chapter 95

7 DESIGNING MECHANICALLY ROBUST AND POROUS ALL-INORGANIC ANTIREFLECTIVE COATINGS USING MICROPOROUS POLYMERS 97
7.1 Introduction: Antireflective Coatings 98
7.2 Fabrication of Porous Coatings: Utilizing Polymer Templates for ALD Deposition 99
7.2.1 Materials 99
7.2.2 Polymer Film Deposition 100
7.2.3 Solution Treatment of the Deposited Polymer 100
7.2.4 Infiltration of the Polymer Templates with Alumina Precursors to Form ARCs 101
7.3 Characterization of Porous Coating Thin Films 102
7.3.1 Refractive Index of the Infiltrated Thin Films 102
7.3.2 Electron Microscopy and X-Ray Characterization 103
7.4 Antireflective Properties of Single-Layer and Graded-Index Double-Layer ARC Coatings 105
7.4.1 Optical Performance on Sapphire Glass 106
7.4.2 Optical Performance on Gorilla Glass 108
7.5 Mechanical Stability of Single-Layer and Graded-Index Double-Layer ARC Coatings 110
7.5.1 Methods - Nanoindenter 110
7.5.2 Thin Film Hardness 111
7.5.3 Thin Film Scratch Resistivity 111
7.5.4 Discussion of Results 113
7.6 Concluding Remarks of This Chapter 113

8 CONCLUSION OF THIS JOURNEY 115
8.1 Summary of Key Findings 115
8.2 Future Research Outlook 116

REFERENCES 119

LIST OF FIGURES

1.1 How quantum memory extends entanglement 5

2.1 ALD system and processes 21
2.2 Thin film characterization 26
2.3 Thickness map over 4-inch wafer 27
2.4 Electron microscopy of Er-doped thin films 29
2.5 HAADF-SETM images of Er doped TiO_2 33
2.6 The optical measurement setup for the thin films. 35
2.7 Thin film PLE spectra 37
2.8 PLE spectra of unannealed films and waveguide integrated thin films 39

3.1 Photonic crystal cavity simulations 47
3.2 The designed adiabatic inverse taper waveguide to fiber coupling structure . . . 49
3.3 Inverse taper FDTD simulation results. 49
3.4 Fabrication of photonic cavity and waveguide devices. 52

4.1 The optical measurement setup for the photonic devices. 56
4.2 ALD TiO_2-Si photonic crystal cavities 58
4.3 Optical measurements on fabricated devices at T = 3.5 K 60
4.4 Fabricated photonic cavities characterization. 64
4.5 PLE Measurements on cavity-coupled Er ensembles at 3.5 K 68

5.1 Overview of the platform to optically isolate single Er^{3+} ions 70
5.2 Purcell enhancement and antibunching of single photons 72
5.3 Single ion spectral diffusion 74

6.1 Schematic of the circuit model for SPAD 78
6.2 Electron microscope photographs of the ARS devices 81
6.3 Current–voltage characteristics of the ARS 83
6.4 Quenching experiment results with ARS 85
6.5 Conventional passive quenching results and comparison with ARS 88
6.6 The count rate comparison at a input repetition rate of 20MHz 90
6.7 Schematic circuit diagram for Pspice simulation 92
6.8 Pspice simulations of a SPAD quenched by the ARS 95

7.1 Depiction of the steps involved in the fabrication of single-layer and double-layered AlO_x ARCs 101
7.2 The refractive indices of AlO_x^{PIM} and AlO_x^{BCP} versus different wavelengths. . . 103
7.3 SEM and SAXS measurements results. 105
7.4 Optical performance of single (AlO_x^{PIM}) and graded-index double-layered ($AlO_x^{PIM/BCP}$) ARCs deposited on sapphire glass 107
7.5 Optical performance of single (AlO_x^{PIM}) and graded-index double-layered ($AlO_x^{PIM/BCP}$) ARCs deposited on Gorilla glass 109

7.6 Mechanical properties of the single- and the graded-index double-layered ARCs . 112

LIST OF TABLES

2.1 Sample deposition and Er doping parameters 30

ACKNOWLEDGMENTS

This work is primarily supported by Q-NEXT, a U.S. Department of Energy Office of Science National Quantum Information Science Research Center under Award Number DE-FOA-0002253. The device fabrication were mostly performed at the Center for Nanoscale Materials, a U.S. Department of Energy Office of Science User Facility, supported by the U.S. DOE, Office of Basic Energy Sciences, under Contract No. DE-AC02-06CH11357. Additional support for TEM characterization is supported by Quantum Information Science research funding from the U.S. DOE, Office of Science User Facility. The devices and materials characterization support was provided by the U.S. Department of Energy, Office of Science; Basic Energy Sciences, Materials Sciences, and Engineering Division. The computation and simulation work was completed in part with resources provided by the University of Chicago's Research Computing Center.

Regarding personal acknowledgments, I would like to first express my deepest gratitude to my advisor, Professor Supratik Guha, for his outstanding leadership and unwavering support in our group's research on quantum science and engineering. Beyond being an exemplary mentor, he has instilled in us the values and skills necessary to become versatile scientists across disciplines.

I am also sincerely thankful to my co-advisor, Dr. Alan Dibos, for his invaluable guidance on multiple projects. His mentorship has provided me with hands-on experience in device fabrication, optical measurement, and experimental design, which has been instrumental in shaping my academic and professional growth.

I would like to extend my gratitude to the members of my committee, Professor Alex High, Professor Supratik Guha, and Dr. Alan Dibos, for their insightful feedback and support throughout my doctoral journey.

Additionally, I am immensely grateful to my colleagues and collaborators who have supported me over the past five years. I would especially like to thank Dr. Elena Shevchenko, Dr. David A. Czaplewski, Dr. Ralu Nana Silvia Divan, Liliana Stan, and C. Suzanne Miller for their close collaboration at the Center for Nanoscale Materials.

I am also deeply appreciative of the contributions and camaraderie of Dr. F. Joseph Heremans, Dr. Jiefei Zhang, Dr. Gregory Grant, Dr. Koichi Tanaka, Dr. Muchuan Hua, Dr. Jianguo Wen, Dr. Swarnabha Chattaraj, Dr. Kathryn Sautter-Montoya, Dr. Jiyuan Zheng, Dr. Zhongbo Zhang, Dr. Yizhong Huang, Dr. Manish Kumar Singh, Dr. Sean Sullivan, Dr. Robert Pettit, Dr. Vasileios Niaouris, Dr. Tim Draher, Ignas Masiulionis, Connor Horn, Sagar Seth, Claire McDermott, Xella Doi, and Michael Solomon, all of whom directly collaborated with me on various projects.

Meanwhile, I would also like to thank my colleagues at Applied Materials: Dr. Robert Visser, Dr. Ruoyu Li, Dr. Zihao Yang, Dr. Jake Rochman, and Dr. Haoxiong Yan, for sharing their expertise and offering me valuable insights into the industry, as well as for their guidance in fostering my professional growth during my summer internship.

Finally, I extend my heartfelt gratitude to my family, friends, and everyone who has been part of this journey. In particular, I wish to thank my father, who has been a pillar of unwavering support throughout my 28 years and who has exemplified the values and strength that have guided me in becoming the person I am today. I also want to express my deep appreciation to my girlfriend, Jingyao, whose steadfast support during my most stressful days and the joy she brought into my life helped me gain clarity about my goals and the life I truly want to live.

ABSTRACT

Quantum communication networks rely on quantum memory devices to enable long-distance entanglement distribution. Erbium (Er^{3+}) is a promising candidate for quantum memory due to its telecom C-band optical transition, which allows seamless integration with existing fiber-optic infrastructure. However, challenges such as spin coherence limitations, material integration, and non-radiative decay mechanisms must be addressed to realize practical Er-based quantum memory systems.

This dissertation investigates the development of erbium-doped titanium oxide ($Er{:}TiO_2$) integrated with silicon photonics as a platform for quantum memory. A primary focus is the deposition and characterization of Er-doped thin films using atomic layer deposition (ALD), providing a scalable and CMOS-compatible approach to quantum memory fabrication. The integration of Er-doped materials into photonic crystal cavities enables Purcell enhancement, significantly improving optical readout efficiency. The optical measurements provide essential insights into cavity-ion quantum electrodynamics. In particular, the experiment of isolating single erbium ions establish a crucial foundation for realizing spin-photon interfaces, enabling the integration of quantum memories into CMOS-compatible quantum photonic platforms.

This work plays a pivotal role in advancing hybrid quantum system integration, a critical step toward enabling scalable and distributed quantum networks. By developing a fully CMOS-compatible platform, this research not only enhances the feasibility of practical quantum memory technologies but also lays the groundwork for next-generation quantum communication infrastructure, accelerating the realization of global quantum networks.

Beyond quantum technologies, this thesis also explores broader advancements in photonics, including a novel dynamic quenching method for single-photon avalanche diodes (SPADs) and the development of mechanically stable, ultra-thin anti-reflective coatings (ARCs) for displays. Both studies demonstrate technological progress through innovative integration strategies and process development, contributing to the evolution of photonic engineering.

CHAPTER 1

INTRODUCTION

1.1 Quantum Communication: Building the Network for Quantum Computers

Quantum technologies based on the principles of quantum mechanics such as superposition and entanglement are targeted to enable transformative advances in computation, communication and sensing.[1,2,3,4,5] These technologies exploit the unique properties of quantum systems to perform tasks that are infeasible with classical systems. For example, quantum computers have the potential to solve complex problems in material science, cryptography, and drug discovery by processing information with fundamentally acceleration using qubits.[6,7,8,9] Quantum communication ensures unbreakable security through quantum key distribution (QKD) protocols that rely on the inherent unpredictability of quantum measurements.[3,10,11] Quantum sensing and metrology harness extreme sensitivity to detect minor changes in gravitational fields, electromagnetic waves, or biological signals, exceeding the limits of classical measurement techniques.[12,13] Together, these advances are not only pushing the boundaries of physics but also paving the way for practical applications with profound implications for science, industry, and society.

1.1.1 The Necessity and Challenges of Quantum Communication

In the realm of quantum technologies, quantum communication acts as the vital connection between different quantum systems, enabling applications ranging from quantum cryptography for secure communication to distributed quantum computing, where multiple quantum resources collaborate to solve complex problems.[14,15] These quantum communication links are fascinating because quantum cryptography provides supremacy of security, with the magic based on the entanglement and no-cloning theorem of quantum states.[16,17] To achieve reliable quantum communication, photons—often referred to as “flying qubits”—are the ideal choice for long-distance communication, as they can efficiently link stationary qubits, fulfilling the DiVincenzo criteria.[18] The most explored modes of quantum communication to date include ground-to-satellite links[19,20] and photon transmission through optical fibers,[21] both of which demonstrate the immense potential of photons as carriers of quantum states across the globe.

A significant bottleneck in advancing quantum technology lies in the challenges of error rates and operational speed, a limitation shared by quantum technologies.[22] However, unlike quantum computing, quantum communication faces the additional obstacle of photon qubit loss during transmission,[23] a challenge also encountered in classical communication systems. For instance, telecom C-band photons (wavelength $\sim 1.5\ \mu$m) experience minimal attenuation in telecommunication optical fibers, with a loss rate of approximately 0.2 dB per kilometer. This translates to a mere 10% chance of a single photon successfully traveling 30 miles through optical fiber.[24] In classical communication, signal amplifiers are widely employed to mitigate such losses.[25] In quantum communication, the direct amplification of photon signals is prohibited by the non-cloning theorem, which prevents the duplication of unknown quantum states.[26] This fundamental limitation necessitates the development of novel quantum technologies or protocols capable of meeting the stringent demands of reliable and efficient quantum communication.

1.1.2 Quantum Repeaters with Quantum Memory: A Solution for Long-Distance Communication

To address the problem of photon loss, quantum repeaters embedded with long-coherence quantum memory are envisioned as the "amplifiers" of quantum signals.[27,28] The quantum repeaters divide the communication channel into shorter segments, where quantum entanglement is established and stored in quantum memories at intermediate nodes. Through the entanglement swapping, these segments are connected to create entanglement across the entire channel. Therefore, reliable and scalable quantum communications over vast distances are enabled.[29,30] While the concept of quantum repeaters is both feasible and promising, there are four stringent technological criteria that must be met for the associated protocols and devices to function effectively:[31]

(I) The flying qubit photons are ideally in the near-infrared range to minimize the transmission loss.

(II) The quantum repeater nodes are initialized individually and can store the qubits for a time much longer than the communication time over the network.

(III) The protocol implemented is robust against photon loss.

(IV) The quantum repeater nodes can store and emit the photon qubits with high fidelity and efficiency within its coherence time.

Meeting these requirements demands the development of high-quality quantum memory serving as a temporary storage medium for quantum states, allowing entanglement to be created, maintained, and extended across segments of a communication channel. While alternative all-photonic quantum repeaters that do not rely on quantum memories have recently been proposed and studied[32,33,34], these approaches require redundant qubits and highly efficient gates for error correction, raising concerns about cost efficiency. Consequently, quantum memory devices remain the preferred choice for quantum repeaters.

The thesis will focus on the development of CMOS-compatible quantum memory devices that can be seamlessly integrated with existing fiber-optic networks, paving the way for future global optical fiber-based quantum communication systems. Initiatives like the quantum loop testbed between Argonne National Laboratory and the University of Chicago[35] exemplify the practical application of such technologies, leveraging existing infrastructure to advance quantum communication research and bring it closer to real-world deployment.

1.2 Extending Entanglement Through Memory-Assisted Networks with Quantum Repeater

As mentioned in the previous section, quantum memory is the key to extend the entanglement across the whole network. In this section, the key technique − entanglement swapping via Bell State Measurement (BSM) − will be discussed to demonstrate how the entangled pairs can be connected with each other over long distances.[36]

We will start from two independent entangled pairs from between Alice and Charlie, and Bob and Charlie, where Charlie is between Alice and Bob. This step is typically easy to realize with a entangle photon pair generation.[37] Therefore, we have:

$$|\Phi^+\rangle_{AC} = \frac{1}{\sqrt{2}}(|0\rangle_A|0\rangle_C + |1\rangle_A|1\rangle_C) \tag{1.1}$$

$$|\Phi^+\rangle_{CB} = \frac{1}{\sqrt{2}}(|0\rangle_C|0\rangle_B + |1\rangle_C|1\rangle_B) \tag{1.2}$$

where $|\Phi^+\rangle_{AC}$ is the bell states between Alice and Charlie and $|\Phi^+\rangle_{CB}$ is the bell states between Charlie and Bob.

Initially, there is no direct entanglement between Alice (A) and Bob (B)—they are only indirectly linked through Charlie's two qubits.

The total state of the system is the tensor product of these two Bell pairs:

$$|\Psi_{\text{initial}}\rangle = |\Phi^+\rangle_{AC} \otimes |\Phi^+\rangle_{CB} \tag{1.3}$$

Expanding each Bell state:

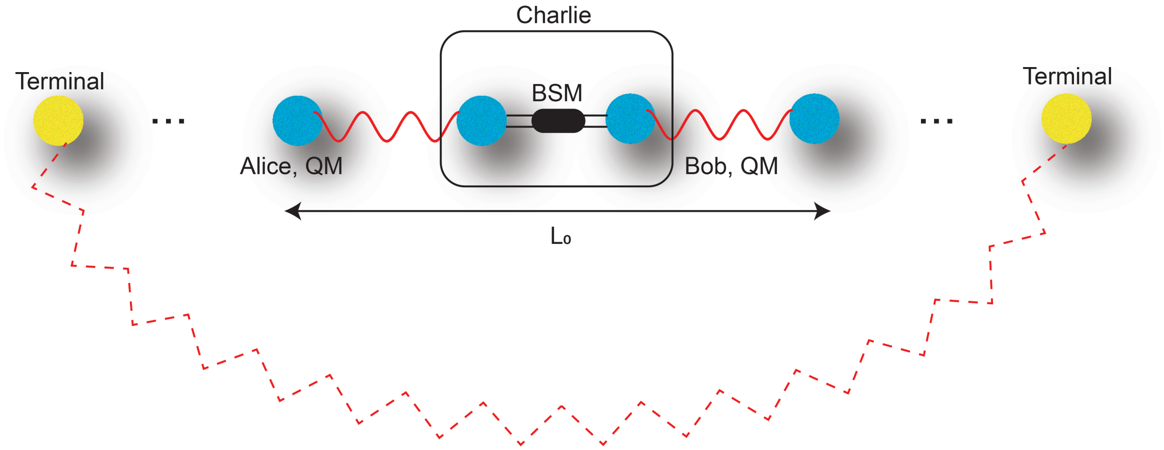

Figure 1.1: A schematic representation of how quantum memory extends entanglement. Alice and Bob serve as quantum memory (QM) nodes, each entangled with separate qubits from Charlie. Adjacent quantum memories are separated by a distance L_0. Charlie performs Bell-state measurements (BSM) on his qubits, enabling entanglement swapping. This process extends the entanglement to Alice and Bob. By repeating this procedure across multiple segments and synchronizing operations, the two terminals can ultimately become fully entangled.

$$\begin{aligned}|\Psi_{\text{initial}}\rangle &= \left(\frac{1}{\sqrt{2}}(|00\rangle_{AC} + |11\rangle_{AC})\right) \otimes \left(\frac{1}{\sqrt{2}}(|00\rangle_{CB} + |11\rangle_{CB})\right) \\ &= \frac{1}{2}\Big(|00\rangle_{AC}|00\rangle_{CB} + |00\rangle_{AC}|11\rangle_{CB} + |11\rangle_{AC}|00\rangle_{CB} + |11\rangle_{AC}|11\rangle_{CB}\Big) \end{aligned} \tag{1.4}$$

Rearrange the terms:

$$|\Psi_{\text{initial}}\rangle = \frac{1}{2} \sum_{i,j\in\{0,1\}} |i\rangle_A |j\rangle_B |i\rangle_C |j\rangle_C \tag{1.5}$$

Charlie now performs a Bell State Measurement (BSM) on his qubits C_1 and C_2 , projecting them into one of the four Bell states:

$$|\Phi^{\pm}\rangle_{CC} = \frac{1}{\sqrt{2}}(|00\rangle_{CC} \pm |11\rangle_{CC}) \tag{1.6}$$

$$|\Psi^{\pm}\rangle_{CC} = \frac{1}{\sqrt{2}}(|01\rangle_{CC} \pm |10\rangle_{CC}) \tag{1.7}$$

To rewrite the total state in terms of these Bell states, we express the C_1C_2 basis in terms of the Bell states:

$$|00\rangle_{CC} = \frac{1}{\sqrt{2}}(|\Phi^{+}\rangle + |\Phi^{-}\rangle) \tag{1.8}$$

$$|11\rangle_{CC} = \frac{1}{\sqrt{2}}(|\Phi^{+}\rangle - |\Phi^{-}\rangle) \tag{1.9}$$

$$|01\rangle_{CC} = \frac{1}{\sqrt{2}}(|\Psi^{+}\rangle + |\Psi^{-}\rangle) \tag{1.10}$$

$$|10\rangle_{CC} = \frac{1}{\sqrt{2}}(|\Psi^{+}\rangle - |\Psi^{-}\rangle) \tag{1.11}$$

Using this transformation, the initial state can be rewritten as:

$$|\Psi_{\text{initial}}\rangle = \frac{1}{2}\left(|\Phi^{+}\rangle_{CC}|\Phi^{+}\rangle_{AB} + |\Phi^{-}\rangle_{CC}|\Phi^{-}\rangle_{AB} + |\Psi^{+}\rangle_{CC}|\Psi^{+}\rangle_{AB} + |\Psi^{-}\rangle_{CC}|\Psi^{-}\rangle_{AB}\right) \tag{1.12}$$

Once Charlie measures his qubits in the Bell basis, his qubits collapse into one of the four Bell states. The result is sent to Alice and Bob as two classical bits (00, 01, 10, 11), telling them which entangled state they now share.

If Charlie's BSM result is:

I. $|\Phi^{+}\rangle_{CC}$, Alice and Bob now share $|\Phi^{+}\rangle_{AB}$, already entangled.

II. $|\Phi^{-}\rangle_{CC}$, Alice and Bob share $|\Phi^{-}\rangle_{AB}$, correctable by a Z gate on Bob's qubit.

III. $|\Psi^{+}\rangle_{CC}$, Alice and Bob share $|\Psi^{+}\rangle_{AB}$, correctable by an X gate.

IV. $|\Psi^-\rangle_{CC}$, Alice and Bob share $|\Psi^-\rangle_{AB}$, correctable by an XZ gate operation.

Thus, by applying the corresponding Pauli correction (I, Z, X, XZ), Alice and Bob successfully recover a maximally entangled state, effectively extending their entanglement over long distances. By systematically implementing the same protocol across multiple segmented network nodes in a synchronized manner several times, two remote nodes can ultimately be entangled, enabling long-distance quantum communication.

While the underlying physics is straightforward, implementing such quantum networks poses significant engineering challenges. One major challenge arises from the unpredictability of photon emission times and inherent network delays, which cause photons from separate locations to rarely arrive simultaneously. This timing mismatch makes direct entanglement swapping between Alice and Bob exceptionally difficult.

Therefore, quantum memory addresses this issue by temporarily storing the quantum states carried by photons, enabling synchronization of photon operations across different network nodes.[38,39] As mentioned previously, quantum repeater nodes must preserve these quantum states with coherence times exceeding network delays and operational durations, setting a fundamental performance benchmark for quantum memory devices. Moreover, uncertainties in quantum memory readout, such as photon re-emission variability, must be minimized. Additionally, both storage and readout efficiencies are crucial, as they directly influence the data transfer rate and overall performance of quantum network nodes.

1.3 Rare Earth Ions: A Promising Platform for Long-Coherence Quantum Memory

1.3.1 Why Rare Earth Ions Are Well-Suited for Quantum Memory

To realize a quantum memory, two critical properties must be considered: storage/readout efficiency and quantum state coherence time. The first criterion requires the quantum memory to facilitate the high-fidelity conversion of photon states into localized states (such as spin states) and back. The second criterion necessitates that the quantum state remain stored for a sufficiently long duration to allow for all operations within a quantum network to be completed before decoherence occurs. Atomic defects in solid-state systems emerge as ideal candidates for quantum memory applications due to their inherent spin-photon interface, ease of spin-state manipulation, and relatively long coherence times, which can be further extended using decoupling techniques[40]. While alternative approaches have shown promise in demonstrating quantum memory functionality[41,42], this thesis will primarily focus on the development and study of quantum memory based on atomic defects.

Atomic defect systems, such as nitrogen-vacancy (NV) centers in diamond, are widely studied for their unique quantum spin states, which are valuable for quantum computing applications[43,44,45,46]. NV centers are optically active, and their fluorescence depends on the spin state, enabling quantum information initialization and readout[47,48]. However, like many solid-state defect systems, NV centers can be influenced by environmental factors such as high temperatures or external electric fields, which may cause charge instability and affect their performance in certain conditions.

Unlike traditional spin defects like NV centers, rare earth ions provide a complementary approach by relying on their atomic transitions, which are intrinsically robust due to the shielding of the 4f-orbitals by the outer 5s and 5p electrons. This shielding makes their quantum states highly resistant to decoherence from environmental disturbances, offering significant potential for quantum memory applications.[49,50] For instance, the europium (Eu) ion has demonstrated spin coherence times of up to six hours under optimal conditions, showcasing its suitability for long-term quantum information storage.[51]. Overall, rare-earth ions stand out as highly promising candidates for quantum memory applications, owing to their exceptional coherence properties and intrinsic robustness.

Rare earth ions, in addition to their excellent spin properties, exhibit outstanding optical performance. They are widely used in the optical industry for applications such as lasers and fiber amplifiers[52,53,54]. Their relatively narrow emission linewidths, combined with broad absorption and emission spectra, simplify the implementation of multiplexing[55,56]. These optical characteristics are also highly desirable for quantum memory applications. Specifically, the narrow emission linewidth allows for the spectral isolation of single ion qubits, facilitating simpler and more precise quantum operations. Moreover, the broad spectra enable the realization of multi-channel quantum communication.

1.3.2 Erbium: A Telecom-Compatible Rare Earth Ion for Quantum Memory

Among rare earth ions, erbium (Er) is particularly promising for quantum memory due to its intrinsic telecom C-band optical transition. The emission at approximately 1550 nm permits direct interfacing with the classical communication network, eliminating the need for frequency conversion. Recent studies have further demonstrated a coherence time of 23 ms for Er ions doped in crystal host materials, making them suitable for a range of quantum memory applications.[57] As a Kramers ion (non-integer electron spin), Er has a shorter coherence lifetime compared to non-Kramers ions (integer electron spins, such as Eu). However, this limitation is offset by its stronger Zeeman effects and the presence of more accessible nuclear spin states, which are characteristic of Kramers ions[58].

Despite the advantages of the telecom-C band transition, the long optical lifetime of Er ions remains a challenge for quantum memory devices[59]. The first excited state lifetime of Er^{3+} is typically a few milliseconds[60,61], which severely limits the efficient storage and emission of photon qubits. Therefore, high-fidelity storage and readout require coupling Er^{3+} to nanophotonic cavities to enhance photon-atom interactions. In particular, Purcell enhancement[62] can significantly increase the decay rate of the excited state. Thus, the successful design and integration of cavities are crucial for implementing Er^{3+}-based quantum repeaters.

In summary, rare-earth ions, particularly Er^{3+}, offer a promising platform for quantum memory applications due to their long spin coherence times, robust atomic transitions, and direct compatibility with telecom-wavelength optical networks. While the long optical lifetime of Er^{3+} poses a challenge for efficient photon storage and emission, this limitation can be addressed through nanophotonic cavity integration, where Purcell enhancement accelerates the excited-state decay rate. The successful implementation of such cavity-enhanced Er^{3+} systems is a crucial step toward realizing high-fidelity quantum memory and advancing quantum repeater technologies. This thesis aims to overcome these challenges by incorporating Er^{3+} ions into CMOS-compatible thin films and monolithically integrating them onto an SOI photonics platform.

1.4 Selecting Erbium-Doped Host Materials for Quantum Memory Applications

With Er^{3+} as the chosen quantum memory defect, selecting an optimal host material is crucial for maximizing device performance and integration. In recent years, extensive research has explored Er^{3+} integration into various host materials, including $Er:TiO_2$,[63,64,65] $Er:Y_2O_3$,[61,66] $Er:CaWO_4$,[57,67] $Er:Y_2SiO_5$,[68] Er:MgO,[69] $Er:YVO_4$,[70] $Er:LiNbO_3$,[71,72,73] and also Er:Si[74,75]. Each material offers distinct advantages in different aspects. However, the successful and commercially viable implementation of Er^{3+}-based quantum memory requires the host material to satisfy several key criteria:

I. Low abundance of nuclear spins. At low temperatures, phonon scattering in the lattice becomes negligible, and nuclear spin fluctuations become the dominant source of electron spin decoherence[76]. These fluctuations generate magnetic noise, which dephases the Er^{3+} electronic and nuclear spin states, thereby limiting coherence time.

II. Wide bandgap. The host material must have a bandgap greater than 0.8 eV, corresponding to the typical photon energy in the telecom C-band. To prevent undesired photon interactions with the host material, the Er^{3+} optical transition should remain well within the bandgap.

III. Low defect densities. Beyond spin coherence, quantum memory also demands high optical coherence. Achieving narrow optical linewidths requires a host material with minimal strain, charge, and phonon fluctuations, which are often introduced by defects arising from material deposition and Er doping.

IV. CMOS integration compatibility. For large-scale industrial adoption, the host material should be compatible with CMOS fabrication processes. This enables scalable production and seamless integration with silicon photonics and electronic chips, similar to modern memory and computing devices.

To select an optimal host for quantum communication, we must consider the structure of the solid-state environment. While bulk oxide crystals provide largely defect-free conditions, Er-doped thin-film hosts, including wide-bandgap oxides grown on silicon, have emerged as a promising quantum memory platform. This is due to their compatibility with established semiconductor technology[61,64] and their potential for scalable on-chip integration[77,78,65]. Therefore, this thesis primarily focuses on thin-film technology for Er, the integration of Er into a CMOS-compatible silicon photonics platform, and performance benchmarking of the devices.

1.5 Comparative Analysis with Other Research on Erbium based Quantum Memory

Utilizing Er ion as a quantum memory offers significant advantages, as previously discussed. As a result, this field is rapidly advancing, leading to numerous high-impact research developments across various platforms. In this section, we present a comparative analysis of notable research efforts across the world focused on Er and other rare-earth ion based quantum memory, highlighting the key differences and advancements.

Prof. Jeff Thompson's group at Princeton University has made significant contributions to understanding erbium quantum emitters and their spin dynamics through a series of pioneering experiments. In 2018, they demonstrated a telecom-band single-photon source using Er-doped Y_2SiO_5 crystals integrated with silicon nanophotonic cavities[59]. Leveraging a similar experimental platform, they successfully achieved quantum non-demolition measurement of electron spin states with approximately 95% fidelity[79], as well as coherent manipulation of both electron spins[80] and nearby proton nuclear spins[81]. More recently, employing Er-doped $CaWO_4$, their group produced indistinguishable single photons characterized by remarkably narrow emission linewidths of around 150 kHz[67], enabling them to further demonstrate spin-photon entanglement with a fidelity of 73%[82]. Through these advancements in device fabrication and optimization of optical systems, their work has substantially enhanced the feasibility and potential of erbium-based quantum memory technologies using bulk crystal systems.

Prof. Andrei Faraon's group at Caltech has conducted extensive research to advance rare-earth-ion-based quantum applications. Their work with Yb:YVO_4 has yielded significant results for quantum memory technologies, including the demonstration of single-shot spin-state readout[83] and coherent optical control of single Yb ion qubits[84]. Recently, they further demonstrated multiplexed entanglement using two nanophotonic cavities, each containing multiple Yb ions, achieving entanglement fidelity of approximately 88%, underscoring the substantial potential of rare-earth-ion quantum memories[85]. Additionally, the group has investigated Nd:YVO_4 systems, achieving coherent optical manipulation of rare-earth-ion ensembles, crucial for enhancing quantum memory capabilities[58,86]. Moreover, their research into Er ion ensembles significantly advanced the atomic frequency comb (AFC) quantum memory protocol, enabling frequency-multiplexed memory functionalities[87,88]. Furthermore, their work on microwave-to-optical transduction using erbium-ion ensembles has broadened the applicability of erbium beyond quantum memory, facilitating integration with superconducting quantum computing circuits and extending the scope of hybrid quantum technologies[70].

Prof. Philippe Goldner's group at PSL University has made significant contributions to the host material engineering of erbium ions, with a particular emphasis on optimizing spin coherence properties. Their investigations into Er:$CaWO_4$ have elucidated the underlying mechanisms of electron spin spectral diffusion[89]. Furthermore, they have successfully coupled Er-doped $CaWO_4$ crystal ensembles to superconducting microresonators, achieving exceptionally long electron spin coherence times of up to 23 ms at cryogenic temperatures[57]. This milestone represents a substantial advancement in quantum state storage capabilities. Additionally, their innovative integration of Er:Y_2O_3 with NV center implanted diamond[90] has demonstrated promising potential for hybrid quantum systems, which may extend the applicability of Er based quantum memories to broader quantum technologies. Through these advancements in material engineering and coherence preservation, their work is playing an essential role in developing scalable quantum memory platforms based on erbium.

Prof. Andreas Reiserer's group at the Technical University of Munich has achieved significant advancements in the development of Er:Si based quantum memory and integrated photonic systems. Their pioneering measurements on Er-implanted silicon waveguides demonstrated exceptionally narrow homogeneous optical linewidths of approximately 10 kHz[91,75]. Leveraging these promising optical properties, they successfully coupled Er ions to nanophotonic cavities, obtaining Purcell-enhanced emission lifetimes on the order of a few microseconds and enabling single photon emission[92]. More recently, their groundbreaking experiments achieved single-shot readout of individual Er spin qubits integrated within silicon, revealing electron spin coherence times between 20 to 40 µs—significantly longer than the enhanced emission lifetimes[93]. This achievement marks an essential milestone toward realizing CMOS-compatible quantum memory devices. Although challenges remain, particularly in extending coherence times and addressing non-radiative decay mechanisms compared to erbium-doped oxide materials, their work provides a robust foundation for developing scalable, chip-level quantum memory technologies.

Another significant research direction within our group, led by Prof. Supratik Guha, Prof. Alan Dibos, and Prof. Jiefei Zhang, focuses on exploring Er:CeO_2 as a novel platform for quantum memories. The cubic symmetry of CeO_2 is particularly promising for optimizing electron spin coherence properties[94]. Experimentally, colleagues within the group have successfully demonstrated the molecular beam epitaxy (MBE) deposition of Er:CeO_2 on silicon substrates and conducted comprehensive optical and structural characterizations of the doped material system[95]. At a measurement temperature of 3.6 K, the MBE-grown Er:CeO_2 exhibited a homogeneous optical linewidth of approximately 440 kHz and an electron spin coherence time of 660 ns, underscoring its potential for quantum networking applications[96].

Beyond the research discussed above, various groups have significantly advanced the field of erbium-based quantum systems. For instance, Prof. Hong Tang's team at Yale University has investigated Er:$LiNbO_3$ for single-photon emission, as well as electro-optical modulation within optical cavities[72,73], which could introduce valuable functionalities to on-chip quantum memory devices. Prof. Tian Zhong's research at the University of Chicago has provided critical insights into the optical linewidth mechanisms of Er:Y_2O_3, enhancing the fundamental understanding necessary for practical quantum memory development[97,66,98]. Additionally, work by Prof. John Bartholomew at the University of Sydney on Er:Si has demonstrated electron spin coherence on the millisecond scale, highlighting its viability for robust and reliable on-chip quantum memories[99].

1.6 Scope and Structure of This Thesis

This thesis explores the integration of Er:TiO_2 with silicon photonics for quantum memory applications, focusing on the development of scalable, CMOS-compatible platforms for quantum communication. The research spans material development, device fabrication, optical characterization, and single erbium ion-based quantum memory. This work aims to address key challenges in quantum memory performance and scalability.

The thesis, from **Chapter 2** to **Chapter 5**, primarily focuses on quantum memory research and is structured as follows:

- **Chapter 2** begins with an overview of the deposition techniques for erbium-doped thin films, establishing the foundational material platform for quantum memory applications. The chapter primarily explores the advantages of atomic layer deposition (ALD) in achieving uniform, high-quality thin films and provides a detailed characterization of the deposited materials. While molecular beam epitaxy (MBE) is also utilized in this research, it is not systematically introduced in this thesis. For a more comprehensive discussion on MBE-based growth techniques, readers are encouraged to refer to previously published work[100].

- **Chapter 3** focuses on the integration of Er-doped thin films into photonic crystal cavities, a critical step in enhancing the interaction between photons and quantum emitters. This chapter explores cavity QED and provides a comprehensive discussion on the design, simulation, and fabrication of photonic crystal cavities. These structures are engineered to couple with Er ion emitters, enabling improved optical readout efficiencies through Purcell enhancement.[65,64]

- **Chapter 4** presents the optical measurement techniques used to characterize integrated photonic devices. It covers cavity spectrum characterization and emission lifetime measurements, which are essential for evaluating Purcell enhancement and assessing the performance of erbium-based quantum memory. Additionally, the chapter provides a brief introduction to anomalous Purcell decay phenomena, highlighting the rich underlying physics within the cavity-ion quantum system.[65,101]

- **Chapter 5** explores the isolation of single erbium ions, a crucial step toward individual qubit readout for quantum information processing. It covers the experimental techniques used to detect and characterize single-ion emission, demonstrating the feasibility of single Er ions as quantum memory qubits. Additionally, the chapter discusses the current challenges and bottlenecks in realizing a single Er ion quantum memory within our system.[102]

Following this, I introduce two early-stage research projects that focus on broader topics in photonics and optics. These projects not only contribute to advancements in photonics technology but also played a crucial role in shaping my expertise, providing foundational training in photonics device fabrication and optical measurements.

- **Chapter 6** investigates the dynamic quenching of single-photon avalanche photodetectors (SPADs) using adaptive resistive switches (ARS). This chapter compares ARS-based quenching with conventional passive quenching methods and presents experimental and simulation results that highlight the advantages of ARS for high-speed photon detection.[103]
- **Chapter 7** shifts focus to the development of porous yet mechanically robust antireflective coatings (ARCs) using polymers of intrinsic microporosity (PIMs). The chapter discusses the fabrication, optical performance, and mechanical properties of single- and double-layered graded-index porous ARCs, which are essential for enhancing optical efficiency.[104]

Finally, **Chapter 8** concludes the thesis by summarizing key findings, discussing the broader implications of erbium-integrated photonic quantum memory, and outlining potential future research directions. These perspectives extend beyond quantum technologies, highlighting advancements that could impact a wider range of photonics applications.

To benchmark and contextualize the research presented in this thesis against the quantum memory studies discussed in Section 1.5, we highlight our distinctive focus on developing Er:TiO_2 integrated with silicon photonics within a fully CMOS-compatible framework. Rather than concentrating primarily on the optimization of intrinsic material properties, our approach prioritizes practicality and future product integration. The central objective of this research is to create a scalable, CMOS-foundry-compatible platform based on Er-doped oxide thin films. Furthermore, this study primarily emphasizes optical and photonic device integration, as optical readout constitutes a critical initial step toward realizing quantum memory functionalities. By establishing robust optical interfaces and integrated photonic architectures, our work lays a foundational platform that will enable future explorations of spin dynamics and advanced quantum memory operations.

CHAPTER 2

DEPOSITION TECHNIQUES FOR ERBIUM-DOPED THIN FILMS: THE FOUNDATION FOR QUANTUM MEMORY

To realize Erbium-based quantum memory devices, the first step is doping Erbium into thin-film host materials that can be integrated on the silicon photonics platform. Previous studies have used ion implantation[91,92] to directly embed Er into devices. This technique is relatively straightforward; however, due to the large Er ion mass, the implantation process can cause significant lattice damage upon impact, leading to interstitial defects and undesired decay pathways. While high-temperature annealing can partially repair the crystalline structure, complete recovery is often challenging, which may impact the optical and coherence properties of the Er ions.

An alternative approach is molecular beam epitaxy (MBE) which offers an advantageous approach to fabricating high-quality erbium-doped thin films for quantum applications. Specifically, MBE is a physical vapor deposition technique conducted under ultra-high vacuum (UHV) conditions ($<10^{-8}$ Torr), where molecular or atomic beams directly deposit onto substrates without interactions with residual gas molecules. This ultra-clean environment minimizes impurities, enabling highly controlled and precise layer-by-layer growth.

Leveraging these benefits, our group at the University of Chicago and Argonne National Laboratory has developed robust MBE methodologies for erbium-doped oxide materials[64,100,95]. Compared to conventional ion implantation methods, this bottom-up approach significantly reduces crystal lattice damage. Prior studies have established that our optimized MBE deposition and subsequent annealing treatments dramatically enhance optical properties of erbium emitters, improving key metrics such as brightness and emission linewidth. These advances have been clearly demonstrated in Er:TiO_2[100] and Er:CeO_2[95]. Building upon these reliable deposition processes and comprehensive understanding of material-host interactions, this thesis further investigates anomalous Purcell effect and single Er ion isolation phenomena in MBE-grown Er:TiO_2, as elaborated in **Chapter 4**, **Section 4.2** and **Chapter 5**.

Despite its advantages, MBE also presents significant challenges. The stringent UHV requirements, substrate-dependent growth parameters, and high-cost instrumentation make it impractical for large-scale foundry processing. These limitations hinder its widespread integration with silicon photonic circuits, restricting its scalability for commercial applications.

Another alternative approach for achieving such integration is the growth of high-quality thin films via atomic layer deposition (ALD). This chapter will focus on the ALD process for erbium-doped thin films, including a brief introduction to atomic layer deposition, the deposition process of erbium-doped TiO_2 thin films, and the characterization results used to evaluate their performance. The content of the ALD growth and characterization are mainly reproduced from Ji et al.[65], with the permission of ACS Publications.

2.1 Unlocking Atomic Layer Deposition (ALD): A Key Tool for Precise Thin Film Growth

ALD is a thin-film deposition technique that enables precise control over material growth at the atomic level. It is a self-limiting, sequential process based on repeated cycles of gas-phase chemical reactions. The common ALD process consists of alternating exposure to two or more chemical precursors, which react on the substrate surface in a self-limiting manner with 4 steps[105,106]:

(I) The first precursor is introduced into the reaction chamber, where it reacts with the surface to form a monolayer.

(II) The chamber is then purged while waiting for the second precursor. During this step, excess precursor is removed by the background inert gas flow and the pumping system. This step is typically referred to as the purge step.

(III) The second precursor is introduced into the reaction chamber, where it reacts with the first precursor to form the thin film. The reaction is usually driven by thermal energy. However, in Plasma-Enhanced ALD (PEALD), the reaction can also be initiated by high-density plasma.

(IV) A second purge step removes excess precursor and byproducts before the next cycle begins.

This process allows for cyclic layer-by-layer deposition, offering precise control over film thickness and conformality. Nowadays, ALD already demonstrate broad applications in semiconductor industry, such as high-k dielectrics gate material, interconnect passivations, and display coatings.[107,108,109,110,103,111,104]

For the process of Er doped thin films, ALD offers significant advantages over molecular beam epitaxy as a manufacturing method for a variety of reasons including scalability, throughput, cost of operation, deposition conformality, and thin film uniformity. Studies on Er-doped dielectric oxides grown by ALD have been sparse, though ALD-grown Er-doped Al_2O_3 thin films have been used for on-chip nanolasers[112] and have shown potential for integration with waveguides.[113]

However, the reported optical linewidth in amorphous aluminum oxide has been too broad for quantum communication applications. To overcome this limitation, titanium dioxide (TiO_2) has emerged as a promising host material due to its low intrinsic nuclear spin density, which minimizes decoherence, and its relatively large optical bandgap.[114,94,115] Experimental studies have demonstrated narrow ensemble optical and spin linewidths for erbium implanted into bulk rutile-phase TiO_2, although these results required high-temperature annealing.[60] Additionally, reasonably narrow inhomogeneous optical linewidths have been achieved through MBE of single-crystal anatase TiO_2 thin films grown on $LaAlO_3$ substrates.[116] Furthermore, TiO_2 is widely used as a CMOS-compatible oxide material, making it a promising candidate for seamless integration into existing semiconductor fabrication

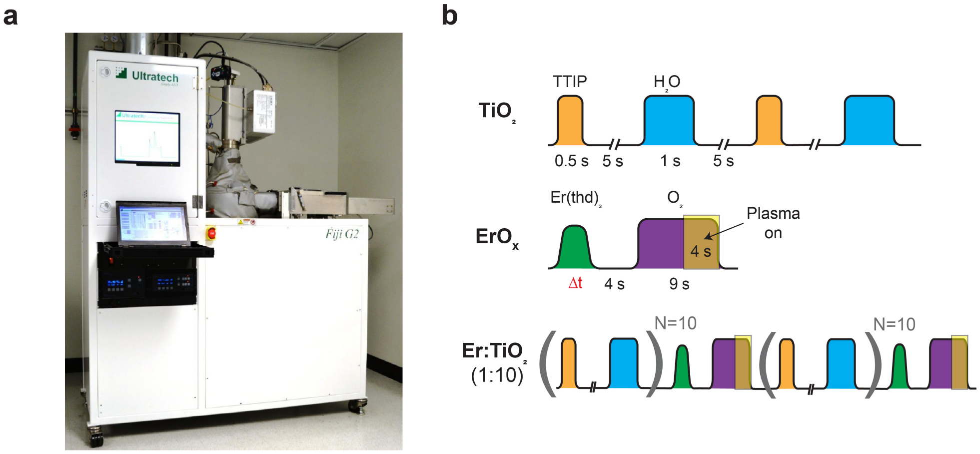

Figure 2.1: The ALD system and processes for Er:TiO_2 (a) The Fiji G2 PEALD system from Veeco Instruments Inc. in our lab, used for atomic layer deposition (ALD) of Er:TiO_2 thin film. (b) ALD deposition process pulse sequence. Top (TiO_2): Two cycles of thermal ALD growth, where the TTIP precursor and water are successively pulsed into the chamber and reacted to form a TiO_2 monolayer. Middle (ErO_x): A single cycle where the $Er(thd)_3$ is pulsed into the chamber with a bubbler and a turbo pump is used to remove excess precursor. The residual precursor reacts with oxygen plasma, which is turned on during the last 4 seconds of the oxygen pulse, to create a layer of erbium oxide. The $Er(thd)_3$ pulse length (Δt, marked in red) can be varied to control the doping level. Bottom (Er:TiO_2): Composite growth, where one ErO_x deposition cycle is followed by 10 cycles of TiO_2 deposition to space out the Er ions. The doping concentration can be further controlled by adjusting the $Er(thd)_3$ evaporation temperature and pulse length.

processes.

Therefore, the following discussion is primarily focused on the deposition process of erbium-doped TiO_2 thin films.

2.2 Engineering Erbium-Doped TiO_2 Thin Films Using ALD

In this study, we used a Fiji G2 PEALD system, which can be operated with and without plasma, to produce the Er-doped TiO_2 thin films. The deposition process involved the use of titanium isopropoxide (TTIP), produced from Sigma-Aldrich with 5N purity, and water (H_2O) as precursors for the thermal deposition of TiO_2.[117,118,119] The TTIP precursor was heated to 68 °C, and water (H_2O) was maintained at ambient conditions. During the TiO_2 deposition, the Ar flow was set to 110 sccm to purge out the by-product and excessive precursors from the chamber. We chose TTIP as the Ti precursor to minimize impurities in the as-grown TiO_2 thin films because of its composition, which comprises only elements of carbon, hydrogen, titanium, and oxygen.[120]

For the Er doping, we selected Tris(2,2,6,6-tetramethyl-3,5-heptanedionato)erbium, short for $Er(thd)_3$ or $Er(tmhd)_3$, produced from from Strem Chemicals with 3N purity. This precursor can react with oxygen plasma to form atomic layers of erbium oxides, thereby incorporating erbium into various host materials.[112,121,122,123,124] The operating power of the oxygen plasma was 300 W with O_2 flow of 25 sccm and Ar flow of 55 sccm.

In an effort to grow smooth films, we deliberately maintained the Si substrates at a temperature of 120 °C during the deposition —well below the 150-165 °C temperature range for deposition of anatase phase TiO_2[125] —at the expense of amorphous growth.[117]

The Er:TiO_2 ALD pulse sequence is depicted schematically in Figure 2.1b. Similar in overall sequence to that demonstrated for Er:Al_2O_3,[112] we employ an alternating sequence of undoped TiO_2 layers interrupted with single cycles of ErO_x to provide the Er doping. For the undoped thermal ALD TiO_2 deposition steps (Fig. 2.1b, top), we pulse the TTIP precursor into the chamber for 0.5 s and the water for 1 s, where the additional H_2O pulse time is used to fully consume the TTIP. We use a 5-second window after each pulse to pump out excess precursor, thereby allowing for a more homogeneous deposited layer. For the Er doping process, we introduce $Er(thd)_3$ into the chamber via a bubbler where it binds to the substrate (Fig. 2.1b, middle). The $Er(thd)_3$ pulse length is variable (Δt), to coarsely control the Er concentration. Following a 4-second wait time, we pulse molecular oxygen into the chamber and, synchronously, we open a turbo molecular pumping line to quickly remove excess precursors. After 5 s of O_2 flow, we ignite the oxygen plasma for 4 s, reacting with the $Er(thd)_3$ on the surface to form atomic layers of erbium oxide. Upon plasma cessation, we close the valve to the turbo pump, completing one cycle of ErO_x deposition. In this study, the growth cycle ratio was fixed at 1 cycle of ErO_x for every 10 cycles of TiO_2, as delineated in the lower panel of Figure 2.1b.

Unless noted otherwise, all of the thin films are deposited on lightly boron-doped standard silicon substrates from NOVA Electronic Materials and Silicon Valley Microelectronics (SVM), with the recipe demonstrated in this section.

After the deposition, we remove the sample from the reactor and perform ex-situ thermal anneal at 400 °C for 30 min in a rapid thermal annealing system (Annealsys), with a consistent O_2 flow rate of 500 sccm and resultant pressure near 700 Torr. The annealing step is crucial for recrystallizing the amorphous as-grown TiO_2, transforming it into the anatase polycrystalline phase, as will be further discussed in this thesis.

2.3 Characterization of Erbium-Doped Thin Films Deposited via ALD

Previous optical experiments have shown that the inclusion of undoped 'buffer' and 'capping' layers can reduce optical inhomogeneous broadening for epitaxial $Er:Y_2O_3$ films,[61] epitaxial $Er:TiO_2$ films,[116] as well as spectral diffusion and inhomogeneous linewidth broadening for Er in polycrystalline TiO_2 films.[63] While a thicker layer is better for optical properties, it is more difficult to etch for eventual nanophotonic devices. In this research, with both of these considerations in mind, the films used for our optical studies were grown with a '10/10/10' doped heterostructure: a 10 nm undoped TiO_2 buffer layer at the Si interface, a 10 nm Er-doped TiO_2 layer in the middle, and a 10 nm undoped TiO_2 capping layer on top.

To accommodate metrology techniques requiring thicker doped regions for sufficient depth resolution —such as Secondary-Ion Mass Spectrometry (SIMS) —we also fabricated a

‘20/50/20’ heterostructure, illustrated in Figure 2.4a (left), comprising of a 20 nm nominally undoped buffer layer TiO_2, a 50 nm Er-doped TiO_2 layer, and a 20 nm undoped TiO_2 capping layer. These thicker films were also utilized for Scanning Electron Microscopy (SEM) and Transmission Electron Microscopy (TEM) characterization, as they provide stronger signal contrast and improved imaging resolution.

2.3.1 Surface Roughness and Morphology

Surface roughness plays a critical role in the performance, integration, and scalability of photonic devices,[126,127,128] particularly for photonic cavities and waveguides. In high-quality optical systems, surface roughness can lead to increased scattering losses, degrading the quality factor(Q-factor) of photonic cavities and the transmission efficiency of optical waveguides. This effect is particularly detrimental in high-index contrast waveguides (e.g., silicon photonics), where even sub-nanometer roughness can significantly impact mode confinement and transmission.[129] Additionally, rough surfaces pose fabrication challenges, limiting device scalability and seamless integration with key components such as resonators, detectors, and modulators. In photonic integrated circuits (PICs), minimizing roughness is crucial for achieving low-loss interconnects and ensuring uniform performance across large-scale photonic chips. Therefore, precise control over thin-film surface roughness is essential for enhancing quantum memory performance and enabling its integration with silicon photonics.

To assess the surface roughness of $Er:TiO_2$ thin films deposited via Atomic Layer Deposition (ALD), we performed Atomic Force Microscopy (AFM) measurements under different deposition and post-processing conditions. The AFM height maps in Figure 2.2 illustrate the surface morphology of three samples:

(a) A film deposited at 300 °C (about 20 nm thick),

(b) An as-grown 10/10/10 thin film deposited at 120 °C,

(c) The corresponding annealed film from (b).

The root mean square roughness (Rq) and arithmetic mean roughness (Ra) values indicate that the as-grown and annealed films deposited at 120 °C exhibit very similar surface roughness. This suggests that the low-temperature deposition followed by high-temperature annealing preserves a smooth surface morphology, in contrast to films grown directly at higher temperatures (300 °C), which exhibit significantly increased roughness (Figure 2.2a). Maintaining low surface roughness with post-annealing is crucial for further integration with on-chip nanophotonic structures, such as waveguides and high-quality factor optical resonators.

2.3.2 Wafer Scale Uniformity

ALD is renowned for its exceptional wafer-scale uniformity, making it a key deposition technique for nanophotonic and semiconductor applications. Its self-limiting surface reactions enable angstrom-level thickness control, ensuring highly uniform thin films across large wafer areas. This level of uniformity is critical for high-volume semiconductor manufacturing, as it guarantees consistent device performance across the entire wafer, reducing process variability and enhancing scalability for advanced electronic and photonic devices.

To demonstrate the scalability of our ALD process, we investigated the deposition uniformity over a 100 mm silicon wafer. The deposited thin film is a "20/50/20" doped heterostructure. After deposition, the wafer was post annealed at 400 °C for 30 min with a consistent O_2 flow rate of 500 sccm and resultant pressure near 700 Torr, same as the annealing conditions mentioned before. The resultant thickness map in Figure 2.3 shows that the variation of thickness across the wafer is well below 1%.

2.3.3 Erbium Doping Concentration

For quantum memory applications, ideally, each photonic cavity would host a single dopant ion, functioning as a qubit without unwanted interactions with surrounding ions. However,

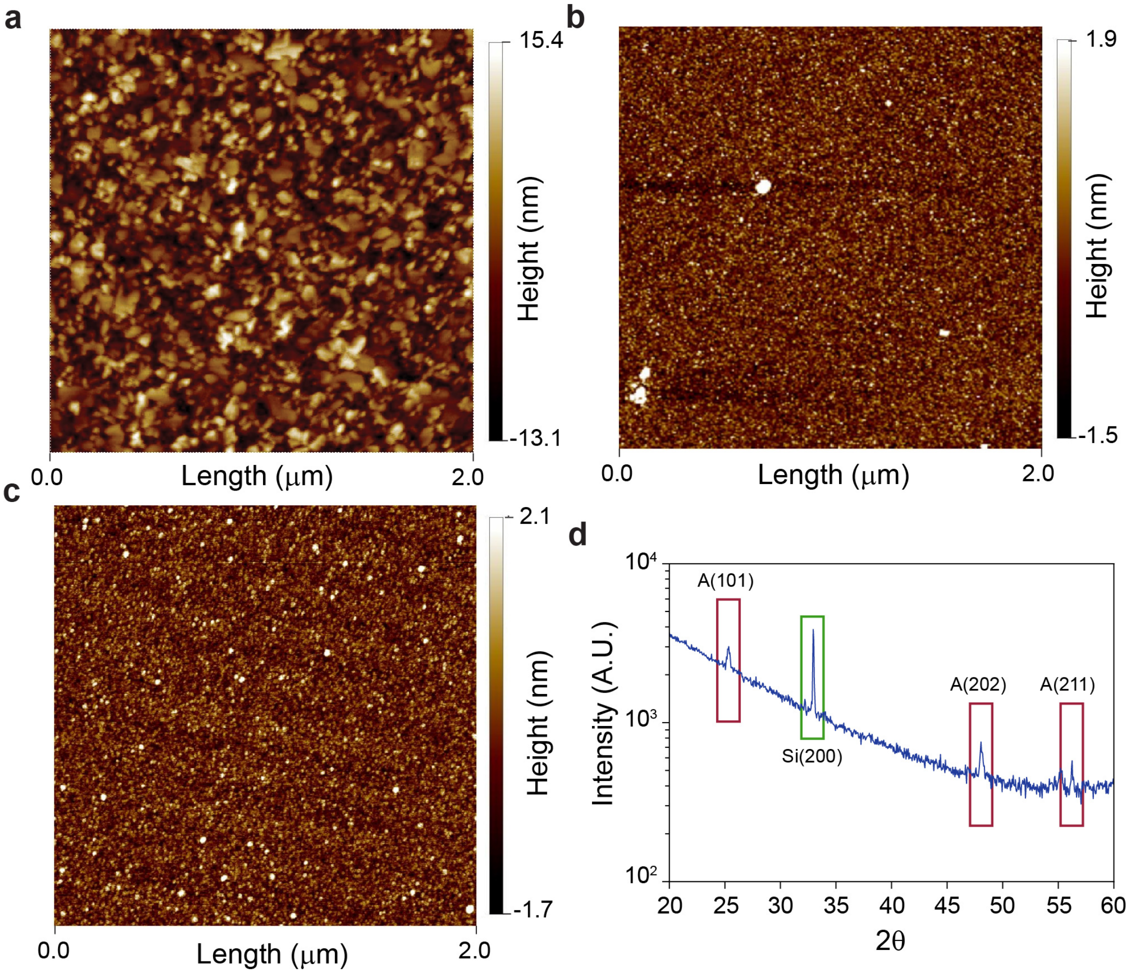

Figure 2.2: The ALD deposited thin film characterization. (a-c) Atomic Force Microscopy (AFM) height scans over a 2 μm × 2 μm scan area under different processing conditions: (a) undoped and unannealed TiO_2 film (about 20 nm) grown with a substrate temperature of 300 °C. The root mean square roughness (Rq) and arithmetic mean roughness (Ra) values are 3.62 nm and 4.43 nm, respectively. (b) the as-grown '10/10/10' structured thin film with a substrate temperature of 120 °C. (c) annealed thin films from the same growth run with (b). The Rq and Ra values for (c) are 0.522 nm and 0.348 nm, respectively. The Ra and Rq values for (d) are 0.520 nm and 0.399 nm, respectively. (d) X-ray Diffraction (XRD) spectrum of an oxygen-annealed Er-doped TiO_2 thin film grown on a Si(100) substrate. The thin film follows a '10/10/10' layered structure, as described in the main text. The anatase TiO_2 diffraction peaks are highlighted in red boxes, and the Si(200) peak from the substrate is highlighted in a green box.

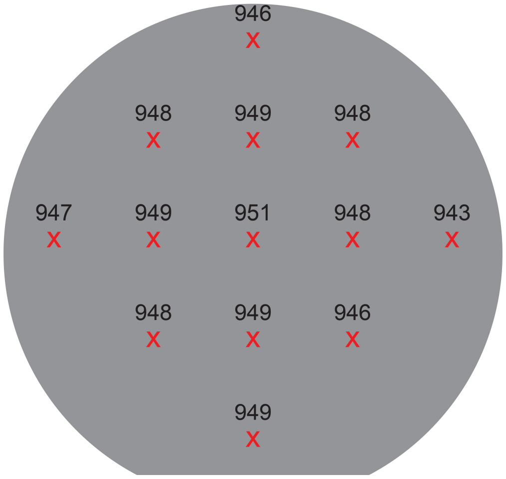

Figure 2.3: Thickness map of deposition across 4-inch wafer. We measured the ALD TiO_2 via a Horiba Jobin Yvon UVISEL spectroscopic ellipsometer. The red X's are marked at the points of measurement (13 points total with a pitch of 20 mm), with the thickness given in Å. The average thickness is 947.7 Å and the standard deviation is 2.0 Å. The estimated experimental uncertainty of each thickness is about ±2 Å given by the ellipsometry model fit to the film thickness.

achieving this is challenging because precise positioning of individual ions at the optimal coupling location is not feasible, and the ion's dipole orientation may not inherently align with the polarized light entering the cavity, limiting interaction efficiency. To overcome these limitations, generallz a lightly doped regime is necessary to increase the probability of incorporating well-coupled ion qubits while minimizing detrimental effects from ion-ion interactions.

However, ALD as a chemical precursor-based deposition technique has not yet demonstrated precise control over ultra-low doping concentrations. For our quantum memory development with Er, it is essential to establish a method for accurately controlling and reducing the Er doping level to enable reliable single-ion coupling within nanophotonic cavities.

In general, we can make use of two primary methods to control the concentration of dopants during ALD growth: (1) altering the TiO_2 deposition ratio relative to ErO_x deposition, or (2) controlling the growth rate of the ErO_x layer itself. In the first approach, the overall Er concentration is controlled by modifying the TiO_2 spacing (via insertion of more cycles of TTIP/H_2O) around each ErO_x layer. However, this method, while feasible and easy to apply in ALD processes, has a limited tuning range from a few percent to a few tenths of a percent due to the finite number of cycles required to grow a thin film. In this study we focused on the second method of controlling doping by tuning the erbium oxide deposition rate. For example, to decrease the Er concentration, we can lower the $Er(thd)_3$ evaporation temperature and shorten the precursor pulse. Consequently, in each cycle, a reduced amount of $Er(thd)_3$ will enter the reaction chamber.

To calibrate the Er concentration, we grew a series of samples by varying the evaporation temperature and pulse duration of $Er(thd)_3$, followed by Secondary Ion Mass Spectrometry (SIMS) analysis. To ensure sufficient depth resolution, these samples required a thicker doped region, leading us to grow a 20/50/20 heterostructure, as illustrated in Figure 2.4a (left).

The $Er(thd)_3$ precursor temperature, pulse duration, and experimentally measured Er concentrations via SIMS are summarized in Table 2.1, with doping levels ranging from sub-ppm to a few percent. Previous studies have shown that the vapor pressure of $Er(thd)_3$ decreases approximately 10-fold when the evaporation temperature drops by 25 °C above 130 °C.[130] In this work, we observed a similar trend: a 10-fold reduction in Er concentration between Samples No. 1 and No. 2 in Table 2.1, corresponding to a temperature decrease from 160 °C to 135 °C. However, further reducing the temperature to 110 °C (Sample No. 3) led to a dramatic decrease in Er incorporation, as this temperature falls below the reported $Er(thd)_3$ evaporation range.

To achieve sub-ppm doping, we further reduced the pulse duration from 8 s to 2 s (Sample No. 4). Notably, the lower Er doping concentrations (<2 ppm) observed in Samples No. 3 and No. 4 suggest that ALD can potentially achieve Er doping levels suitable for single-ion quantum applications by reducing the number of ErO_x layers.

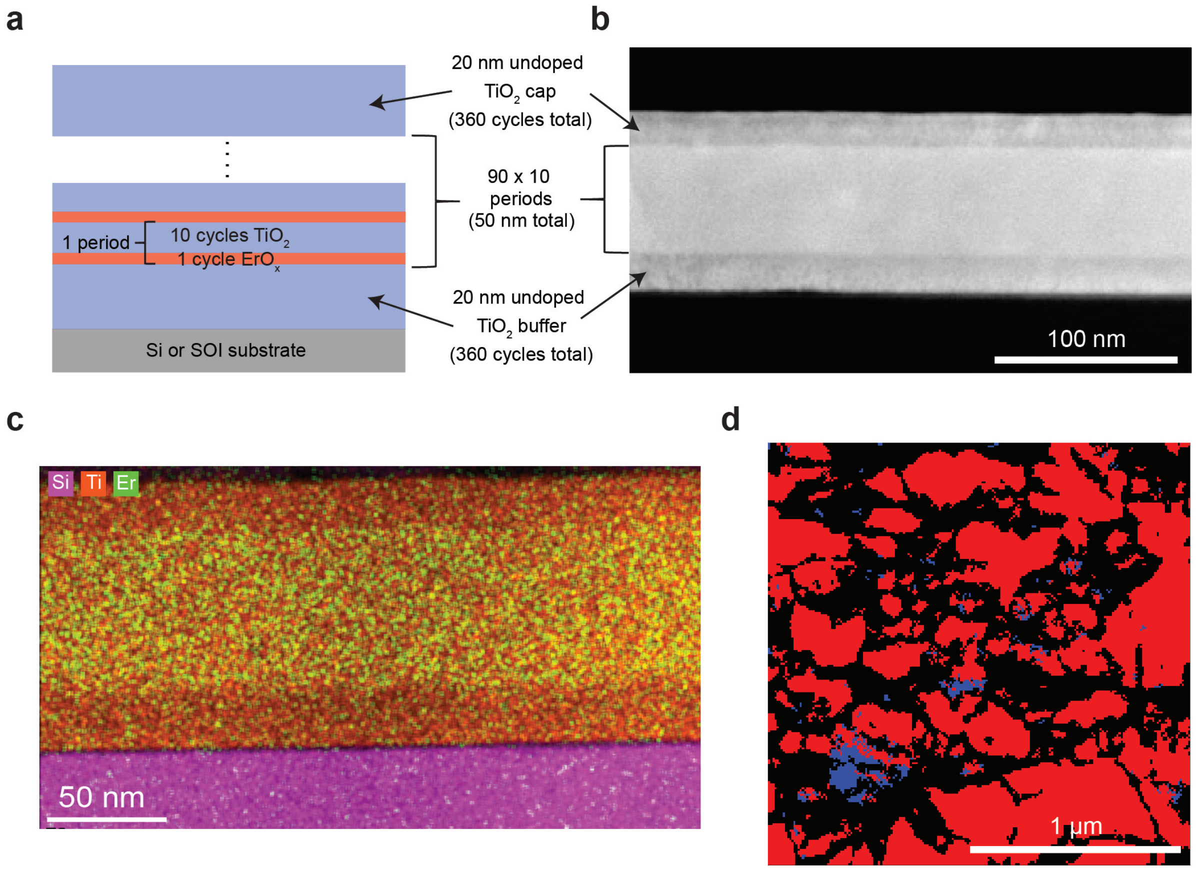

Figure 2.4: Electron microscopy of Er-doped thin films. (a) Schematic diagram of the '20/50/20' doped heterostructure used for SIMS elemental analysis and electron microscopy, consisting of a 20 nm undoped TiO_2 buffer layer, a 50 nm Er-doped TiO_2 layer, and a 20 nm pure TiO_2 capping layer. The thin film is grown on Si(100) or SOI. A thinner '10/10/10' heterostructure with the same 1 ErO_x to 10 TiO_2 layer ratio is used in the doped region for optical experiments. (b) A low magnification high-angle annular dark-field scanning transmission electron microscopy (HAADF-STEM) image of a sample cross section with an Er doping level of 2950 ppm after oxygen annealing. (c) Energy-dispersive X-ray spectroscopy (EDS) elemental map of the same annealed sample as in (b). The elemental distribution overlay shows Si in purple, Ti in orange, and Er in green, respectively. (d) Electron backscatter diffraction (EBSD) phase map of individual grains within the same '20/50/20' film as in (b-c). The red regions consist of individual anatase grains and the smaller and less numerous blue regions are individual rutile grains. The black regions are either amorphous or consist of multiple stacked grains of either phase within the thickness of the 90 nm film.

No.[a]	T(°C) [b]	Δt (s)[c]	Doping (ppm)[d]
1	160	8	39200 ± 15680
2	135	8	2950 ± 885
3	110	8	1.7 ± 0.51
4	110	2	0.59 ± 0.24

Table 2.1: Sample deposition and Er doping parameters
[a] The sample number.
[b] The Er precursor evaporation temperature.
[c] The Er precursor pulse length, same as Δt in Figure 2.1b.
[d] The Er concentration determined via SIMS.

2.3.4 Crystallinity and Phase Stability

The crystallinity of the host material significantly impacts the optical and quantum properties of Er ions, particularly their coherence and emission linewidth. In amorphous as-grown TiO_2, the local environment around Er ions is highly disordered, leading to inhomogeneous broadening, spectral diffusion, and shorter coherence times due to variations in crystal field interactions. Therefore, achieving high crystallinity through post-annealing is crucial for enhancing Er ion coherence and emission stability for quantum memory applications.

After post anneal, X-Ray Diffraction (XRD) is performed to evaluate the crystal phase of TiO_2. Figure 2.2d displays the XRD spectrum of an oxygen annealed '10/10/10' heterostructure thin film sample. The spectrum shows the characteristic peaks of anatase TiO_2[131] (marked with red boxes), though the signature is weak due to the modest thickness of the film, as well as the peak from the Si substrate (green box).[132] These results confirm that oxygen annealing enhances the polycrystallinity of the initially amorphous film, aligning with previous findings.[133]

To better visualize the crystalline morphology of the Er:TiO_2 thin films we also performed electron microscopy on the doped '20/50/20' films used for SIMS analysis. Specifically, high-angle annular dark-field scanning transmission electron microscopy (HAADF-STEM) imaging was used to provide additional atomic number contrast to better visualize the heavier Er dopants within the TiO_2 matrix (i.e. a brighter pixel corresponds to a higher Z number).

Using this technique, we can clearly see in Figure 2.4b the increased brightness of the 50 nm thick doped region in a 2950 ppm Er-doped film (same growth conditions as Sample No. 2 of Table 2.1). A corresponding energy-dispersive X-ray spectroscopy (EDS) elemental map of the same cross-section in Figure 2.4b is shown in Figure 2.4c, confirming the presence of Er in the doped region.

We also conducted HAADF-STEM imaging to compare the as-grown and 400 °C annealed samples (Figure 2.5a,b). Both cross-sections were extracted from the same growth film (Er doping level: 39,200 ppm, Sample No. 1 in Table 2.1) and focus on the undoped-doped interface near the substrate. In the as-grown film (Figure 2.5a), the structure is completely amorphous, exhibiting no discernible atomic regularity. In contrast, after 400 °C annealing, the film transitions to a crystalline state, as evidenced by the well-defined lattice spacing characteristic of a single-crystal anatase domain, which dominates the entire field of view (Figure 2.5b). The results further confirm the presence of large anatase grains, measuring tens of nanometers in thickness, extending from the Si substrate. Notably, the crystallinity of these grains remains unaffected by the relatively high Er doping concentration (Figure 2.5b,c).

The lateral extent of these grains can be visualized with electron backscatter diffraction (EBSD) phase mapping in an SEM operating at 10 kV (with an effective probe depth of a few tens of nanometers), as shown in Figure 2.4d. The majority of the 4 μm^2 area consists of anatase grains (49.8%) while also exhibiting a much lower percentage of smaller rutile grains (2.0%). The exact depth of the grains probed via EBSD varies based upon accelerating voltage and interaction with the Si substrate underneath, so it is unclear if the black regions in Figure 2.4d merely represent stacked anatase grains with different orientations or pockets of amorphous TiO_2. Regardless, it is particularly significant that these anatase grains can extend for hundreds of nanometers laterally, as these grains are larger and, overall, the sample offers higher phase purity than the mixed rutile and anatase grains sizes reported in molecular beam deposited TiO_2 on Si.[64] These results suggest that even though our as-grown thin films are amorphous, the oxygen annealing process can induce large anatase grain coarsening, and that these resultant grains might serve as a good local crystal host for erbium ions, all without increasing the top layer surface roughness.

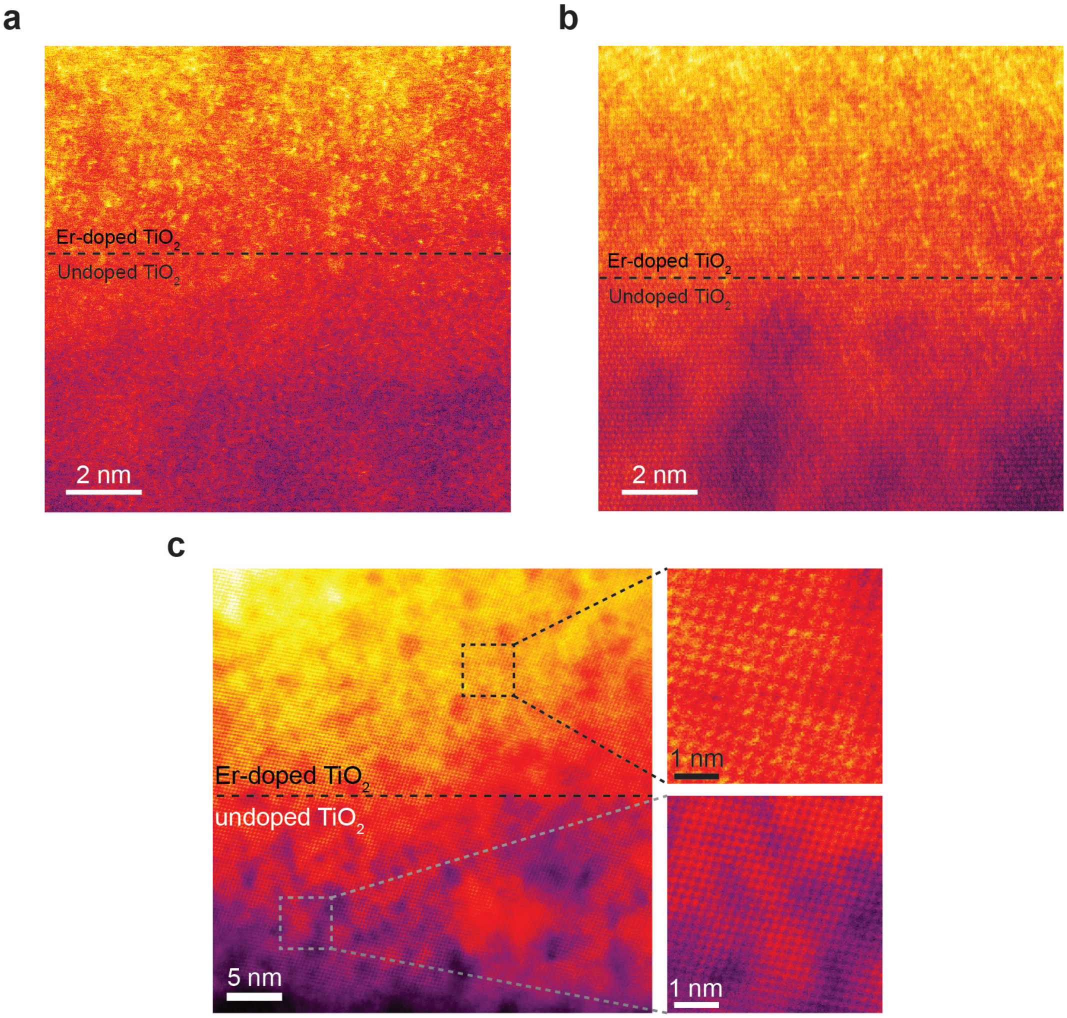

Figure 2.5: HAADF-STEM of Er doped TiO$_2$ thin films with false color heat map. All of the images focused on the lower boundary between the doped and undoped regions to analyze structural and crystallographic differences. (a) HAADF-STEM images of a cross section of an as-grown “20/50/20” sample, showing a completely amorphous structure without regularity in the single atom spacing. (b) HAADF-STEM image of a different piece from the same growth sample as in (a) after oxygen annealing. The doping level of the growth sample is 39,200 ppm. (c) HAADF-STEM image of a broader cross-section from the annealed "20/50/20" sample, with a doping level of 2950 ppm. Insets show atomic-resolution images of the crystalline region. In both (b) and (c), the cross-sections clearly shows a single crystalline anatase grain extending through 20 nm of the undoped TiO$_2$ near the substrate into the Er-doped region after oxygen annealing.

2.4 Probing Optical Properties: Photoluminescence Excitation (PLE) Measurements of Er Emitters in the Thin Film

Photoluminescence excitation (PLE) spectroscopy is an essential optical characterization technique used to study the optical transitions and electronic structures of quantum emitters. Unlike conventional photoluminescence (PL), which measures the emission spectrum at a fixed excitation energy, PLE involves scanning the excitation energy while monitoring the emission at a specific wavelength. This approach provides detailed insights into the excitation pathways, energy-level structures, and the efficiency of photon absorption and subsequent emission in quantum systems. For quantum emitter benchmarking, PLE spectroscopy is particularly valuable as it allows for the precise identification of resonant excitation energies, helping to distinguish individual quantum emitters from an ensemble. It can accurately characterize the emitter's absorption cross-section, excitation linewidth, and spectral purity, all of which are critical for evaluating performance in quantum applications.

Therefore, in addition to standard material characterization, we conducted PLE spectroscopy to investigate the optical emission properties of Er ions. This technique provides a critical benchmark for quantum memory applications, as reliable qubit readout strongly depends on clear and precise optical emission. Specifically, our PLE measurements focused on emitters within the telecom C-band on the aforementioned '10/10/10' heterostructures grown on Si substrates, wherein only the central 10 nm layer in the heterostructure contains Er dopants.

Figure 2.6 illustrates the optical measurement setup for characterizing ALD-grown thin film samples. The excitation source is a Toptica CTL 1500 tunable laser with piezo control for precise wavelength tuning. The laser beam passes through two acousto-optic modulators (AOMs) to enable fast intensity modulation, while an additional AOM placed before the superconducting nanowire single-photon detector (SNSPD) prevents residual laser leakage from reaching the detector. A 50:50 free-space plate beam splitter is used to split the

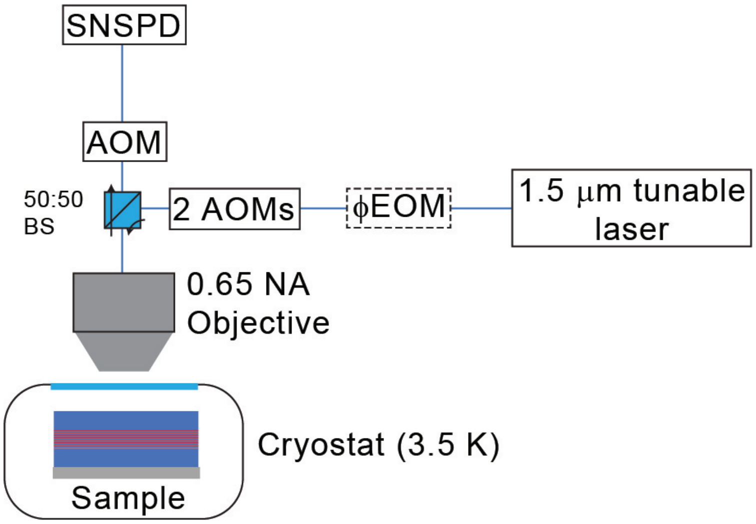

Figure 2.6: The optical measurement setup for the thin films.

optical path. A 0.65 NA objective focuses the laser onto the sample inside the Montana s50 Cryostation (3.5 K). During signal collection, the two AOMs after the laser suppress the excitation pulse, and the AOM before the SNSPD opens the optical path, allowing the emitted signal from Er dopants to be collected via the 50:50 beam splitter and directed to the superconducting nanowire single-photon detector for analysis. Note that the ϕEOM here is optional for spectral hole burning measurements. In this process, the ϕEOM applies controlled phase shifts, allowing selective depletion of specific frequency components within the inhomogeneously broadened Er ion ensemble. This creates a narrow spectral feature, which can be used to measure the spectral diffusion linewidth and assess the upper bound for homogeneous linewidth broadening.[74]

As shown in Figure 2.7, we measured PLE spectra for oxygen annealed thin films with the three highest doping levels (Table 2.1): 39200 ppm, 2950 ppm, and 1.7 ppm. The PLE intensity is the average number of detected photons per 3.5 ms collection window after each 1.5 ms laser pulse. It should be noted that for Sample No. 4 at 0.59 ppm the doping level is too low to be measured because of the long optical excited state lifetime of erbium emission, the thin optically active region, and the finite overall collection efficiency of the setup.

All of the as-grown samples had negligible emission in PLE as a result of the underlying disorder in the films. However, after the 30 minute oxygen anneal, all three samples show distinct peaks in the PLE spectra (Fig. 2.7). An example of the dramatic increase in PLE brightness for an as-grown versus annealed film is shown in Figure 2.8a, where the doping level is 39200 ppm. The as-grown PLE spectrum did not show any emission peaks and the brightness of the emission was close to the background level, which confirms that the oxygen annealing process is essential to not only form crystalline grains within the sample but also to optically activate the embedded Er ions. Note that the periodic oscillations in the PLE signal are due to Fabry-Perot fringes resulting from partial reflections within the finite thickness of a beamsplitter used in the setup.

The variation in emission intensities among the three samples (Fig. 2.7) is mainly attributed to the difference in the doping concentration. In general, higher Er doping typically leads to brighter overall emission; however, as seen by comparing Figures 2.7a and 2.7b, an order of magnitude increase in doping concentration from 2950 ppm to 39200 ppm does not show a commensurate increase in overall brightness for the emission near 1532 nm. Rather, this reduction in brightness is possibly due to ion-ion quenching and cooperative photon up-conversion, which are common at high Er doping concentrations,[134,135] as the estimated ion-ion spacings at 2950 ppm and 39200 ppm are 1.9 nm and 0.8 nm, respectively.

For each of the three samples, a higher spectral resolution PLE spectrum (i.e. 0.01 nm step size) near the 1532 nm peak is provided in the inset. Due to the finer spacing, the peak fluorescence varies slightly from that of each corresponding coarse spectrum. Most notable is a pair of closely spaced peaks near 1532.2 nm and 1532.6 nm, similar to what was observed previously in textured growth of polycrystalline TiO_2.[63] Previous work on Er-doped TiO_2 nanoparticles has experimentally determined the Y1 → Z1 transition to be at 6525 cm^{-1} (1532.57 nm),[136] similar to the predominant peak at 1532.6 nm in our scans. Future temperature-dependent PL and PLE scans are necessary to confirm this level

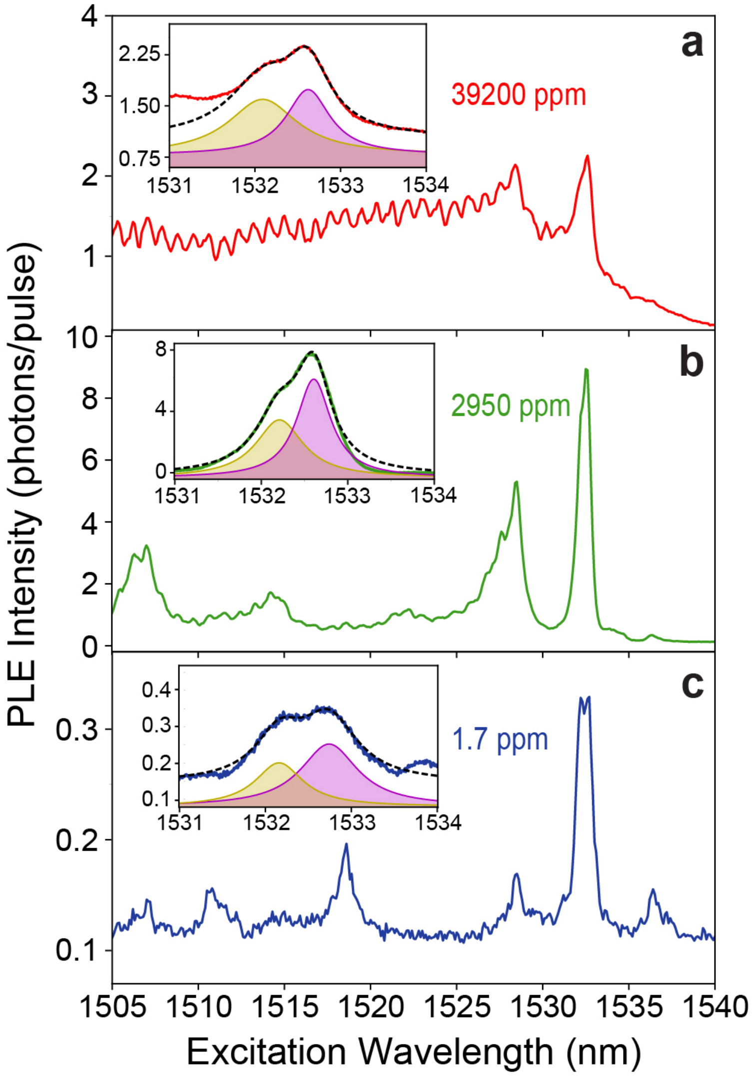

Figure 2.7: Photoluminescence excitation (PLE) spectra of annealed '10/10/10' Er:TiO_2 thin films. In each of the main panels is a broadband PLE scan from 1505 nm to 1540 nm, with a scan step size of 0.1 nm. The thin film Er doping levels for the three samples are (a) 39200 ppm, (b) 2950 ppm, (c) and 1.7 ppm according to Table 2.1. Insets: corresponding higher resolution PLE scans (step size of 0.01 nm) around the emission peak at 1532.6 nm, giving inhomogeneous linewidths of 79.3 ± 2.4 GHz, 61.4 ± 1.7 GHz, and 102.2 ± 5.4 GHz for the three samples No. 1-3, respectively. Each spectrum is fit to a pair of Lorentzian lineshapes (dashed, black line) with the resultant individual fits highlighted for clarity (purple and yellow, shaded curves).

assignment.[60] However, this value differs from the exact energy of the Y1 → Z1 transition reported for epitaxial anatase Er:TiO_2 growth on $LaAlO_3$ at 6518.9 cm^{-1} (1534.00 nm).[116] This discrepancy could be due to the strain relaxation afforded by the amorphous growth in our polycrystalline anatase films.

Fits of these closely spaced peaks enables us to estimate the inhomogeneous linewidth of the 1532.6 nm transition in each of our three samples (in order of decreasing doping) as 79.3 ± 2.4 GHz, 61.4 ± 1.7 GHz, and 102.2 ± 5.4 GHz, respectively (Fig. 2.7a-c, insets). The signal-to-noise ratio for the 1.7 ppm sample is poor (Fig. 2.7, inset), as this sample was pumped with ten times higher laser intensity to get sufficiently large detectable signal above background. Therefore, we suspect that this particular transition is power broadened, and waveguide-based PLE measurements at lower power (Figure 2.8b), suggest an inhomogeneous linewidth closer to 44 GHz for the 1.7 ppm sample. In general, the inhomogeneous linewidths of these samples prepared via ALD are broader than epitaxial growth of anatase TiO_2 on $LaAlO_3$ (12.7 GHz for a 4000 ppm film with similar buffer/capping layer thicknesses)[116] and molecular-beam deposited growth of highly textured Er-doped anatase TiO_2 on silicon (11.1 GHz with comparable buffer/capping layer thicknesses and doping).[63] However, it is important to note that they are all much narrower than the previously reported results for Er in ALD-grown Al_2O_3, which show broad emission on the scale of THz.[112,113] Overall, these findings demonstrate the positive impact of the annealing process in promoting the formation of a more ordered lattice structure and enhancing the optical emission characteristics of Er ions in the anatase TiO_2 matrix.

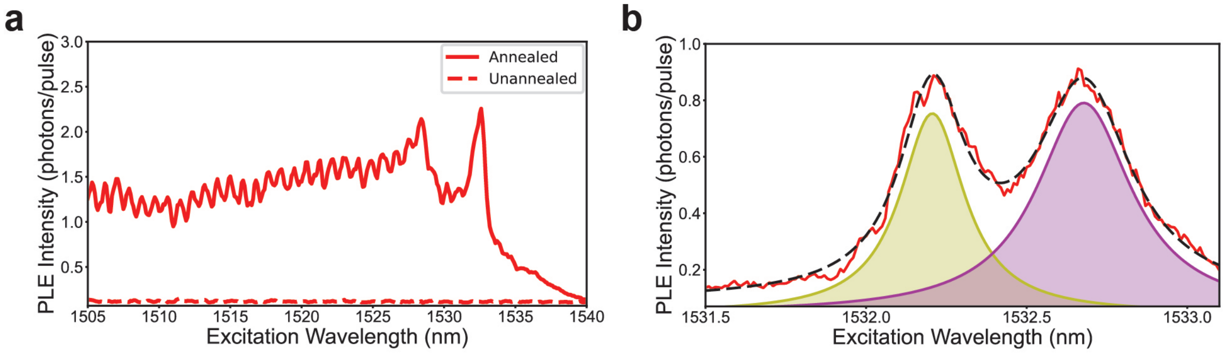

Figure 2.8: (a) PLE spectra of annealed versus as-grown “10/10/10” Er:TiO_2 thin films. The Er doping concentration of the film is 39200 ppm, corresponding to the condition No.1 in Table 2.1. The annealed sample PLE spectrum is shown in solid red lines while the unannealed sample from the same growth wafer is shown in red dashed line. (b) PLE scan of an annealed "10/10/10" Er:TiO_2 thin film with 1.7 ppm doping integrated on waveguide for better signal to noise ratio. The PLE scan shows two peaks near 1532.2 nm and 1532.6 nm. The peak at 1532.6 nm gives an inhomogeneous linewidth of the emission peak of 44.0 ± 0.7 GHz via Lorentzian fits.

2.5 Concluding Remarks Regarding Thin-Film Deposition

wTo conclude, this chapter showcases a reliable method for growing Er-doped TiO_2 using ALD. One of the most significant findings is the ability to dope these films with Er ions over a large range by controlling the Er-dopant precursor temperature and pulse length. This is a level of doping control not usually provided by ALD and opens up new possible applications at both ends of the doping spectrum (few percent to sub-ppm). Over the demonstrated doping range, our ALD process offers potential advantages over other methods, such as molecular beam deposition of doped films and implantation of erbium ions in undoped films, in terms of translation to industry because of lower cost and increased scalability. Our characterization of the material proprieties after post-growth oxygen annealing revealed the films to be Er-doped anatase phase TiO_2 with a smooth surface, which can be maintained even after the formation of polycrystalline grains that are hundreds of nanometers wide. Furthermore, our optical measurements revealed distinct optical transitions and relatively narror inhomogeneous linewidth for the characteristic emission peaks around 1532 nm for the annealed films. These results suggest that Er:TiO_2 thin films grown using ALD are a promising material platform for on-chip quantum memory applications. It is particularly important to note that this critical 400°C oxygen annealing process is CMOS-compatible,[137] further ensuring industrial scalability. A future area of exploration is the possibility of longer annealing times to further increase anatase grain size or higher annealing temperatures to explore the transition to rutile grains.

CHAPTER 3

PHOTONIC CRYSTAL CAVITIES INTEGRATION: ADVANCING SCALABLE QUANTUM PHOTONIC PLATFORMS

As discussed in Section 1.3, the long excited-state lifetime of Erbium ions presents a significant challenge for fast spin-state readout, which is crucial for quantum memory applications. A promising solution to this limitation is the integration of Erbium doped thin film with a resonant photonic cavity, where the Purcell effect can significantly enhance the spontaneous emission rate by reducing the optical lifetime, thereby enabling faster photon emission.

This chapter explores the design, simulation, and integration of photonic crystal cavities with thin films deposited using ALD, as introduced in Chapter 2, as well as those deposited via the MBE system in our lab. To establish a foundational understanding, the chapter begins with a brief introduction to cavity quantum electrodynamics (cavity QED), explaining the underlying physics of photonic cavities and the Purcell effect. Following this, the principles of cavity design and simulation will be presented, detailing key parameters and underlying rationale. Finally, the fabrication process of the photonic cavity will be discussed, along with potential imperfections that may arise during the process.

3.1 Physics behind Photonics Cavity – an Overview of Cavity Quantum Electrodynamics (QEDs)

This section provides an overview of cavity QED and explores the fundamental physics of the atom-cavity interaction, highlighting the role of cavities in enabling Purcell enhancement for Er^{3+}.

To begin, consider a system consisting of a two-level atom and an optical resonator, forming a fundamental cavity QED system. In free space, deterministic atom-photon interactions are typically limited, as the atom's absorption cross-section is much smaller than the photon beam size. However, in a cavity, multiple reflections confine the light, significantly enhancing the interaction probability. The number of round trips a photon makes within the cavity is characterized by $\mathcal{F}/\pi$, where $\mathcal{F}$ is the finesse of the cavity, defined as[138].

$$\mathcal{F} = \frac{\pi\sqrt{|r|}}{1-|r|} \tag{3.1}$$

where r is the reflection from the cavity boundaries. For simplicity, isotropy in all directions is assumed here.

To describe the interaction between the atom and the cavity, the coupling constant g is defined as

$$g = \frac{\mu_{ce}E}{\hbar} = \sqrt{\frac{\mu_{ce}^2\omega}{2\epsilon_0\hbar V}}u(\boldsymbol{r}) \tag{3.2}$$

Here $\hbar$ is the reduced Planck constant, μ_{ce} is the atomic electric dipole matrix element of the transition from the ground state to the excited state, E is the electrical field of a single photon in the cavity mode volume V, ϵ_0 is the permittivity of free space, ω is the cavity frequency, and $u(\boldsymbol{r})$ is the electrical mode function with the maximum normalized to 1.[31]

Considering the cavity field decay rate κ and the atom state decay rate γ, where[31]

$$\kappa = \frac{\pi c}{2L\mathcal{F}} \tag{3.3}$$

$$\gamma = \frac{\mu_{ce}^2\omega^3}{6\pi\epsilon_0\hbar c^3} \tag{3.4}$$

The cooperativity C can be thus defined as

$$C = \frac{g^2}{2\kappa\gamma} \tag{3.5}$$

For the atom-cavity system in Purcell regimes, the emitted photon should be emitted out of the cavities before being reabsorbed by the atom. Therefore, $\kappa >> g >> \gamma$ and $C >> 1$ are required for reliable Purcell enhancement and strong atom-photon interactions. The atomic dipole decay rate into the cavity γ_c can be derived:[139,140]

$$\gamma_c = \frac{g^2 \kappa}{\kappa^2 + \Delta^2} \tag{3.6}$$

Δ is the detuning between the atomic transition and the cavity resonant frequency. The on resonance ($\Delta = 0$) will give $\gamma_c = 2C\gamma$. For $C >> 1$, the enhanced decay rate γ_c is much greater than the intrinsic decay rate γ. That is the magic of the Purcell effect on the emission of photon qubit from the atom qubit.

Although the derivation above provides a clear picture of the atom-cavity coupling mechanism, calculating the Purcell factor F_P directly from this perspective can be cumbersome. To simplify the process, an alternative approach — focusing on the density of optical states rather than explicit coupling dynamics — can be employed. This approach, while not explicitly emphasizing the coupling between the two systems, provides a more straightforward calculation of F_P.

First, the spontaneous emission rate of an emitter in free space is given by Fermi's golden rule[138]:

$$\Gamma_0 = \frac{2\pi}{\hbar} |\mathbf{d} \cdot \mathbf{E}|^2 \rho(\omega) \tag{3.7}$$

where $\mathbf{d}$ is the dipole moment of the emitter, $\mathbf{E}$ is the electric field at the emitter location and $\rho(\omega)$ is the density of optical states at frequency ω.

In free space, the density of states per unit volume is:

$$\rho_{free}(\omega) = \frac{\omega^2}{\pi^2 c^3} \tag{3.8}$$

leading to the free-space spontaneous emission rate:

$$\Gamma_0 \propto \frac{\omega^3}{c^3} \tag{3.9}$$

However, inside an optical cavity, the electromagnetic field is confined, modifying the density of optical states. If we assume a single cavity mode with volume V and quality factor Q, this will lead to an enhanced emission rate:

$$\Gamma_c = \frac{2\pi}{\hbar} |\mathbf{d} \cdot \mathbf{E}|^2 \rho_{cavity}(\omega) \tag{3.10}$$

where the density of states in the cavity is approximated as:

$$\rho_{cavity}(\omega) \approx \frac{Q}{V} \frac{\lambda^3}{8\pi^3}. \tag{3.11}$$

If we further assume the emission wavelength matches the cavity resonance wavelength, the Purcell factor F_P is directly related to the cavity quality factor Q and corresponds to the ratio of the optical density of states in the cavity to that in free space[138]:

$$F_P = \frac{\rho_{cavity}(\omega)}{\rho_{free}(\omega)} = \frac{3}{4\pi^2} \frac{\lambda^3}{V} Q \tag{3.12}$$

To emphasize, here the quality factor demonstrates the energy storage capability of the cavity, as:

$$Q = 2\pi \frac{Stored \quad energy \quad in \quad the \quad cavity}{Energy \quad loss \quad per \quad cycle} \tag{3.13}$$

It can also be extrapolated to $Q = \frac{f_0}{\delta f}$. f_0 is the center frequency and δf is the full width at half maximum (FWHM). From the Purcell factor equation above, a high-Q nanocavity with small mode volume is essential for large Purcell factors. This enhancement is needed to speed up the single photon emission rate and improve collection efficiency into the cavity mode.

3.2 Photonics Design and Simulation for Quantum Memory

3.2.1 The Photonic Crystal Cavity Design and Simulation

Photonic crystal cavities emerge as a direct optical analogue of periodic potentials in solid-state physics, where the periodicity of a structure governs wave propagation. In solid-state systems, the periodic potential of a crystal lattice leads to the formation of electronic band structures, dictating the allowed and forbidden energy states for electrons. Similarly, in photonic crystals—periodic dielectric structures—the modulation of the refractive index gives rise to photonic bandgaps, where specific frequency ranges of light are forbidden from propagating.[141,142] By introducing a localized defect within this periodic dielectric arrangement, a discrete optical mode can be created within the bandgap, leading to strong light confinement.[143,144] This mechanism underpins the operation of photonic crystal cavities, allowing light to be confined within subwavelength-scale mode volumes while achieving exceptionally high Q-factors, which make the essential condition for realizing significant Purcell enhancement.

For our specific application, we selected a one-dimensional (1D) photonic crystal cavity, also known as a nanobeam photonic crystal cavity, to achieve an optimal balance between Purcell enhancement and efficient photon extraction. In a nanobeam photonic cavity, the periodic structure is embedded within a waveguide, enabling the emitted photon to directly couple into the waveguide's propagation mode. This design facilitates efficient photon routing to downstream components such as optical fibers and single-photon detectors, ensuring seamless integration with larger photonic circuits.

Our photonic crystal cavity design is originally inspired by the optomechanical crystal resonators studied at Caltech[145]. The device consists of a wide waveguide patterned with periodically spaced, identical elliptically shaped holes that act as photonic crystal mirrors[59,64]. Each hole has a major diameter of 397.5 nm and a minor diameter of 195.0 nm. The structure is designed with 30 nm thick Er:TiO_2 on top of a standard silicon-on-insulator (SOI) platform, comprising a 220 nm silicon layer atop a 2 μm SiO_2 buried oxide layer and a silicon substrate. The waveguide has a width of 660 nm, with a lattice constant of 355 nm for the elliptical holes. Simulations using MIT Photonic Bands (MPB) predict a photonic bandgap spanning wavelengths from 1360 nm to 1620 nm (see Figure 3.1a) for light polarized in the plane of the film and normal to the waveguide (TE-like modes).

To create a localized optical cavity, we introduce a defect using a 14-hole parabolic taper, gradually reducing the lattice constant from 355 nm in the mirror regions to 320 nm at the cavity center. This tapering modifies the photonic band structure, effectively confining light within the cavity mode. The resulting Q-factor is 1.3×10^5 with the resonance at 1560 nm. The mode volume of the cavity is computed to be 0.038 μm^3, and calculated using:

$$V_{\text{mode}} = \frac{\int \mathrm{d}V\, \epsilon(\boldsymbol{r})|E(\boldsymbol{r})|^2}{\max\left(\epsilon(\boldsymbol{r})|E(\boldsymbol{r})|^2\right)}. \tag{3.14}$$

The simulations are performed with 3D Lumerical FDTD. The results of the cavity spectrum is demonstrated in Figure 3.1b.

It should be noted that there are two primary practical nanofabrication rationales for our approach to effective index modulation in the manner described above (device fabrication will be described later in Section 3.3): (1) Having each hole identically sized means they aren't subject to differences area dry etch rates for experimental realization within the same cavity. This can be particularly challenging for etching through multiple layers with different etch chemistry. (2) Using a parabolic taper in the lattice constant to define the cavity defect is an effective approach because the pixel pitch for common nanocavity patterning techniques (such as electron beam lithography) can be well controlled.

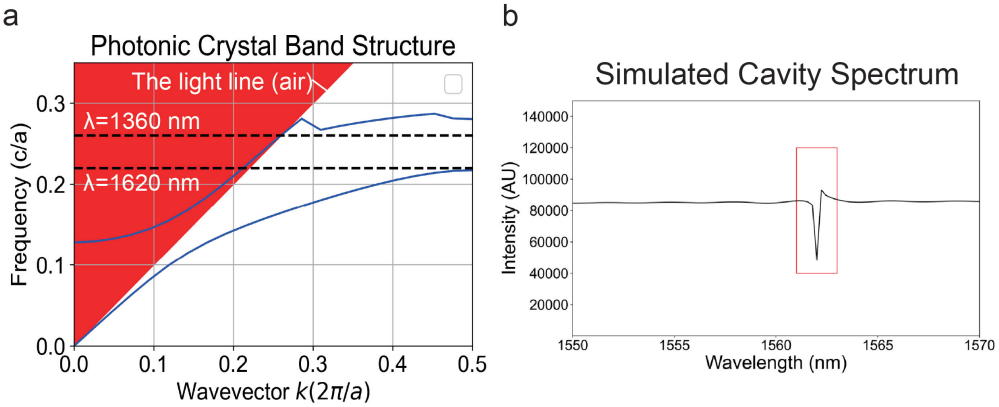

Figure 3.1: Photonic crystal cavity simulations. (a) Simulated photonic band structure using MPB. The red-shaded region represents the light cone in air, where no guided modes can exist due to the constraint of light propagation. The blue curves correspond to the calculated photonic bands, showing a well-defined photonic bandgap for TE-polarized light between 1360 nm and 1620 nm (marked by dashed lines). This confirms the presence of a bandgap where confined optical modes can exist within the photonic crystal cavity. (b) Simulated cavity spectrum using Lumerical FDTD, based on the cavity design described in the main text. A distinct resonance feature is observed around 1560 nm, highlighted by the red box. The extracted Q factor is approximately 130,000, indicating strong optical confinement and low radiative losses.

3.2.2 The Waveguide to Fiber Coupling Design and Simulation

Efficient waveguide-to-fiber coupling is essential for the practical realization of Erbium-based quantum memory, as it directly enables seamless integration with existing fiber-optic communication networks. While Erbium ions naturally emit in the telecom band, making them ideal for fiber-based quantum memory applications, achieving high coupling efficiency remains challenging due to mode mismatch and scattering losses between the nanoscale waveguide and the standard optical fiber. Optimizing this interface is crucial for minimizing insertion loss and ensuring reliable quantum state transfer in scalable quantum networks. While there is extensive work on cladding-based approaches to fiber-to-waveguide coupling within Si photonics[146,147,148]. These cladding-based approaches can be hard to implement without simultaneously covering our nanocavity with thick cladding layers. The deposition of these thick layers on the nanocavity eliminates our ability to tune the cavity's resonant wavelength at cryogenic temperatures via controlled gas condensation as mentioned later in Chapter 4. Also, the cladding deposition process may have an impact on the optical and/or spin properties of our Er-doped oxide layers.

To enhance the lensed fiber-to-waveguide coupling efficiency, we implemented a suspended inverse waveguide taper extending beyond the sample edge (Fig. 3.2). This design follows the adiabatic inverse taper approach used in previous work for fully suspended Si waveguides of 220 nm[149] and 250 nm[59] thickness. In our simulations, we neglected the presence of the 30 nm-thick TiO_2 layer due to its low refractive index relative to Si.

We initialized our simulations with parameters inspired by prior studies: a waveguide end facet width of 200 nm[149] and a taper length of 14 μm[59] to ensure mechanical stability. Again using Lumerical 3D FDTD simulations, we determined the minimum lateral undercut of the buried oxide layer required to effectively guide light into the cavity. As shown in Figure 3.3a, an initial undercut length of ≥ 4 μm minimizes optical losses as the mode transitions into the waveguide section in contact with the buried oxide layer.

To refine the design, we varied the waveguide end facet width (Fig. 3.3b) and taper length (Fig. 3.3c) while keeping the undercut length fixed at 4 μm. A TE-polarized Gaussian source with a 1.25 μm waist radius was positioned 14 μm from the waveguide end to emulate our commercial lensed fiber (OZ Optics), and transmitted power was monitored 4 μm beyond the taper's full width. Our results indicate that an end facet width of 200 nm and a taper length of 14 μm yield a maximum one-way coupling efficiency of 80% (Fig. 3.3b). While extending the taper length marginally improves efficiency (Fig. 3.3c), the 14 μm taper is finally chosen for mechanical stability.

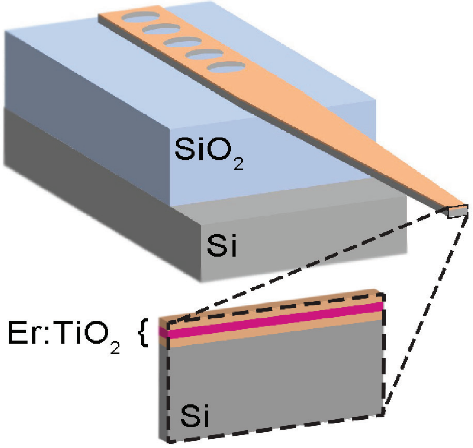

Figure 3.2: The photonic crystal cavity and waveguide are designed based on a 30 nm $Er:TiO_2$ layer atop an SOI chip. To enhance fiber coupling efficiency, the suspended waveguide extends beyond the SiO_2/Si substrate edge. The adiabatic inverse taper design, highlighted in the protruding waveguide region, gradually narrows the waveguide width, expanding the optical mode for improved coupling with a lensed fiber.

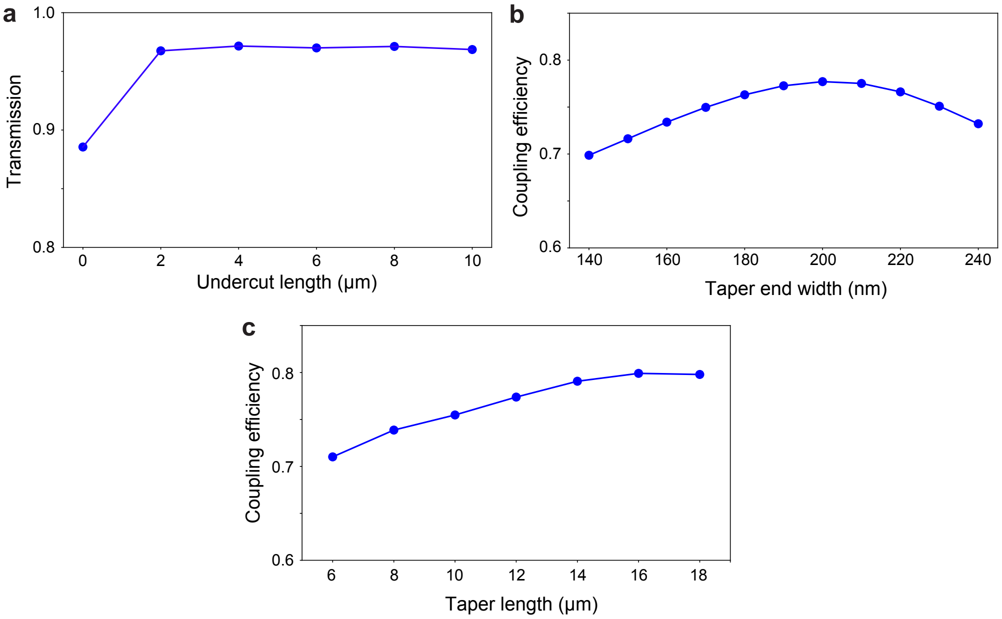

Figure 3.3: Inverse taper FDTD simulation results. (a) Guided mode transmission as light is routed in a Si waveguide from an undercut region to oxide region. (b) Fiber-to-waveguide coupling efficiency versus waveguide end facet width assuming a fixed taper length of 14 μm and a fixed undercut of 4 μm. (c) Fiber-to-waveguide coupling efficiency versus overall taper length width assuming a fixed end facet width of 200 nm and a fixed undercut of 4 μm

3.3 Photonic Crystal Cavity Fabrication and Integration: Realizing Quantum Memory in Scalable Photonic Devices

The insights gained from photonic simulations provide a critical foundation for the subsequent fabrication and integration of photonic devices. However, translating these theoretical designs into functional devices requires precise nanofabrication techniques that account for material properties, process variations, and real-world constraints. The following section details the fabrication and integration steps used to realize these simulated structures, ensuring their viability for experimental characterization and practical applications.

To account for run-to-run variations in the etch rate, our fabricated devices incorporate a deliberate elliptical hole size parameter sweep. As a result, the cavity resonances on each chip span from 1510 nm to 1550 nm, ensuring a high probability of coupling with resonant Erbium ion emitters.

The fabrication process for creating cavities and suspended inverse tapers, along with an optical device image, is shown in Figure 3.4. All fabrication steps are carried out in the Center for Nanoscale Materials cleanroom at Argonne National Laboratory.

The photonic cavity and waveguide fabrication is demonstrate in Figure 3.4a, similar to our previous work[64]. Our TiO_2 thin films are deposited on silicon-on-insulator (SOI) substrates (Soitec) featuring a lightly boron-doped 220 nm-thick Si device layer, a 2 μm buried oxide layer, and a more heavily boron-doped Si handle to minimize charging effects during subsequent fabrication steps. The thin film deposition can be performed using either MBE or ALD, followed by an annealing process if necessary.

After deposition, a SiO_2 hard mask is deposited on the surface using plasma-enhanced chemical vapor deposition (PECVD) to facilitate pattern transfer during the etching process. A ZEP520A resist layer is then spin-coated on top of the hard mask, and electron beam lithography (EBL) is used to define the photonic cavity patterns in the resist. After resist development, the chip undergoes a two-step inductively coupled plasma reactive ion etching

(ICP RIE) process.

In the first etching step, a CHF_3/O_2 plasma is used to selectively etch the SiO_2 hard mask, simultaneously removing most of the remaining resist due to the reactive plasma environment. The second step involves a Cl_2-based RIE process to etch through the Er:TiO_2 layer, followed by an HBr/O_2 mixture RIE to etch the underlying silicon and form the final cavity pattern.

To protect the device during processing, we deposit a 20 nm (200 cycles) thermal ALD alumina layer at 175°C, as conventional polymeric resist layers do not provide sufficient protection—particularly during the vapor HF etching step. This alumina layer is optimized in both thickness and growth temperature to mitigate pinholes that could expose the device layers to vapor etchants during undercutting.

Immediately after cleaving (Lattice Ax), we perform an isotropic etch of the Si handle layer using a XeF_2 vapor etch tool, which results in the characteristic scalloped edge seen in Figure 3.4b. A prolonged delay between cleaving and the XeF_2 etch allows the formation of a native oxide layer on the freshly cleaved Si surface, reducing the otherwise deterministic XeF_2 etch rate. Following the Si handle undercut step, we perform vapor HF etching (SPTS uEtch system) to selectively remove the buried thermal oxide layer. After undercutting, the ALD alumina protection layer is gently stripped using Aluminum Etchant Type A (Transene) at 40°C.

Finally, to mitigate potential defects introduced during nanofabrication, we anneal the devices in pure O_2 at 400°C using a rapid thermal annealing system (Annealsys). As discussed in Section A, our simulations suggest that longer tapers (>14 μm) offer a slight improvement in coupling efficiency. However, they become significantly more fragile during the vapor HF undercut process due to strain induced in the suspended SiO_2 and alumina layers following the Si handle undercut.

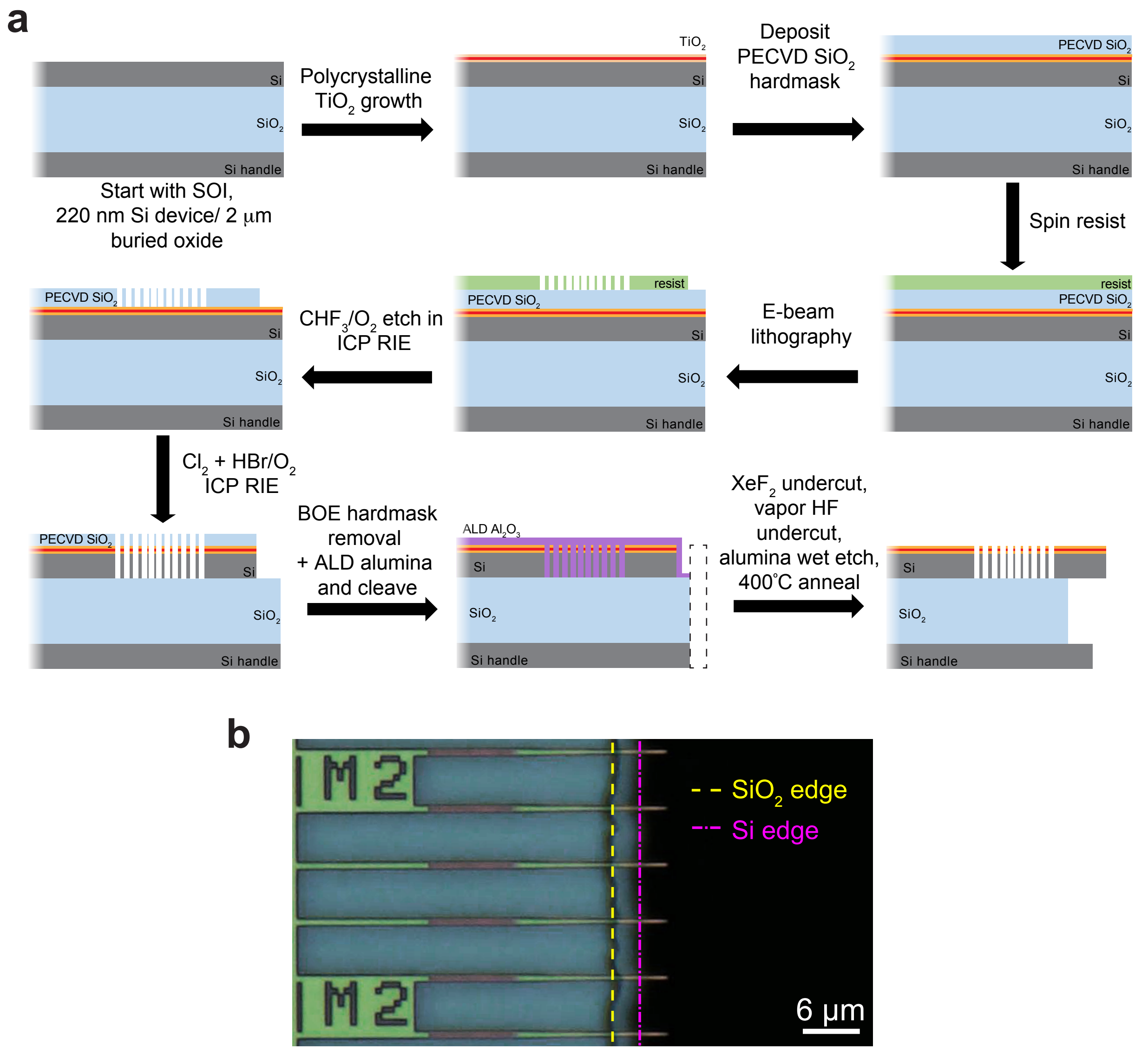

Figure 3.4: Fabrication of photonics cavity and waveguide devices. (a) Step-by-step fabrication process illustrating patterning, etching, and undercutting to extend the on-chip waveguide beyond the edge. (b) Optical microscope image of the fabricated device, showing fully suspended waveguides. The dashed yellow (magenta) lines indicate the undercut boundary for the SiO_2 (Si handle) edges.

3.4 Concluding Remarks of Cavity Design and Fabrication

In this chapter, we presented the design, simulation, and fabrication of photonic crystal cavities integrated with erbium-doped thin films for quantum memory applications. Through simulations, we demonstrated that high-Q 1D photonic crystal cavities have the potential to achieve significant Purcell enhancement, enabling faster photon emission and efficient quantum state transfer. Additionally, the implementation of an adiabatic inverse taper design minimized optical losses at the fiber-to-waveguide interface, further optimizing the memory-photon qubit interaction.

By combining robust photonic design principles with advanced nanofabrication techniques, we successfully realized scalable quantum memory devices compatible with existing fiber-optic networks. The integration of a novel undercut etch process with top-down cavity fabrication enabled precise control over the device geometry. To further assess device functionality and investigate the optical properties of Er-doped emitters, we now turn to Chapter 4, where experimental measurements will provide deeper insights into photonic device performance and quantum coherence characteristics.

CHAPTER 4

OPTICAL MEASUREMENT OF INTEGRATED PHOTONIC DEVICES: PROBING QUANTUM MEMORY EMITTERS

Optical characterization is essential for evaluating the performance of integrated photonic devices, providing critical insights into key parameters such as resonance properties, quality factors, and coupling efficiency. Additionally, these measurements enable a deeper understanding of the optical properties of erbium ion emitters and the Purcell enhancement resulting from their coupling to photonic crystal cavities. This chapter outlines the experimental techniques used to characterize photonic crystal cavities, investigate Er ion emission properties, and quantify Purcell enhancement.

This chapter specifically focuses on the optical measurements of devices incorporating thin films deposited via ALD and MBE, as discussed in previous chapters:

—For ALD-integrated photonic devices, we demonstrate successful thin-film integration and strong performance, including Purcell enhancement and relatively narrow spectral diffusion linewidths, reinforcing ALD's potential for future quantum memory and on-chip lasing applications. This part of results are mainly reproduced from Ji et al.[65], with the permission of ACS Publications.

—For MBE-integrated photonic devices, we report an anomalous three-fold suppression of the ensemble Purcell factor at zero cavity detuning and high pump fluence, providing new insights into emitter-cavity coupling dynamics. This part of results are adapted with permission from Solomon et al.[101], with the permission of Optica Publishing Group.

4.1 Nanocavity-mediated Purcell Enhancement of ALD of Er:TiO_2 Thin Films

To demonstrate the potential use of these ALD grown Er:TiO_2 films as a platform for telecom on-chip photonic applications, we integrated the same '10/10/10' thin film heterostructure with silicon photonic crystal cavities based on SOI and measured the resultant Purcell enhancement for ensembles in different doping regimes. The details of the ALD deposition is demonstrated in Chapter 2. For this study, we fabricated devices from two samples with different Er concentrations: Sample A (2950 ppm Er, deposition condition No. 2 in Table 2.1) and Sample B (1.7 ppm Er, No. 3 in Table 2.1). The waveguide geometry, photonic crystal cavity, and mirror design lattice parameters are introduced in Chapter 3. In order to compensate for run-to-run etch rate variations, our fabricated devices are designed to have a deliberate elliptical hole size sweep, and there are resonance wavelengths ranging from 1510-1550 nm on each chip. In this work, the desired cavities are nearly resonant at 1532 nm. In order to improve the one-way coupling efficiency of our silicon nanophotonics, we performed a multi-step process to fully suspend the inverse taper of the waveguide to better mode match to a lensed optical fiber, as introduced in Chapter 3. To mitigate any potential detrimental defects introduced by the nanophotonic fabrication, we also oxygen annealed the chips at 400°C after full device fabrication. Scanning electron microscopy (SEM) images of the final devices are shown in Figures 4.2a-b.

4.1.1 Optical setup for photonic device measurements

Following the fabrication process, the devices were placed inside a closed-cycle cryostat (Montana Instruments s100 Cryostation) with a base temperature of 3.5 K for optical characterization using a lensed optical fiber mounted on a 3-axis nanopositioner.

The optical measurement setup used for device characterization is illustrated in Figure

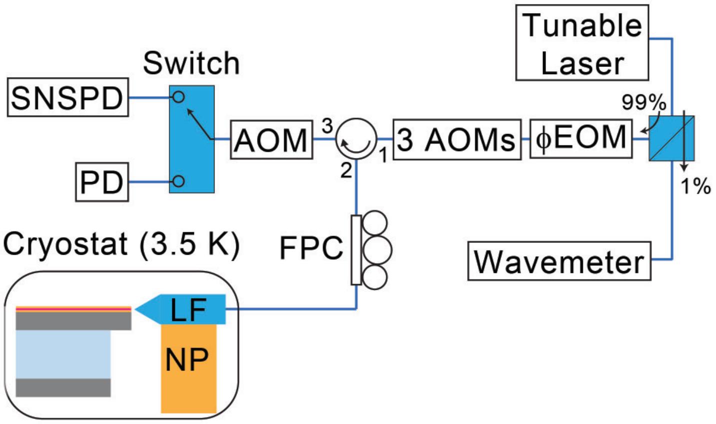

Figure 4.1: The optical measurement setup for the photonic devices. AOM: acousto-optic modulator, FPC: fiber polarization controller, LF: lensed fiber, NP: nanopositioner, ϕEOM: electro-optic phase modulator, PD: amplified photodiode, SNSPD: superconducting nanowire single-photon detector.

4.1. A tunable laser, combined with three fiber-coupled acousto-optic modulators (AOMs), generates short optical pulses, which are delivered to the sample via a lensed fiber (LF) mounted on a nanopositioner (NP) for precise alignment. The collected return signal can be directed to different detection pathways, including a photodiode (PD) for power monitoring or a superconducting nanowire single-photon detector (SNSPD) for high-sensitivity photon counting. A fiber polarization controller (FPC) ensures optimal polarization alignment with the photonic cavity mode. Additional optional components (indicated by dashed boxes) can be integrated into the setup, such as an electro-optic phase modulator (ϕEOM) for generating sidebands in transient spectral hole burning experiments and a fiber wavelength division multiplexer (WDM) for off-resonant excitation. More details on the experimental configuration can be found in previous work[64].

4.1.2 Cavity Benchmark

Photonic cavities on each sample are screened for resonances 1-2 nm to the blue of the desired optical transition ($\lambda = 1532.6$ nm), after which they are tuned (redshifted) onto resonance via nitrogen gas condensation. Then, each cavity can be characterized by scanning the laser wavelength across the cavity resonance, with their cavity quality factor calculated from the Lorentzian fit of the reflection spectrum as measured with an amplified photodiode. As shown in Figure 4.2c, Device A shows a quality factor of $Q=30,220 \pm 890$ while Device B gives $Q=40,680 \pm 990$. Overall, the samples etched from Sample A (2950 ppm) had a lower Q than those from Sample B (1.7 ppm) by 30-40% regardless of detuning from the 1532 nm transition, so this is not due to increased absorption from a higher Er concentration. Rather this uniform discrepancy in Q between the two samples is most likely due to the fact that a more complete $\mathrm{ErO_x}$ layer (in the case of Sample A) hinders the $\mathrm{Cl_2}$ reactive-ion etching (RIE) step in the doped region of the $\mathrm{TiO_2}$ film, leading to more hardmask erosion during the RIE process and a subsequently lower etch selectivity. Overall, the quality factors of the cavities are comparable to devices fabricated using thinner (≈22 nm) molecular beam deposited $\mathrm{TiO_2}$ layer with 35 ppm Er doping.[64]

4.1.3 Spectral Diffusion Linewidth Measurement through TSHB

The homogeneous linewidth of an optical transition is important for many photonics applications and, in particular, for optically addressing single ion quantum memories. A measurement of the homogeneous linewidths of individual emitters would provide the best characterization of disorder within each ion's local environment. However, that measurement is not possible for the high doping concentrations where single emitters cannot be spectrally isolated. Instead, one can perform transient spectral hole burning (TSHB) by sweeping the detuning of two symmetric sideband tones (generated via an electro-optic phase modulator) from the laser carrier frequency to measure the degree of spectral diffusion, which establishes an upper bound on the homogeneous linewidth[74]. We performed control TSHB measurements via Er embedded in $\mathrm{TiO_2}$ on top of a bare waveguide (no holes). We use 1 ms resonant laser pulses and detect the integrated fluorescence —in a 3.95 ms collection window

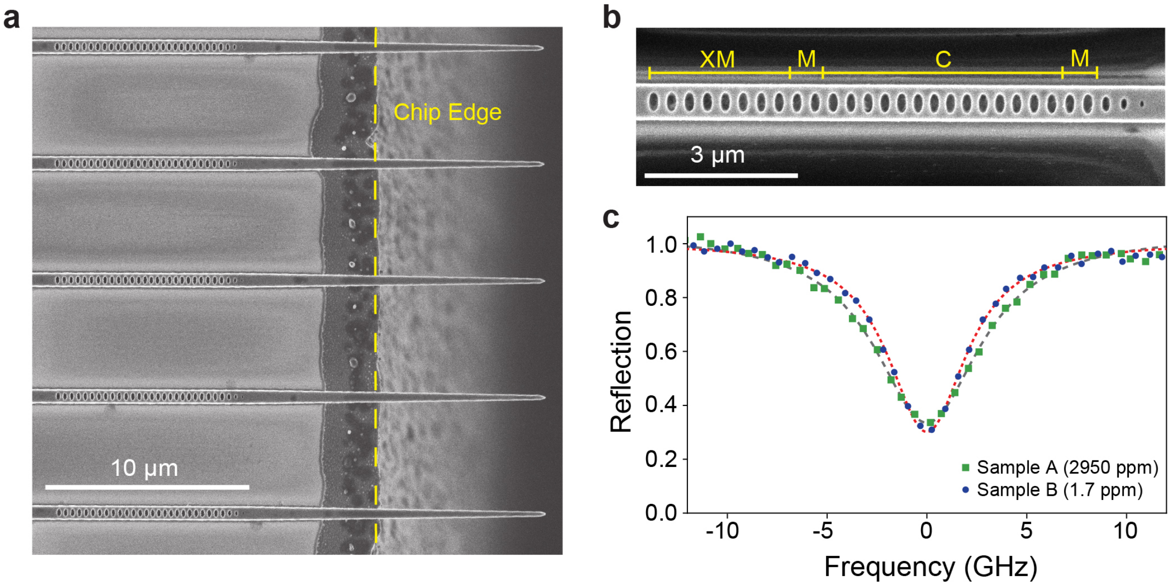

Figure 4.2: ALD TiO_2-Si photonic crystal cavities. (a) Top view SEM image of fabricated devices from Sample B, highlighting the inverse tapered waveguide extending off the edge of the SOI chip (to the right of the yellow dashed line). The dark gray region extending 2-3 μm from the chip edge is due to lateral etching of the original buried oxide layer as part of the undercut process. (b) An SEM image highlighting the nanophotonic cavity composed of elliptically shaped holes etched through the TiO_2 and Si device layers. The 14-hole cavity region (denoted by C) consists of a parabolic taper of the lattice constant, there are two mirror holes (M) on each side of the cavity region, and extra mirror holes (XM) are included on the left-hand side of the device because all measurements are performed in a one-sided coupling configuration via the inverse waveguide taper seen in (a). (c) Normalized laser reflection spectra of the photonic cavities from Samples A (green squares) and B (blue circles) coupled via lensed optical fiber at a temperature of 3.5 K. For these reflection scans, the cavities are tuned onto resonance with the Er in anatase TiO_2 transition of interest ($\lambda =$ 1532.60 nm). Using Lorentzian fits, the cavities from Samples A and B have quality factors of Q=30220 ± 890 (gray, dashed line) and Q=40680 ± 990 (red, dashed line), respectively.

after the end of the pulse —as a function of the sideband-carrier detuning frequency (Δ). In Figure 4.3a, the TSHB results are shown for Sample A (green squares) and Sample B (blue circles) with the emitters on bare waveguide devices. The half-width at half-maximum (HWHM) linewidths are 0.56 ± 0.02 GHz and 0.235 ± 0.012 GHz, respectively. The higher doped sample reveals a linewidth that is broader by a factor of two, presumably as a result of the stronger ion-ion interactions. However, in both cases this spectral diffusion linewidth is much narrower than the cavity linewidth, which is 6.47 ± 0.19 GHz and 4.80 ± 0.11 GHz for Samples A and B, respectively. Thus for both samples, coupling between the emitter and cavity lies in the "bad cavity" regime, where the Purcell enhancement of the optical decay rate scales as Q/V, where Q is the quality factor and V is the mode volume.

We also performed a TSHB measurement on a cavity-coupled Er ensemble for Sample B (Figure 4.3b) when the cavity is resonant with the transition at 1532.6 nm. For this measurement, the continuous wave (CW) laser power is increased 28-fold while the laser pulse lengths are shortened to 2 μs —specifically to address the sub-ensemble of ions that are well-coupled to the cavity. Finally, the normalized intensity as a function of Δ has been corrected to account for the lineshape of the cavity (shown in Fig. 4.2c, green squares), which modifies the sideband-carrier detuning intensity dependence. In this case, the Lorentzian fit (dashed line) yields a spectral diffusion linewidth of 0.223 ± 0.007 GHz, which is comparable to the TSHB linewidth for Sample B (0.235 ± 0.012 GHz) in Figure 4.3a. Both the bare and cavity-coupled spectral diffusion linewidths are comparable to the narrowest value (0.18 GHz) measured previously for molecular beam deposited thin films with thicker buffer layers,[63] suggesting that the quality of the ALD films as a host for Er are comparable to those grown via molecular beam deposition.

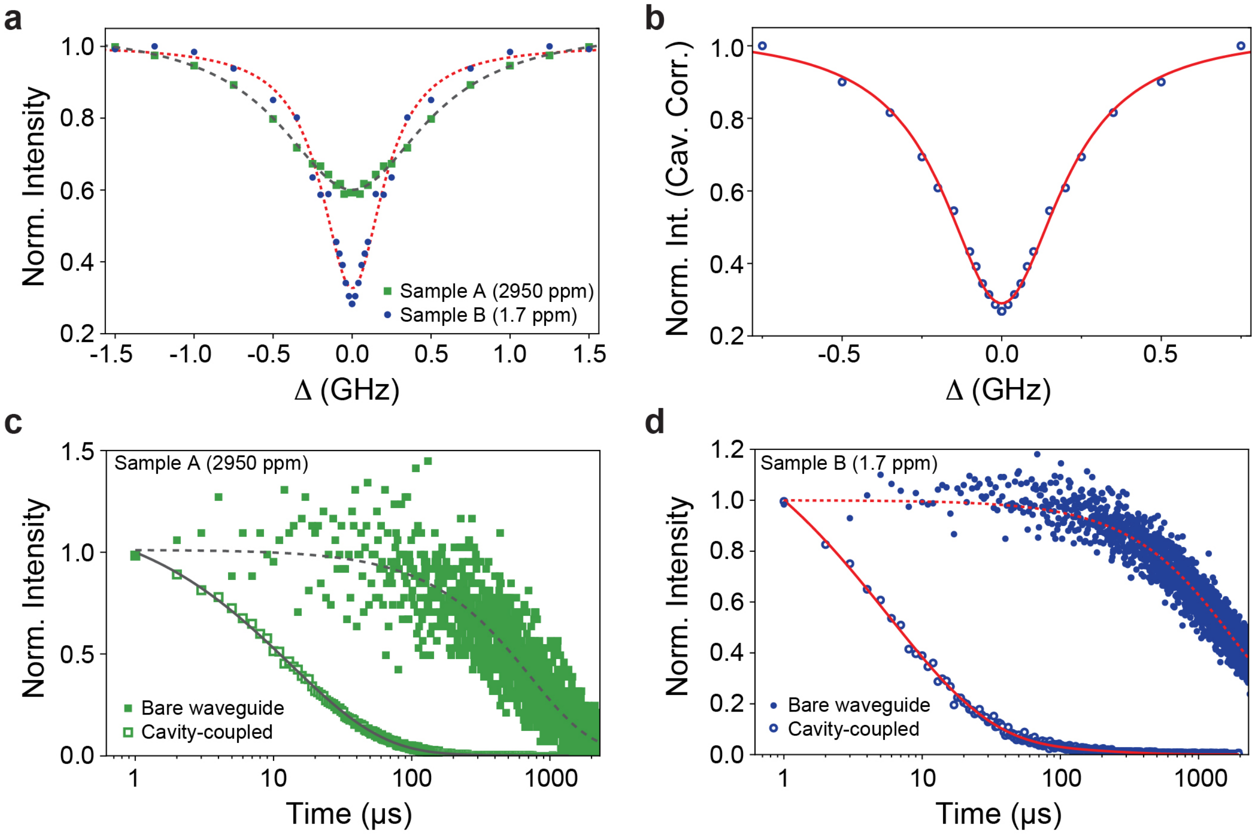

Figure 4.3: Optical measurements on fabricated devices at T = 3.5 K. (a) TSHB measurement results performed on bare waveguide devices fabricated from Sample A (green squares) and Sample B (blue circles). The data show the normalized PLE intensity versus the carrier-sideband detuning (Δ) and are symmetric about zero, but they are plotted over the full range for visual clarity. The Lorentzian fit (dashed lines) shows a spectral diffusion HWHM of 0.56 ± 0.02 GHz for Sample A and 0.235 ± 0.012 GHz for Sample B. (b) Similar TSHB measurement results for a cavity-coupled Er ensemble on Sample B, where the normalized intensity has been corrected to account for the lineshape of the same cavity shown in Fig. 4c (blue circles). The Lorentzian fit (solid, red line) yields a spectral diffusion linewidth of 0.223 ± 0.007 GHz. (c) Comparison of the normalized ensemble lifetime of Er ions in a bare waveguide device (solid green squares) versus the cavity-coupled device (open green squares) for Sample A (2950 ppm). The bare waveguide lifetime is 725 ± 7 μs and the cavity-enhanced lifetime is 13.19 ± 0.07 μs. (d) Comparison of the normalized ensemble lifetime of Er ions in a bare waveguide device (solid blue circles) versus the cavity-coupled device (open blue circles) for Sample B (1.7 ppm). The bare waveguide lifetime is 1718 ± 5 μs and the cavity-coupled lifetime is 5.7 ± 0.2 μs. For (c) and (d), the bare waveguide lifetimes are fit to a single exponential and the cavity-enhanced decay times are fit using a stretched exponential as discussed in the text.

4.1.4 Optical lifetime and Purcell Enhancement

The Purcell enhancement of cavity-coupled ions is an increase in the spontaneous emission rate of the emitter due to coupling with the cavity mode. It is a key parameter for enhancing light-matter interaction in quantum and optoelectronic devices. To characterize the Purcell enhancement introduced from the nanophotonic cavities for both Sample A (2950 ppm) and Sample B (1.7 ppm), we performed measurements of the Er emission lifetime using resonant laser pulse excitation. The baseline (non cavity-coupled) optical lifetime was measured from the same control devices as the TSHB measurements, as illustrated by the closed squares (circles) in green (blue) in Figure 4.3c (d) for sample A (B). Using a single exponential fit, we found that the natural emission lifetime for the ions on the bare waveguide was approximately 725 μs for Sample A and 1718 μs for Sample B. An optical lifetime of 1.7 ms for Sample B is consistent with what is measured in ALD and molecular beam deposited thin films at sub-100 ppm doping levels, suggesting that even after patterning the re-annealed sample does not seem to show signatures of excessive fabrication-induced non-radiative decay. We speculate that the reduced Er optical lifetime seen in sample A is likely due to ion-ion quenching at higher concentration that serves as a non-radiative pathway.[150]

We measured the Purcell-enhanced decay rate (open markers) for each sample using the same cavities in Figure 4.2c when each cavity is resonant with the Er optical transition at 1532.6 nm. In contrast to the single exponential character of the decay from bare waveguides, the ensembles coupled to each of the cavities show a stretched exponential character (as has been seen previously[64,151]). This is due to the varying coupling strength of ions in the ensemble to the cavity at different spatial positions along the cavity and dipole orientation with respect to the TE-like fundamental mode. The time constant for the stretched exponential enhanced lifetime for ions coupled to the resonant cavity was 13.19 ± 0.07 μs for Sample A and 5.7 ± 0.2 μs for Sample B, indicating that the best coupled ions in the ensemble have a Purcell factor of 55 ± 0.6 and 301 ± 11, respectively. Overall, we can see that the Purcell factor for Sample A is about 6 times lower than Sample B, and the primary culprits are the reduction in the baseline lifetime (725 μs versus 1718 μs) and the modest reduction in cavity Q (3.02×10^4 versus 4.07×10^4). However, this does not fully account for the difference in the cavity-enhanced decay. Because the Purcell factor measured here comes an ensemble of ions coupled to the cavity, with ions positioned near the cavity nodes being more weakly coupled, the measured stretched exponential decay time only provides a lower bound on the lifetime for the most strongly coupled ions. As a result, it is feasible that the thousand-fold higher concentration of ions in Sample A results in more averaging of the ensemble Purcell factor and hence dilutes the contributions of the best coupled ions to yield a lower enhancement. Overall the Purcell factor measured for Sample B is approximately 50% better than previously fabricated devices from molecular beam deposited TiO_2 and the Er ions (35 ppm) embedded in the rutile phase grains even though the cavity quality factors were similar.[64] Likely this is due to the aforementioned averaging from the higher doping concentration.

4.1.5 Conclusion of this section

To conclude, the successful coupling of these ALD-grown Erbium doped TiO_2 thin films with moderately high quality factor 1D Si photonic crystal cavities that are enabled, in part, because of the low surface roughness after annealing, as introduced in Chapter 2. The resultant Purcell enhancement demonstrates the significant improvement in the spontaneous emission rate of the Er ions due to the evanescent coupling with the fundamental nanophotonic cavity mode. This enhancement plays a crucial role in achieving more efficient and controlled light-matter interactions. In particular, the low-doped sample exhibited a much higher Purcell enhancement in excess of 300, further confirming the potential of these Er:TiO_2 thin films integrated with nanophotonic cavities at dilute concentrations suitable for quantum technologies.

4.2 Anomalous Purcell Decay of Strongly Driven Inhomogeneous Emitters Coupled to a Cavity

For this study, we utilize "10/10/10" Er-doped TiO_2 films grown via molecular beam deposition, which incorporate both rutile and anatase crystalline grains, as reported in previous work[64]. The deposition process is conducted at a substrate temperature of 390°C, with a metallic Er cell temperature of 900°C. At this Er temperature, the flux is calibrated to yield an Er concentration of 120 ppm in rutile and 130 ppm in anatase, accounting for the density difference between the two phases. This corresponds to an average Er-Er spacing of approximately 4.4 nm. While the full details of the molecular beam deposition process for Er-doped TiO_2 are beyond the scope of this study, they can be found in our group's prior work[100]. The fabrication process is well introduced in Chapter 3. The SEM images of the final devices are shown in Figures 4.4a.

4.2.1 Photonic Cavity and Waveguide Characterization

The optical measurement setup is identical to that shown in Figure 4.1. The cavity full-width half-maximum (FWHM) linewidth measured is 2.94 ± 0.05 GHz, when centered at $\lambda = 1520.52$ nm, and this corresponds to a Q $=(6.71 \pm 0.11) \times 10^4$ (Fig. 4.4b) with a waveguide-cavity mode coupling efficiency, $\eta = 34\%$, yielding a decay rate from the cavity of $\kappa_c = 0.34\kappa$. The cavity is tuned around 1520.5 nm to match the Erbium ion optical transition in rutile TiO_2.In a simplified ambient setup with a closed-loop nanopositioner, measurements of the suspended in-coupling structures show a typical lensed fiber-to-waveguide coupling efficiency of approximately 75%, which is close to the simulated maximum of 80%. However, when the same characterization is performed in the cryostat at 3.5 K, the efficiency decreases to around 65%.

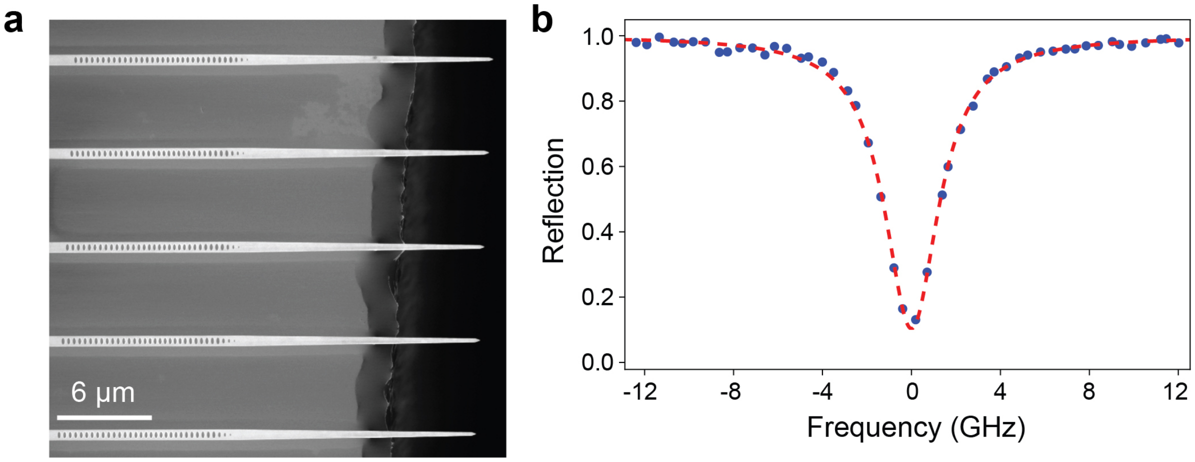

Figure 4.4: Fabricated photonic cavities characterization. (a) Scanning electron microscope (SEM) image of a nanophotonic cavity consisting of elliptically shaped holes etched through the TiO_2/Si device layers. The structure includes a waveguide inverse taper extending from the chip edge to facilitate efficient optical coupling.(b) Normalized laser reflection spectrum of the cavity tuned onto resonance with the $Z_1 \rightarrow Y_1$ optical transition for Er in rutile phase TiO_2 ($\lambda = 1520.5$ nm at a temperature of 3.5 K. The dashed line represents a Lorentzian fit, yielding a cavity quality factor of Q=$(6.71 \pm 0.11) \times 10^4$.

4.2.2 PLE measurements

We explore the cavity-coupled optical relaxation dynamics in these ensembles using resonant photoluminescence excitation (PLE) measurements as depicted in Figure 4.5a. We use three acousto-optic modulators (AOM) in series to generate 5 μs laser pulses from our tunable CW laser. After the end of the laser pulse, we wait 2 μs before opening a fourth AOM in the collection path to our superconducting nanowire single-photon detectors (SNSPDs), which are not gated. It should be noted that both the laser pulse length and wait time before detection are sufficiently long to allow for the fast decay of pump photons from the cavity. We can repeat each pulse sequence many times (typically $N_{\mathrm{shots}} = 4000$) to create a histogram of the ensemble fluorescence lifetime and measure the integrated intensity. Using this approach, resonant PLE from a laser sweep near 1520.52 nm, yields a broad Er^{3+} ensemble linewidth of 50 GHz, as was shown previously[64], and is represented by the wide gray Lorentzian shown in Figure 4.5b. The inhomogeneous linewidth Δ_{inh} is much broader than the cavity linewidth (κ=2.94 ± 0.05 GHz), and we use nitrogen gas condensation on the cavity to tune the refractive index and slowly redshift the cavity resonance through the center of the inhomogeneous linewidth. For the majority of measurements, the laser is locked at $\lambda =$ 1520.52 nm using a wavemeter (WS-8-10, High Finesse) calibrated against a fixed frequency reference laser (SLR-1532, High Finesse). We periodically interrupt PLE measurements to perform CW laser reflection measurements, such as the one shown in Figure 4.4c, to precisely measure the cavity-laser detuning parameter, Δ_c.

4.2.3 Anomalous Purcell Double-peak Decay

With the foundations of PLE measurements, we can now perform lifetime measurements at a variety of input laser powers for each cavity detuning. For better understanding, we quantify the incident laser brightness in terms of ϕ/κ, the photon flux given by the number photons of incident on the cavity per cavity lifetime ($1/\kappa$).

As shown in Figure 4.5c, for the lowest laser power used ($\phi = 19\kappa$) we measure a fast decay time close to resonance ($\Delta_c \approx 0$) and slower decay at modest cavity detunings of $\approx \pm 4$ GHz. In contrast, even though the fluorescence intensity is brighter for the highest laser power ($\phi = 1.1 \times 10^4 \kappa$), we see faster decay when the cavity is detuned from the transition than on resonance. Following previous work[64,151], we can fit the experimental data using a function of the form: $A \exp\left[-(t/\tau_1)^d\right] + B \exp(-t/\tau_2) + C$. For our case, the stretched exponential with lifetime τ_1 represents the fastest ensemble fluorescence decay rate ($\Gamma = 1/\tau_1$) mediated by coupling to the cavity. The stretching exponent (d) attempts to capture the distribution of individual ion-cavity coupling strengths (g) within the ensemble, and the single exponential decay constant represents the much slower decay from Er ions along the inverse taper waveguide because the ions are located everywhere in the film. It is important to note that for these measurements, the specific fit for τ_1 is robust regardless of the other parameters (A, B, d, τ_2, and C)[64]. If we also measure the optical lifetime of the fluorescence decay rate in a bare waveguide without a cavity, $\Gamma_0 = 1/\mathrm{T}_1$, where $\mathrm{T}_1 = 5.370 \pm 0.013$ ms measured from this sample, then the cavity-mediated Purcell enhancement, Γ/Γ_0, can be computed for each incident flux and cavity detuning, and the resultant plot is shown in Figure 4.5d.

Most interesting is that at higher incident fluxes we see a double-peak decay profile appear, and the decay rate appears to slow when the cavity is resonant with the driving field. This double-peaked detuning profile is significantly wider than the lower power cases: a single Lorentzian fit of the $\phi = 19\kappa$ case yields a FWHM $= 3.96 \pm 0.24$ GHz, which is 35% wider than the cavity linewidth measured via reflection.

When we plot the total PLE intensity for the resonant case, we can see the onset of saturation (Fig. 4.5e), where the dashed red line is a fit to a standard PLE function of the form

$$P(\phi) = \frac{p_1}{p_2 + 1/(\phi/\kappa)} \ . \tag{4.1}$$

If we use the total experimental photon collection efficiency of our system (0.023) and the detected number of photons, we can infer ~ 2200 photons generated in the cavity per pulse at the highest pump power ($\phi = 1.1 \times 10^4 \kappa$). Since we are in a saturation regime, we can generally conclude that the number of ions that are addressed with our optical pulse is close to this value.

Using our device geometry and doping density, we very coarsely estimate that there are 7×10^4 total ions along the cavity, though our uncertainty is quite large given the unknown proportion of Er ions residing in the rutile vs anatase grains. However, if we use this value and make another coarse estimate that if the spectral window that is being addressed with these highest power pulses is approximately the cavity linewidth ($\kappa = 2.94$ GHz), a rough calculation suggests that around 2600 ions are effectively coupled to the cavity mode. Given that our estimates of the ion population and the number of photons generated in the cavity are in reasonable agreement—particularly in a regime where the ensemble appears to be saturating—we infer that the actual number of participating ions is likely close to 2000. This estimate provides a useful basis for simulations aimed at explaining the dependence of the Purcell factor on detuning. While a detailed theoretical simulation is beyond the scope of this thesis, further analysis can be found in the published work[101].

4.2.4 Conclusion of This Section

Through systematic lifetime measurements at various input laser powers and cavity detunings, we have gained deeper insight into the interplay between photon flux, ion-cavity coupling, and Purcell enhancement in our system. Our results confirm that at lower excitation powers, the fastest decay occurs near resonance, with slower decay observed at moderate detunings. However, at higher photon fluxes, a double-peaked decay profile emerges, where the decay rate appears to slow when the cavity is resonant with the optical drive, deviating from the expected Lorentzian behavior.

By analyzing the PLE intensity, we infer that the system reaches a saturation regime, with approximately 2200 photons generated per pulse in the cavity at the highest pump power. Given our device geometry and doping density, we estimate a total ion population of 7×10^4 within the cavity region, with approximately 2600 ions effectively coupled to the cavity mode. The agreement between these estimates and the observed fluorescence characteristics suggests that the number of participating ions is approximately 2000, providing a reliable input parameter for the theoretical modeling introduced in the published work[101].

Overall, these findings offer valuable experimental benchmarks for understanding ensemble ion-cavity interactions and optimizing Purcell-enhanced emission.

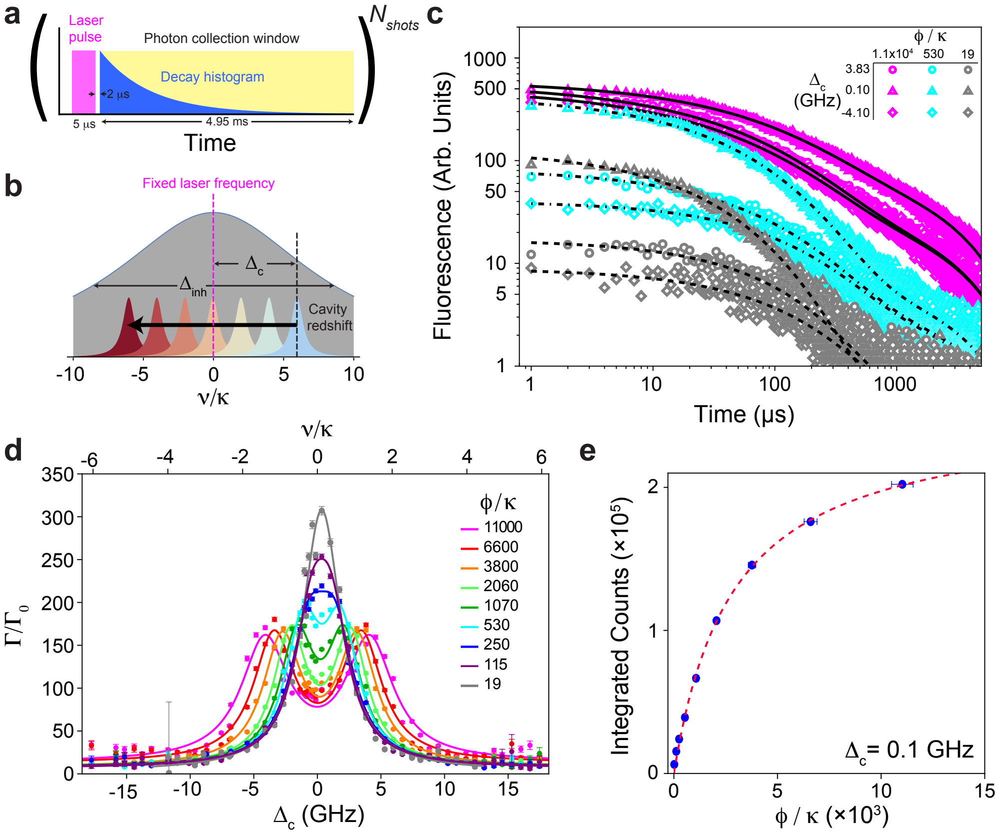

Figure 4.5: PLE Measurements on cavity-coupled Er ensembles at 3.5 K. (a) Schematic of our photoluminescence excitation measurement sequence. We first generate a 5 μs long laser excitation pulse (magenta). After a 2 μs wait time, we open an additional modulator in the collection path to start the photon collection window (yellow) to enable detection of the fluorescence from the ensemble. This single pulse sequence is repeated over N_{shots} measurements to build up a histogram of the decay (blue). (b) Schematic of the cavity tuning mechanism in the measurement. The laser is locked to a particular frequency at the center of the ensemble's inhomogeneous distribution. This distribution is broad relative to the cavity linewidth (κ) and is represented by the wide gray Lorentzian ($\approx 17\kappa$). The cavity is slowly redshifted through the resonance through gas condensation tuning, and its frequency relative to the laser is given by Δ_c. The experimental extent of Δ_c is $\approx 12\kappa$ as represented with the blue-to-red transition of the cavity Lorentzian. (c) Nine example experimental time traces for three different incident photon flux values (ϕ) and cavity-laser detuning values (Δ_c). The black lines are fits to the experimental data. (d) The spontaneous decay rate enhancement (Γ/Γ_0) as a function of the cavity-laser detuning (Δ_c, bottom x-axis and top x-axis in units of κ) for increasing photon fluxes (ϕ) . The Γ/Γ_0 values are extracted from the stretched exponential time constants fit to experimental data such as those in (c). The solid lines for each flux are from a pair of Lorentzian lineshapes fit to the experimental data. (e) Integration of all detected counts within collection time window for each PLE time trace with the single detuning condition of $\Delta_c = 0.10$ GHz as a function incident flux, the red dashed line is a saturation fit.

CHAPTER 5

ISOLATING A SINGLE ERBIUM ION: THE INITIAL STEP FOR QUANTUM MEMORY QUBIT READOUT

To develop a practical quantum memory, the isolation of a single atomic defect is critical. This approach is advantageous not only for simplifying the system model but also for enabling high-fidelity operations. Following the successful integration of on-chip nanophotonic structures and the realization of Purcell-enhanced emission, the next focus in advancing the quantum memory system will be achieving single-ion isolation and characterizing its single-photon emission properties.

In this Chapter, we demonstrate that the deposition of Er:TiO_2 thin films on SOI wafers, subsequently patterned into nanophotonic waveguides and photonic crystal cavities, provides a platform capable of isolating single Er^{3+} ions. At a temperature of 3.4 K, we tune the photonic crystal cavity within the inhomogeneous ensemble of ions and observe isolated peaks in photoluminescence excitation (PLE) scans with linewidths on the order of $\sim$ 100 MHz, with a reduction of the optical emission lifetime by a factor $>$ 400 and antibunching of the photon autocorrelation $g^{(2)}(0) < 0.5$, revealing the emission of single photons. These results present Er:TiO_2 on SOI as a widely scalable platform that can be incorporated into mature semiconductor fabrication processes for the advancement of quantum technologies.

This chapter is primarily reproduced from Ji et al.[102], with permission from AIP Publishing.

5.1 Materials and Devices Preparation

The anatase TiO_2 thin films are grown on commercial SOI wafers (220 nm silicon layer with 2 μm buried oxide) using molecular beam deposition and consist of three layers: a middle Er-doped layer sandwiched between undoped buffer and capping layers below and

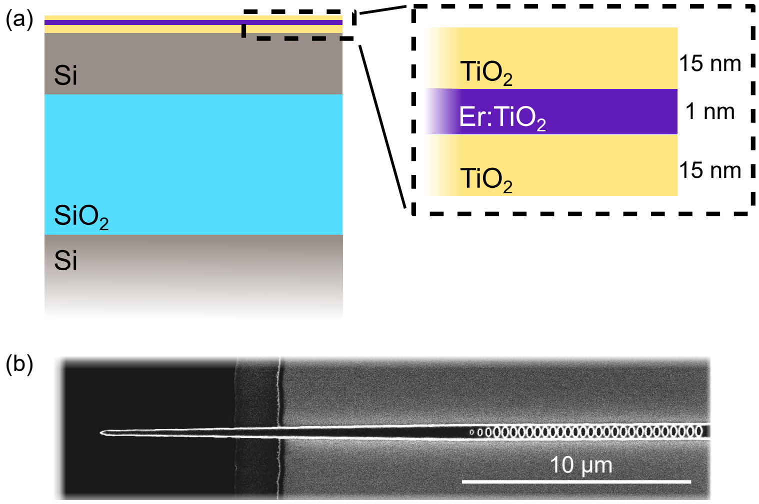

Figure 5.1: Overview of the platform to optically isolate single Er^{3+} ions. (a) Outline of the device heterostructure. The heterostructure consists of a TiO$_2$ film grown on top of an SOI wafer with a 1 nm thick Er^{3+} doped layer sandwiched between two 15 nm thick undoped layers. The doping level of the middle layer is 2 ppm. (b) SEM image of a representative fabricated device showing a 1D photonic crystal cavity embedded in a silicon optical waveguide.

above, respectively.[100] We use MBE instead of ALD primarily because MBE enables precise control over doping levels, especially in the low-doping regime, which is essential for achieving single ion isolation measurements. The doped layer has been shown to exhibit no significant erbium clustering. In this study, we investigate a heterostructure in which the undoped layers are 15 nm thick and the doped layer is 1 nm thick ("15/1/15" structure). The erbium concentration in the doped layer is estimated at 2 ppm based upon previous doping calibration confirmed with secondary ion mass spectrometry[64,65]. Figure 5.1a provides an illustration of the Er:TiO$_2$/SOI heterostructure.

In the crystal lattice, transitions within the unfilled $4f$ electronic orbital are weakly allowed and provide a direct C band telecom optical interface near 1533 nm. Slight differences in the observed $Y_1 \rightarrow Z_1$ crystal field transition in anatase TiO$_2$ have been reported for different growth conditions[136,116,65]. Here, we observe the lowest energy PLE signature near 1532.8 nm which we probe in this work. Rare earth ion optical transitions are long lived, making weak photon emission signals from single ions hard to isolate without additional engineering. In order to enhance the emission rate, optical cavities can be used to modify the excited state lifetime of rare–earth ions through the Purcell effect[152]. We therefore pattern waveguides and photonic crystal cavities into our SOI/TiO_2 heterostructure to enhance and collect the emission from ions in the thin film. We utilize a 1D photonic crystal cavity with elliptically shaped holes and a parabolic reduction of the lattice constant to confine the optical field to a mode volume of $\sim 0.4\ (\lambda/n)^3$, as introduced in Chapter 3.[64,104,101] Figure 5.1b shows an SEM image of a representative device fabricated for this study. The sample is placed in a closed–cycle cryostat at 3.4 K and the lensed optical fiber is aligned with 3–axis positioning stages.

5.2 Optical Emission and Lifetime Dynamics

In order to observe emission from single Er^{3+} ions, we tune the resonance of a cavity across the inhomogeneous optical transition by freezing a thin layer of nitrogen gas on the surface of the sample via a closely placed capillary tube[153]. Adsorption of the nitrogen leads to a redshift of the cavity mode which can be reversibly blueshifted through local heating of the cavity with resonant two photon absorption by the Si. Figure 5.2a shows the reflection spectrum for the cavity used in this work. The cavity exhibits a FWHM linewidth of 4.7 GHz and a quality factor of $4.14(7)\times10^4$.

We perform PLE measurements, shown in Figure 5.2b, by scanning a resonant laser within the cavity lineshape and observe discrete peaks in the emission recorded on a single photon detector (SNSPD), which we attribute to single Er^{3+} ions. In the inset we show the pulse sequence used for recording PLE signal. After an optical pulse of duration 1.0 μs, signal from the ions is collected within a programmable time window of duration τ_{coll}, which can be set independently from the repetition period of the pulse sequence, τ_{rep}. The sequence is repeated N times to build statistics. During the optical pulse we block the SNSPD with an acousto–optic modulator to prevent saturation of the detector signal.

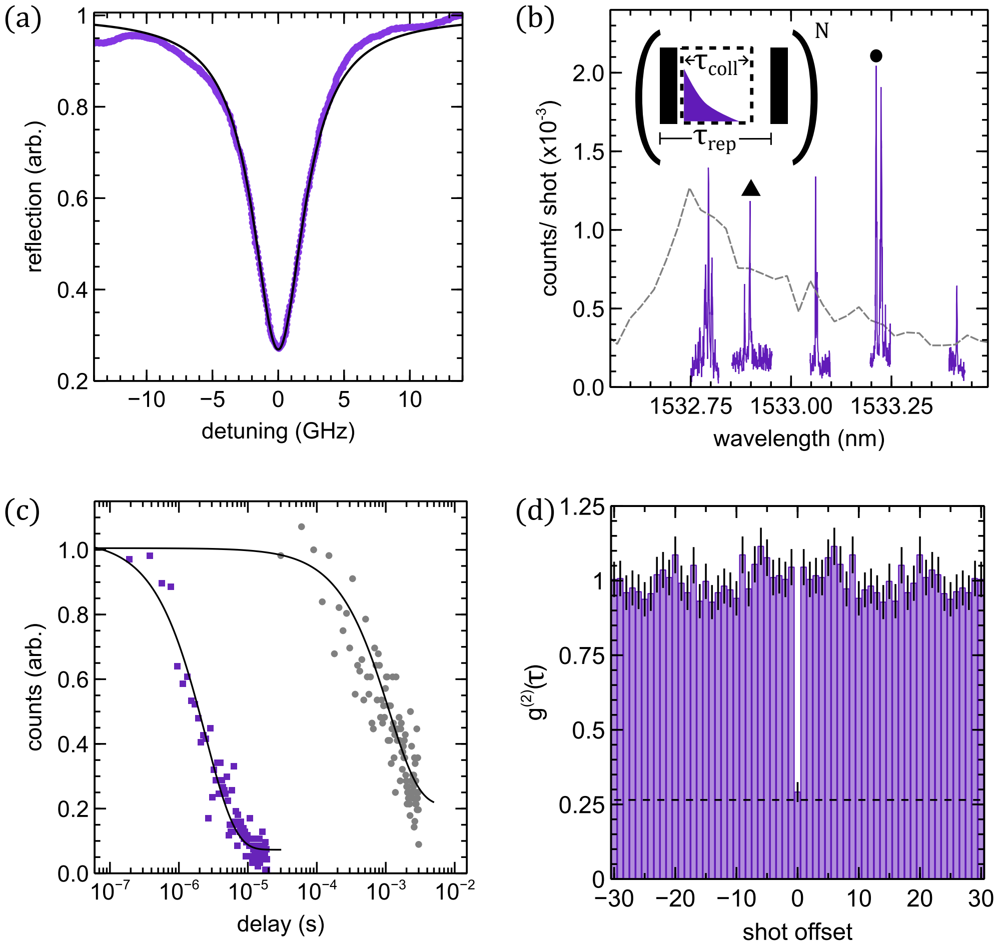

Figure 5.2: Purcell enhancement and antibunching of single photons. (a) The cavity reflection spectrum for the device used in this study. The black line is a Lorentzian fit to extract the cavity parameters. (b) PLE spectrum with resolved single ion emission lines that become visible when the cavity is tuned within the inhomogeneous line of the optical transition (gray dashed line, arbitrary scale). Inset: The optical pulse sequence used for PLE measurements. The duration of the signal collection window, τ_{coll}, is set independently from the repetition period of the pulse sequence, τ_{rep}. (c) The lifetime of the optical transition of a single ion resonant with the cavity (purple squares) is enhanced with respect to an ensemble in a waveguide with no cavity (gray circles). The single ion lifetime data is recorded for the ion marked with the triangle (▲) in panel b. (d) A single photon autocorrelation on the ion marked with the circle (●) in panel b, indicating single photon emission. The contribution of detector dark counts to the correlation is given by the dark shaded rectangles. The shot repetition period is 60 μs and the collection window is 20 μs.

The presence of the optical cavity on resonance with the ion induces a reduction in the optical lifetime due to the Purcell effect by a factor $P = \Gamma/\Gamma_0 - 1$, where $\Gamma = 1/T_1$ is the observed decay rate and Γ_0 is the decay rate without the cavity. In Figure 5.2c we show the observed lifetime of the ion near 1532.9 nm, marked with a triangle (▲) in Figure 5.2b. The observed lifetime is T_1 =2.43(13) μs, compared to 1.12(18) ms measured for an ensemble of ions in a waveguide with no cavity on the same chip. This enhancement corresponds to a Purcell factor of $P = 460(78)$.

5.3 Isolated Single Ion Emission Analysis

To confirm the emission of single photons from isolated Er^{3+} ions we perform a second order photon autocorrelation measurement, shown in Figure 5.2d for the ion near 1533.2 nm marked with a circle (●) in Figure 5.2b. We observe a zero delay value of $g^{(2)}(0) = 0.29(3)$, which indicates single photon emission for $g^{(2)}(0) < 0.5$. If we account for the background detection rate based on an independent measurement of the dark counts in our measurement (black dashed line), we observe an improved zero delay autocorrelation of $g^{(2)}(0) = 0.04$. In this measurement the shot repetition period is 60 μs, providing a delay out to 1.8 ms for the 30–shot offset shown in Figure 5.2d. The autocorrelation is symmetric about zero delay because the measurement is performed on a single detector.

5.4 Single Photon Linewidth Characterization

In Figure 5.3 we characterize the linewidth and spectral diffusion of a single Er^{3+} ion. We use the ion near 1533.2 nm again as a representative example. A single PLE scan reveals a Gaussian lineshape with a FWHM of $\Delta\nu = 173.6$ MHz, indicating the presence of spectral diffusion with a timescale $\lesssim$ minutes required to perform the scan. This is in agreement with previous ensemble–based transient spectral hole burning measurements showing a few

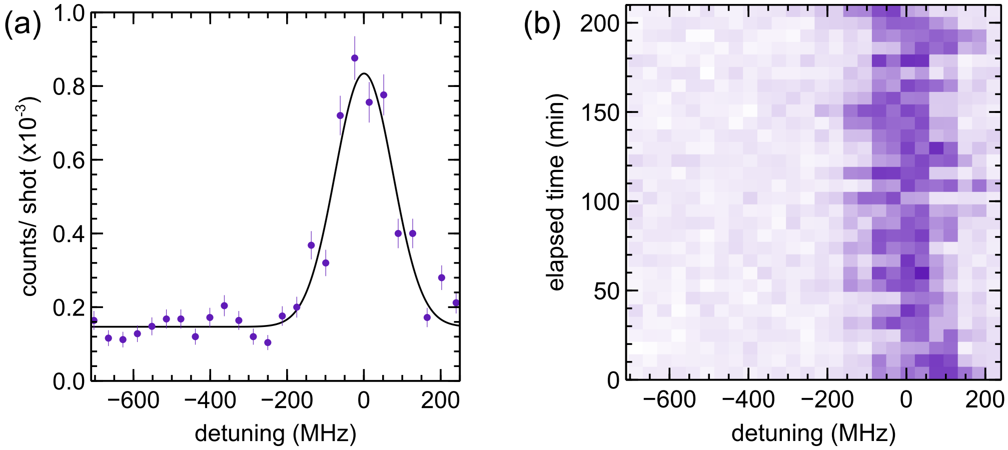

Figure 5.3: Single ion spectral diffusion. (a) A PLE scan across the single ion marked with a circle (●) in Figure 5.2b and fit with Gaussian lineshape. (b) Repeated PLE scans across the same ion over the course of $\sim$ 3.5 hrs.

hundred MHz spectral diffusion linewidths on $\sim$10 ppm Er-doped anatase thin films[100]. Over the course of $\sim$ 3.5 hours, the ion displays additional slower spectral wandering, and the time–averaged linewidth increases to $\Delta\nu = 209.4$ MHz. The Gaussian lineshape indicates that the observed linewidth is not limited by pure dephasing. One route toward reducing this linewidth closer to the radiative limit, such that $\Delta\nu = 1/(2\pi T_1)$, is to further tailor the thickness of the buffering layers in the TiO_2 film to reduce the ion's proximity to interfaces. It is also possible that grain boundaries in the polycrystalline film contribute to the observed linewidth, as has been observed in rare–earth doped nanocrystals[154,155]. Thus, a balance between grain size and smoothness of the thin film to maintain low optical losses in photonic devices is critical.

5.5 Concluding Remarks of This Chapter

To conclude, in this work we have demonstrated optical isolation of single Er^{3+} ions in CMOS compatible TiO_2 thin films monolithically integrated on an SOI photonics platform. Single ion linewidths have been observed on the order of $\sim$ 100 MHz with Purcell enhancement factors of the optical decay rate > 400 and clear antibunching of the single photon emission. This work shows the promise of monolithically integrated Er:TiO_2 on SOI for the development of widely scalable approaches to incorporate quantum emitters with mature semiconductor fabrication processes.

CHAPTER 6

EXPLORING DYNAMIC QUENCHING IN SINGLE-PHOTON AVALANCHE PHOTODETECTORS: A NOVEL PASSIVE QUENCHING METHOD WITH ADAPTIVE RESISTIVE SWITCHING

Semiconductor p–n junction-based single-photon avalanche diodes (SPADs) are a compact, efficient, and room-temperature-compatible technology, making them highly attractive for quantum communication[156,157] and advanced three-dimensional imaging applications[158]. Operating in Geiger mode, SPADs are reverse biased beyond their avalanche breakdown voltage[159], allowing them to detect single photons with high sensitivity. However, once an avalanche is triggered, it can become self-sustaining, necessitating a quenching circuit to terminate the multiplication process and reset the device. The most common quenching method involves a passive series resistor, but this approach inherently limits the recovery speed of the SPAD. The high resistance required for effective quenching results in slow recharging of the SPAD's depletion capacitor, restricting its frequency response and overall performance.[160]

In this chapter, we address this limitation by introducing an adaptive resistive switch (ARS) as a bias-dependent alternative to a fixed quenching resistor. The ARS leverages reversible metallic conduction, enabling dynamic switching between low and high resistance states under unipolar bias. By integrating ARS technology with commercially available SPADs, we achieve avalanche pulse widths as short as 30 ns, a 10× improvement over conventional passive quenching. This innovation significantly enhances the SPAD's frequency response, making it a promising approach for high-speed quantum and optical applications.

This chapter is mainly reproduced from Zheng et al.[103], with the permission of Springer Nature.

6.1 Introduction: Understanding Quenching Mechanisms in SPAD

6.1.1 Working Principles of the SPAD Passive Quenching

The principle of operation is described using the equivalent circuit of a conventional passively quenched SPAD (Fig. 6.1a). The circuit consists of a photon-activated switch, a diode resistance (R_d), a voltage source (V_b) representing the avalanche breakdown voltage of the SPAD, and a junction capacitance (C_d). The SPAD connects to an external voltage source, V_a ($V_a - V_b$ represents the overvoltage), with an R_L quenching resistor in series.

Initially, the SPAD is charged by the external voltage, resulting in a voltage $V_{\text{SPAD}} = V_a$ applied across C_d. Upon absorption of a photon (Fig. 6.1b), the switch closes, and C_d discharges through the internal loop, triggering an avalanche, which causes a drop in V_{SPAD}. When V_{SPAD} decreases to a value near V_b, the avalanche process ends, and the switch reopens (Fig. 6.1c). The external voltage now recharges the SPAD, completing the cycle and preparing the device for the next photon detection. The currents (I) and voltages (V_{SPAD}) during the discharging and recharging phases are given by the following equations:

$$I = \frac{(V_a - V_b)(1 - e^{-t/R_d C_d})}{R_L} \tag{6.1}$$

$$V_{\text{SPAD}} = (V_a - V_b)e^{-t/R_d C_d} + V_b \tag{6.2}$$

$$I = \frac{(V_a - V_b)e^{-t/R_L C_d}}{R_L} \tag{6.3}$$

$$V_{\text{SPAD}} = -(V_a - V_b)e^{-t/R_L C_d} + V_a \tag{6.4}$$

The diode resistance (R_d) is the sum of the resistances in the barrier region (the neutral

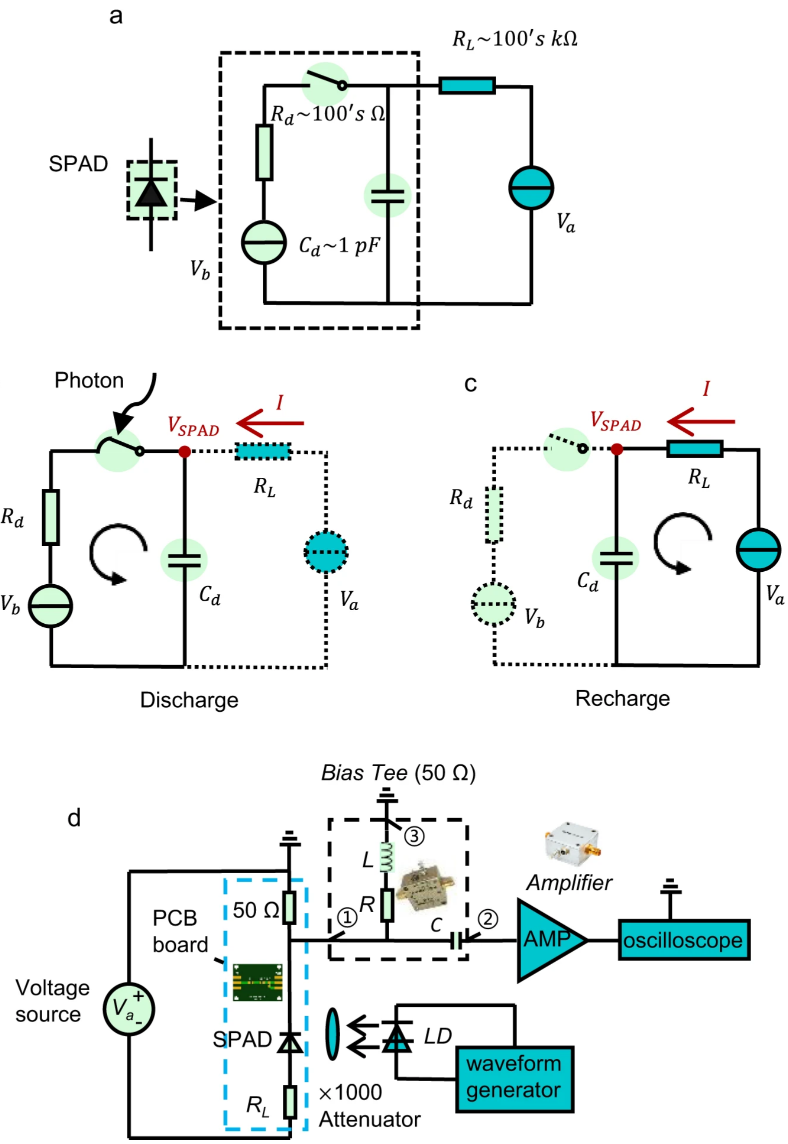

Figure 6.1: Schematic of the circuit model for SPAD. (a) Equivalent circuit model for passive quenching of the SPAD in series with a quenching resistor. The dashed box is the SPAD, represented by a capacitor, a resistor, a photon switch, and voltage source. (b) The SPAD discharge process when an avalanche is triggered by an incident photon. (c) Recharging process after quenching. (d) Single-photon detection system. Passive quenching is accomplished by connecting a SPAD and a resistor in series. A voltage source (Keithley 2400) is used to reverse bias the SPAD. The single-photon signal is generated by attenuating the optical signal from a laser diode driven by a Keysight 33600A waveform generator. The avalanche response current is determined from the voltage on a 50 Ω readout resistor and the voltage is introduced to an amplifier (Mini-circuits ZFL-1000LN+) and then into an oscilloscope (Rigol DS7024) through a bias tee (Mini-circuits ZFBT-4R2GW+).

region through which current flows) and the space-charge layer. A smaller sensing area and a thicker depletion region result in a larger diode resistance. Typical values for diode resistance range from $100\,\Omega$ to a few $\mathrm{k}\Omega$[159]. In this study, the SPAD under investigation has a large sensing area (diameter $200\,\mu$m) with a relatively thick barrier region, yielding a diode resistance of approximately $1\,k\Omega$. This configuration achieves a quantum efficiency of up to 85% at a wavelength of 650 nm.

6.1.2 How Adaptive Resistive Switch Effective in This System

In SPADs, a large quenching resistor (R_L) is crucial for ensuring effective avalanche quenching and minimizing jitter during the discharge process[159]. Consequently, R_L is typically set to around $100\,k\Omega$. However, as shown in Eq. (4), this high resistance significantly increases the recharging time due to the high $R_L C_d$ time constant. Given that R_d typically ranges from $100\,\Omega$ to a few $\mathrm{k}\Omega$, the discharge time (Eqs. (1) and (2)) is relatively short compared to the recharging duration. Since the probability of triggering an avalanche by newly absorbed photons remains low during the recharging phase, this extended recovery time ultimately limits the SPAD's frequency response when passive quenching is employed. To overcome this limitation, a more efficient quenching mechanism is needed that dynamically adapts its resistance, maintaining high resistance during discharge for effective quenching while enabling low resistance during recharging for faster recovery.

A promising solution is the adaptive resistive switch (ARS), a material whose resistance reversibly changes in response to the applied bias. The ARS is typically composed of dielectric metal oxides, such as HfO_2 and Al_2O_3, sandwiched between an inert electrode (commonly Pt) and an active electrode containing a diffusing metal species. Under an applied bias, metal ions from the active electrode migrate through the oxide layer, forming a conductive filament that dynamically modulates the device's resistance. When the bias is removed, the filament dissolves[161]. In this work, we utilize Al_2O_3 as the dielectric oxide layer and Ag as the active electrode, enabling controlled metal diffusion for adaptive resistance switching.

By integrating an ARS with a SPAD, significant improvements in single-photon detection response times can be achieved. At low bias, the ARS remains in its high-resistance state, ensuring rapid quenching of the avalanche. However, when the applied voltage exceeds a critical on-threshold, filamentary conducting paths form within the ARS material, drastically reducing its resistance and enabling efficient recharging. This resistance change is reversible, meaning that when the bias drops below a lower off-threshold voltage, the ARS returns to its high-resistance state. When placed in series with the SPAD, the ARS dynamically transitions between these states—high resistance during avalanche quenching and low resistance during recharging—thereby enhancing both quenching speed and recharging efficiency.

6.2 ARS Devices Fabrication and Measurement

6.2.1 ARS Fabrication Process

The ARS devices (see Figure 6.2) were fabricated on Si wafers covered with a 300 nm thermal SiO_2. The ARS structure is based on a 5 nm Al_2O_3 dielectric layer sandwiched by a Ti (5 nm)/Pt (50 nm) bottom electrode and an Ag (10 nm)/Au (50 nm) top electrode. The top and bottom electrodes (each 500 nm wide) are orthogonal, leading to a typical cross-bar device geometry[162].

The 500 nm-wide bottom electrode strips were first patterned via electron-beam lithography, followed by electron-beam evaporation of a Ti (5 nm)/Pt (50 nm) bilayer thin film and subsequent lift-off. Next, an AlO_x layer was deposited via atomic layer deposition (ALD, Veeco Fiji G2 PEALD system) at a substrate temperature of 250°C, using trimethylaluminium (TMA) and H_2O as precursors. The AlO_x layer was then patterned via photolithography and reactive ion etching (RIE).

Subsequently, the top electrodes, 500 nm wide and orthogonal to the bottom electrodes,

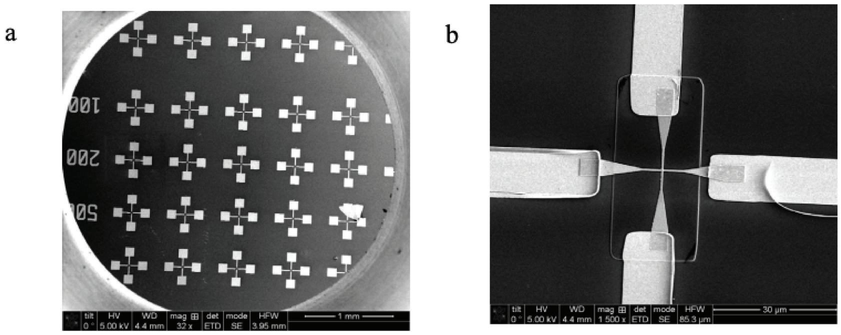

Figure 6.2: Electron microscope photographs of the ARS devices. (a) Low magnification image showing 25 independent devices on a wafer. (b) High magnification image showing the cross-bar architecture.

were deposited using electron-beam lithography, followed by electron-beam evaporation of Ag (10 nm)/Au (50 nm) and lift-off. The top electrode was deposited using a Lesker PVD-250 e-beam evaporator at a base pressure in the low 10^{-8} Torr range.

The device's active area (500 nm × 500 nm) corresponds to the cross-sectional overlap between the top and bottom electrodes. Finally, Ti (20 nm)/Au (200 nm) probe contacts (100 µm × 100 µm area) were patterned via photolithography and electron-beam evaporation.

6.2.2 Packaging and Electrical Characterization

The ARS device was encapsulated in a commercial TO-5 can, with its electrodes wire-bonded to the package pins. Given that the separation between package pins is on the order of several millimeters, the stray capacitance of the ARS package is considered negligible.

The quasi-static current–voltage (I–V) characteristics of the ARS, measured following the standard forming treatment at 5 V[163] (prior to the quenching experiments), are presented in Figure 6.3a. A compliance current of 1 mA is applied to limit the conducting filament thickness, ensuring the device operates in a volatile mode, where it reversibly returns to the high-resistance state when $V = 0$.[164,165]

The initial on-voltage is approximately 0.5 V, while the off-voltage is around 0.1 V. The off-state leakage current is measured to be less than 1 pA, which is below the detection threshold of the Keysight B1500A semiconductor analyzer and is effectively masked by its noise floor, as depicted in Figure 6.3a.

With continued operation, the on and off switching voltages exhibit a gradual upward drift, accompanied by an increase in leakage current. This phenomenon is evident in the I–V characteristics of Figure 6.3b, measured on the same time scale as Figure 6.3a, after approximately 10^{10} avalanche triggers under periodic single-photon signal operation. At this stage, the on and off switching voltages have increased to 8 V and 5 V, respectively. Correspondingly, the off-state and on-state resistances stabilize at approximately 400 $k\Omega$ and 40 $k\Omega$, as confirmed by simulation results, which will be discussed in the following sections. This final stabilized state will be utilized in the ARS-integrated SPAD quenching measurements and simulations.

The voltage drift and resistance variation observed over time suggest gradual device degradation, which is examined in detail in later sections. While this drift underscores the need for further material optimization, such behavior is not uncommon in the early stages of novel device development, and improvements in material engineering could mitigate these effects.

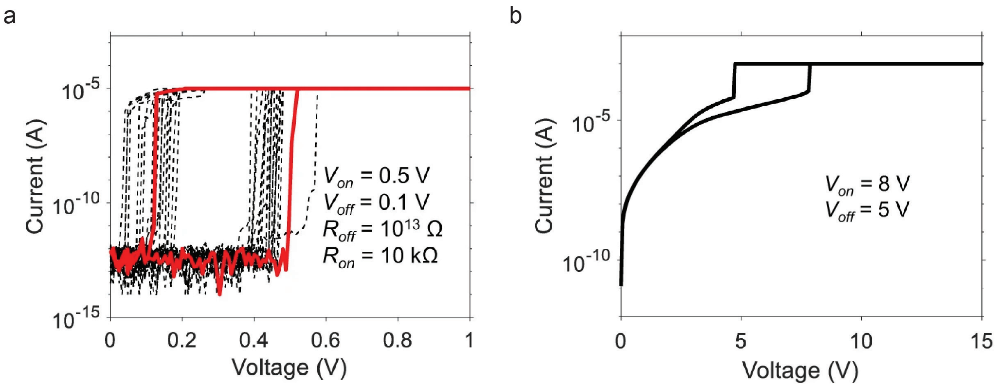

Figure 6.3: Current–voltage characteristics of the ARS showing the hysteresis behavior of the resistor, measured: (a) The initial few cycles of I-V measurements of as fabricated ARS devices. (b) After an estimated 10^{10} cycles of switching, the cycled I-V measurements of the ARS devices. The off-state and on-state resistances here are about 400 $k\Omega$ and 40 $k\Omega$.

6.3 Measurements of Avalanche Quenching Dynamics

6.3.1 Experimental Setup

The experimental setup for single-photon avalanche detection is shown in Figure 6.1d, where the Si SPAD (Hamamatsu S14643-02) is connected in series with a quenching resistor and powered by a DC voltage source (Keithley 2400). A bias tee (ZFBT-4R2GW+) is used to extract the AC signal from the SPAD output. The bias tee has three ports, i.e., DC+AC input port (port 1 in Figure 6.1d), AC output port (port 2), and DC output port (port 3). In the experiment, the SPAD, quenching resistor, 50 Ω readout resistor, and SMA type I/O port are soldered onto a PCB board. The 50 Ω readout resistor is used to match the PCB board impedance to the following circuits, and the bias tee was used to extract the avalanche pulse (port 2) from the DC background (port 3) and protect the amplifier and oscilloscope in case there is a constant and large current coming out from the PCB board (i.e., the SPAD is shorted).

The avalanche pulse is then introduced into a low noise amplifier (ZFL-1000LN+) and read out using an oscilloscope (Rigol DS7024). A 520 nm laser (Thorlabs L520P120) driven by a Keysight 33600A waveform generator delivers the light pulse to the SPAD. The Si SPAD's responsivity at 520 nm (0.2 A/W at a bias of 20 V with gain=1) enables calibration of the input light intensity using the photo-current read by the Keithley 2400. The laser drive voltage is carefully set so that the corresponding photon number in each pulse averages to 1000. The laser pulse is then attenuated to 1 photon/pulse by a ×1000 attenuator (Thorlabs NDUV530B). In this work, the current flowing through the SPAD is derived from the voltage readout (at the oscilloscope) divided by the voltage gain (10) of the low noise ZFL-1000LN+ amplifier times the AC port output impedance (50 Ω). The avalanche pulse shape studies were carried out with the laser repetition rate of 1 MHz and with the SPAD response recorded at a scanning step of 0.4 ns.

6.3.2 Characterization of SPAD Performance Integrated with ARS

When the ARS is used as a quenching resistor, the typical single-photon triggered avalanche pulse shape (representing the current flowing through the SPAD) is shown in Figure 6.4a as the blue curve. Four inflection points are marked as A, B, C, and D. The driving voltage of the laser is depicted as the red curve.

The pulse shape observed with ARS quenching differs significantly from that obtained using conventional passive quenching (i.e., a fixed resistor). In the current trace of Figure 6.4a, one possible interpretation is that the transition from A to B corresponds to the discharging process of the SPAD, while B to C and C to D represent subsequent recharging phases. If this interpretation holds, the quenching resistance during B to C must be higher than during C to D, as indicated by the lower slope of the B to C segment compared to C to D. This would suggest that the ARS transitioned to its low-resistance state near point C, which should have resulted in a noticeable increase in the SPAD current at C—an effect that is not observed in the experiment.

Therefore, discharging is completed before point A, meaning point A is part of the

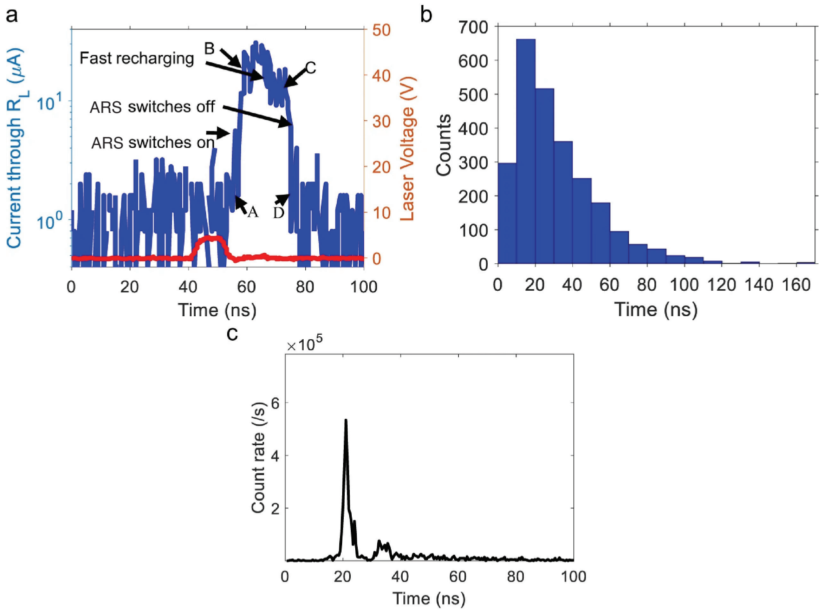

Figure 6.4: Quenching experiment results with ARS. (a) Typical pulse shape of the ARS quenched SPAD (blue curve); the red curve indicates the driving voltage of the laser. (b) The statistical distribution of the critical recovery time for the SPAD quenched by the ARS. The average critical recovery time is 30 ns. (c) Jitter performance of the ARS quenched SPAD when operated at 6 MHz repetition rate.

recharging process. The current rise at point A is due to the ARS switching resistance, as shown in Figure 6.3. This behavior aligns with expected timescales: the RC time constant for discharge is approximately 700 ps for a junction capacitance of 0.7 pF (from the device datasheet) and a diode resistance of 1 kΩ. As derived from Equations (1) and (2), about 90% of the stored energy discharges within 1.6 ns. In contrast, resistive switches typically switch within 100 ps to a few nanoseconds[166].

Given these timescales, it is likely that by point A, the SPAD has fully discharged, and the A to B transition results from the ARS switching from off (high resistance) to on (low resistance). The B to C segment represents the fast recharging phase with the ARS in its on state. At point C, when the voltage across the ARS drops below its off threshold, the ARS returns to its high-resistance state, leading to the C to D segment. Beyond point D, SPAD recovery continues, but the increased resistance of the ARS slows the process.

In this work, we define the A to D process as the critical recovery process, which is accelerated by the ARS. The period after D is the recovery tail, where the SPAD bias is gradually restored. While the recovery tail has a minor impact on detection efficiency, the critical recovery process determines the SPAD's counting speed. Since it is challenging to measure the ARS exact off-state resistance in a serial system during fast quenching and recharging, precise recovery determination is beyond the scope of this study.

A statistical analysis of 1000 avalanche pulses and their critical recovery time distribution is shown in Figure 6.4b. Most pulses exhibit a critical recovery time under 50 ns, with an average of 30 ns. Given the laser pulse width of 15 ns, and that single-photon pulses are generated using a 1000× attenuator applied to a laser pulse with an average of 1000 photons, occasional detection of multiple photons cannot be ruled out. However, this is not the focus of this study, which aims to demonstrate ARS-based dynamic quenching. Additionally, variations in pulse width in the SPAD output are likely due to the stochastic electrochemical reactions involved in ARS filament formation and dissolution.

The jitter performance of the ARS-quenched SPAD is determined from the avalanche output measured by an oscilloscope, as shown in Figure 6.4c. The counting threshold is set to 5 mV, with a sampling time step of 0.5 ns. A sharp peak appears at $t \approx 21$ ns with a full width at half maximum (FWHM) of 1.5 ns, indicating precise timing. A secondary peak is observed at $t \approx 35$ ns, which is attributed to ARS degradation, as discussed in[103].

In our measurements, the modulation bandwidth of the TO-packaged laser (Thorlabs L520P120) compresses the 15 ns pulse width of the drive waveform, as shown in Figure 6.4 (red curve). This bandwidth limitation causes the actual current waveform to be narrower than the electrical pulse, leading to a jitter time significantly shorter than the laser's 15 ns electrical input pulse width. The measured jitter indicates that most avalanche responses occur with high timing consistency, highlighting the fast and reliable switching of the ARS.

6.3.3 Comparison with Conventional Passive Quenching

We conducted quenching experiments on the same SPAD type, using fixed quenching resistors of 40, 60, 100, and 400 $k\Omega$ to compare with the ARS-based quenching results. The findings are presented in Figure 6.5a–d. It is important to note that when the fixed resistance is 30 $k\Omega$ or lower, unreliable quenching is observed, leading to unstable operation. Therefore, the conventional quenching experiments began at 40 $k\Omega$. Different excess bias voltages were applied to ensure a consistent counting rate at low repetition rates. The measured avalanche pulse response (Figure 6.5a) exhibits three distinct features: a spike, a plateau, and a recharging process.

The spike typically originates from the fast charging of the chip quenching resistor's stray capacitance.[167] However, this spike is absent in ARS quenching (Figure 6.4a). This occurs because the ARS is mounted on a TO-5 can package, where the lead pitch (5.08 mm) is significantly larger than the bottom termination distance of the chip resistor (0.3 mm) used in the conventional quenching method. Since stray capacitance is inversely proportional to the lead pitch, it becomes negligible in the ARS configuration.

The plateau appears due to a sustained avalanche, which occurs when the quenching resistance is not sufficiently large[168]. The variation in plateau duration results from the probabilistic nature of the quenching process[159]. When the quenching resistance is sufficiently large, the variation is minimized, and the quenching time is primarily determined by the RC time constant of the SPAD's internal discharge loop. However, when the quenching resistance is too low, the quenching resistor may fail to immediately terminate the avalanche, allowing it to persist until self-quenching occurs. This leads to significant randomness in quenching time[168]. Figure 6.5b–d compares the plateau time, recharging time, and recovery time for SPADs passively quenched with 40, 60, 100, and 400 kΩ resistors. As shown, in all cases, the recovery time is typically 300 ns or longer (Figure 6.5c) for a cumulative distribution function (CDF) of >0.75.

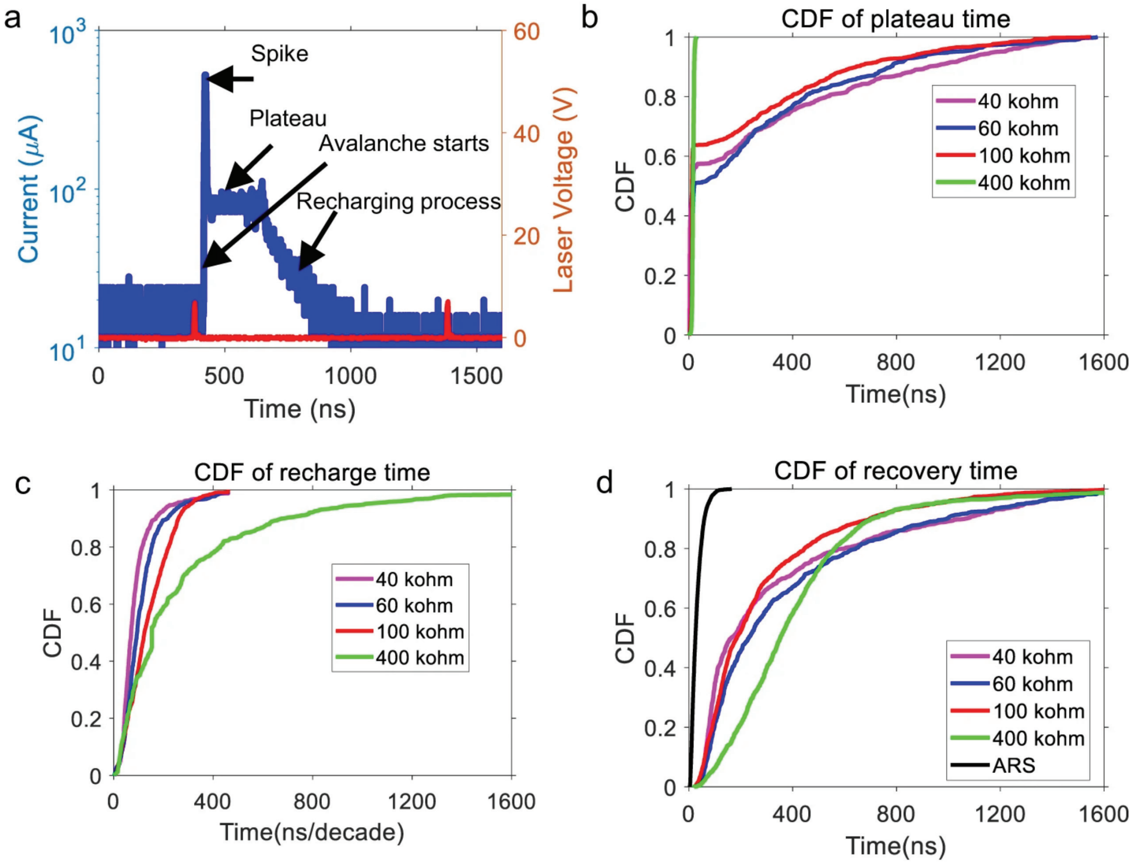

Figure 6.5: Conventional passive quenching results and comparison with ARS. (a) Typical response pulse shape of the 60 $k\Omega$ quenched SPAD (blue curve) indicating features corresponding to the spike, plateau, and recharging processes (pulse shape for the 40, 100, and 400 $k\Omega$ quenched SPAD has similar features); the red curve indicates the driving voltage of the laser. (b), (c) Cumulative distribution functions (CDFs) of the plateau and recharge times, respectively, for the 40, 60, 100, 400 $k\Omega$ quenched SPAD. (d) CDFs of the total recovery times for the 40, 60, 100, 400 $k\Omega$, and the critical recovery time of the ARS quenched SPAD (black).

In contrast, ARS-based quenching achieves a 10× reduction in response time, reaching 30 ns. Our passive resistance data indicates that such an improvement is not possible with a fixed resistance alone, as reducing the fixed resistance to such low values prevents effective avalanche quenching. This suggests that the dynamic switching behavior of the ARS is crucial in achieving lower quenching resistance, leading to significantly faster recovery times.

The advantages of faster critical recovery times is illustrated in high repetition rate (20 MHz) single-photon measurements (Fig. 6.6a and b). Representative avalanche responses (across 1.6 μs time windows) are shown both for the ARS and conventional passive quenching (100 $k\Omega$) cases. The red curve indicates the single-photon drive voltage, and the blue curve is the SPAD signal. Statistical analysis of the data was carried out using single-photon response data over 0.4 ms with a time step resolution of 0.4 ns. There are 8000 single-photon pulses involved in the analysis. The single-photon counting rate under 20 MHz single-photon repetition rate is 1.8 MHz for conventional passive quenching (100 $k\Omega$) and 8.5 MHz for ARS quenching.

Similarly, the counting rates under different repetition rates ranging from 1 to 50 MHz are calculated and plotted in Fig. 4c for SPADs quenched by ARS and conventional passive quenching. For comparison, 400 $k\Omega$ (R_{off} of ARS), 40 $k\Omega$ (R_{on} of ARS), and 100 $k\Omega$ are used to perform the conventional passive quenching. As is shown in Figure 6.6c, the counting rate of the ARS quenched SPAD is significantly higher than the passive quenched SPAD, especially when the repetition rate is large. The results are consistent with the faster critical recovery times of the SPAD measurements with ARS quenching.

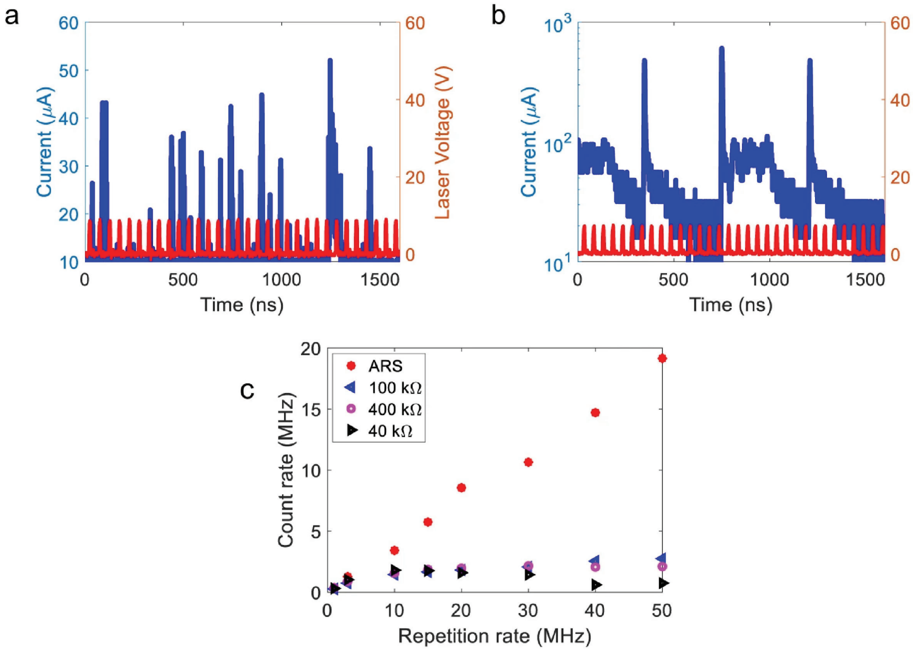

Figure 6.6: The count rate comparison at a input repetition rate of 20MHz. (a-b) Avalanche response to a single photon signal with a 20 MHz repetition rate for a SPAD quenched by (a) ARS and (b) the 100 $k\Omega$. (c) Counting rate under different repetition rate for SPAD quenched by ARS and fixed resistor.

6.4 Simulation and Analysis of ARS-Based Quenching Mechanisms in SPADs

The narrow avalanche pulse width and fast quenching performance indicate a critical resistance transition in the ARS during SPAD quenching. To further investigate this improvement, we conducted a theoretical analysis by modeling and simulating the ARS-quenched SPAD circuit using PSPICE simulations in OrCAD PSpice Designer.

6.4.1 The Circuit Design for Simulation

The circuit schematic is shown in Figure 6.7. The photon signal port, resistances R1, R2, and the switches S_{Trig}, S_{Self} represent the switch in Figure 6.1a–c. V1 and R3 correspond to the equivalent internal voltage source (breakdown voltage) and the SPAD internal resistance, respectively. C1 represents the SPAD junction capacitance. Together, the optical switch sub-circuit, V1, R3, and C1 form the equivalent circuit of the SPAD.

The quenching resistance is modeled by R4, which represents the ARS with the PSPICE model embedded. V2 serves as the external voltage source, while R5 is a 50 Ω matching resistor. The components C4, R6, and L1 form a bias tee, which separates the AC and DC signals. The values of R6 are taken from the datasheet of the bias tee ZFBT-4R2GW+, where capacitance and inductance values are not provided. Therefore, C6 and L1 are chosen from the datasheet of another bias tee product BT1-0026 from Marki Microwave, which has a similar transmission band to what was used in the experiment.

The AC signal is introduced from C4 into an oscilloscope, whose input impedance is 50 Ω (R7). In the simulation, we track the current flow through R7, the voltage across the SPAD, and the voltage and current on the ARS during quenching. The photon signal port generates a voltage pulse with a pulse width of 1 ps, whose rising edge triggers the switching (closure) of a voltage-controlled switch $\mathrm{S}_{\mathrm{Trig}}$. When $\mathrm{S}_{\mathrm{Trig}}$ switches on (i.e., closes), C1 discharges through an internal loop of

$$C1 \rightarrow R3 \rightarrow V1 \rightarrow S_{\mathrm{Trig}} \rightarrow S_{\mathrm{Self}} \rightarrow C1$$

which is marked in blue in the figure.

The discharge current exceeds the threshold of the current-controlled switch $\mathrm{S}_{\mathrm{Self}}$, causing it to close at the start of the discharge. The falling edge of the electric pulse leads to the reopening of the voltage-controlled switch $\mathrm{S}_{\mathrm{Trig}}$.

The current-controlled switch threshold is set at 100 μA (latching current of a self-sustained avalanche[159]) in this work. When discharging ends, the current flow through $\mathrm{S}_{\mathrm{Self}}$ is given by:

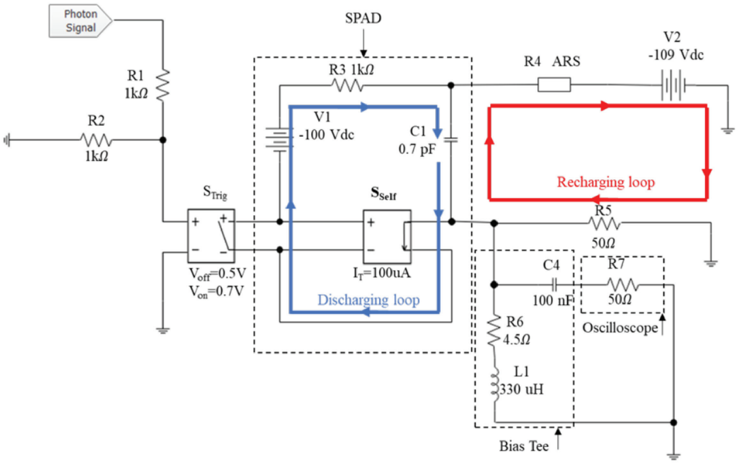

Figure 6.7: Schematic circuit diagram for Pspice simulation. The photon signal port, R1, R2, S_{Trig}, S_{Self} are used to mimic the optical switch in Figure 6.1. V1 and R3 are the equivalent internal voltage source (breakdown voltage) and SPAD's internal resistance, respectively. C1 is the SPAD junction capacitance. The equivalent optical switch, V1, R3 and C1 form the equivalent circuit of SPAD. R4 denotes the quenching resistance of ARS. V2 is the external voltage source. R5 is the 50 Ω impedance matching resistor. C4, R6, and L1 form a Bias Tee, which separates the AC signal and the DC signal. The AC signal is introduced from C4 into an oscilloscope (R7), of which the input impedance is 50 Ω. The discharging path (blue) and recharging path (red) are labelled. The current flowing through R7, the voltage across SPAD (C1), and the voltage and current on ARS are monitored in simulation.

$$I = \frac{V_{\text{excess}}}{R_{\text{total}}}$$

Where: V_{excess} is the excess bias (difference between the external voltage and breakdown voltage), and R_{total} is the sum of the quenching resistance and the diode resistance.

The SPAD breakdown voltage V_1 is 100 V, and the junction capacitance C1 is 0.7 pF (Hamamatsu S14643 datasheet). A typical value of 1 kΩ[169] is used for the internal resistance. With $V_2 = 109$ V, the excess bias is 9 V. The recharging path is labeled in Figure 6.7 as a red loop through:

$$V_1 \rightarrow R_5 \rightarrow C_1 \rightarrow \text{ARS} \rightarrow V_1$$

6.4.2 Model of ARS

Since the ARS is not a standard electronic component commonly used in traditional CMOS circuit design, its modeling is not standardized, and its performance heavily depends on the chosen model. In this work, we simulate the ARS using an established bipolar memristive system with threshold[170]. The behavior of the ARS is described by the following equations:

$$I = x^{-1}V_M \tag{6.5}$$

$$\frac{dx}{dt} = f(V_M)W(x, V_M) \tag{6.6}$$

$$f(V_M) = \beta \times \left[V_M - \frac{1}{2}(V_{\text{on}} + V_{\text{off}}) - \frac{1}{2}(|V_M - V_{\text{off}}| - |V_M - V_{\text{on}}|)\right] \tag{6.7}$$

$$W(x, V_M) = \theta(V_{\text{on}} - V_M)\theta\left(1 - \frac{x}{R_{\text{off}}}\right) + \theta(V_M - V_{\text{off}})\theta\left(\frac{x}{R_{\text{on}}} - 1\right) \tag{6.8}$$

Here, I and V_M are the current and voltage on the ARS, x is the resistance of the ARS, and β denotes a resistance transition speed (with units of $\Omega/(\text{s}\cdot\text{V})$). $V_{\text{on}}, R_{\text{on}}, V_{\text{off}}$, and R_{off} represent the switch-on voltage, on-state resistance, switch-off voltage, and off-state resistance, respectively. Extracting the key parameters of the ARS from Figure 6.3b, we obtain:

$$V_{\text{on}} = 8V, \quad V_{\text{off}} = 5V, \quad R_{\text{on}} = 40\text{k}\Omega, \quad R_{\text{off}} = 400\text{k}\Omega.$$

The response varies as a function of β, and it is found that the switching speed is greatly influenced by this factor. In this study, β is assumed to be $1 \times 10^{14}\Omega/(\text{s}\cdot\text{V})$ to accommodate the nanosecond-level rising and falling speed of the response curve.

Additionally, θ is the smoothed step function, which is introduced to prevent convergence issues[170]. Here we use:

$$\theta(x) = \frac{1}{1 + e^{-x/b}} \tag{6.9}$$

$$|x| = x\left[\theta(x) - \theta(-x)\right]. \tag{6.10}$$

Here, b is a smoothing parameter and we choose it to be 10^{-5}.

6.4.3 Simulation Results and Analysis

With the circuit and ARS PSpice model ready, the simulation results are shown in Figure 6.8a and b. In Fig. 6.8a, the response current is shown in a solid blue curve, while the excess bias, which is defined as the voltage across the SPAD minus the breakdown voltage, is shown in a dashed red curve. The shape of the blue current curve is similar to that observed in the experiment. The SPAD abrupt voltage drop illustrates how the discharge proceeds (1–4 ns). After the discharge, the ARS starts switching and generates an avalanche pulse output with the transition $A \rightarrow B \rightarrow C \rightarrow D$, similar to the experimental results shown in Figure 6.4. Figure 6.8b shows the voltage across the ARS (purple curve) and the ARS resistance (dark curve). Using relevant physical parameters described above, the simulations show that with the triggering of an avalanche, the junction capacitor of the SPAD discharges, and the ARS switches from high (400 $k\Omega$) to low (40 $k\Omega$) resistive states in 4.7 ns ($A \rightarrow B$).

It should be noted that point A (Fig. 6.4a) occurs during the discharging period (1–4 ns), after the voltage across the ARS exceeds 8 V. As a result of switching-on, the current increases, and the recharging process accelerates ($B \rightarrow C$ in Fig. 6.8d, e). During the fast recharging, the excess voltage across the SPAD increases to 4 V (red dashed curve in Fig. 6.8a), and the voltage on the ARS reduces to below 5 V (purple curve in Fig. 6.8b). As a result, the ARS switches off ($C \rightarrow D$ in Fig. 6.8b). The recharging process then decelerates ($C \rightarrow D$ in Fig. 6.8a).

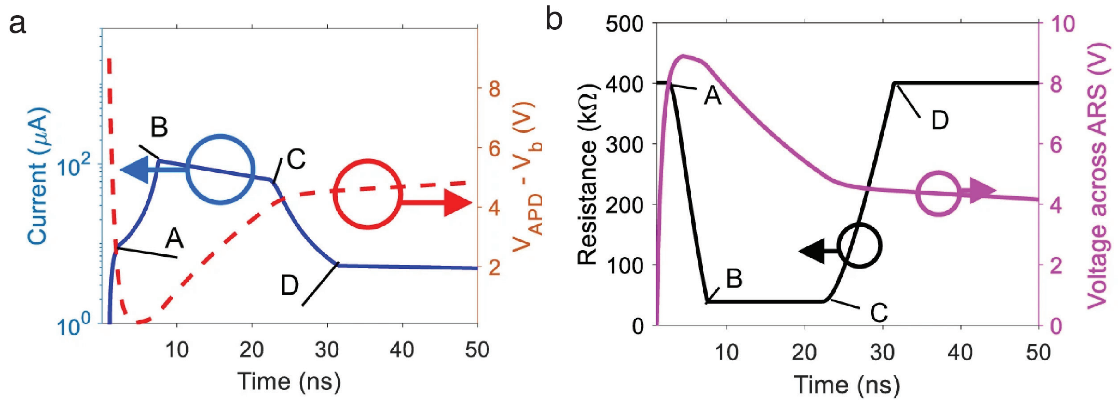

Figure 6.8: Pspice simulations of a SPAD quenched by the ARS showing the variation of the following parameters as a function of time. (a) The avalanche current trace (blue curve) and the voltage across the SPAD (red dashed curve). (b) voltage across the ARS (pink curve) and the resistance (dark curve).

The shape of the simulated SPAD response is consistent with experimental observations, indicating that the ARS transitions from high to low resistance during the SPAD discharge and recharge process, thereby significantly reducing SPAD reset times. However, two issues remain unresolved in the model used. First, the magnitude of the current in the simulation peaks at 100 μA, which is higher than the observed range (10–40 μA). The reason for this is not yet clear at this moment. Second, our model does not incorporate statistical fluctuations of the avalanche pulse width.

6.5 Concluding Remarks of This Chapter

In summary, we have proposed and experimentally demonstrated an avalanche photodetector quenched with a self-adaptive resistive switch (ARS). Our results show that this approach achieves an avalanche pulse width at least eight times narrower than the conventional passive quenching method, while maintaining the simplicity of the traditional approach. Both experimental data and simulations support our conclusion that this fast switching behavior arises from the voltage-dependent resistance of the ARS.

This work has significant potential for enhancing the performance of silicon photomultipliers (SiPMs) by accelerating avalanche quenching recovery times. Additionally, the ARS is easy to fabricate, fully compatible with silicon-based material systems, and offers strong integration potential with SPAD arrays, making it a promising candidate for next-generation high-speed photon detection applications.

CHAPTER 7

DESIGNING MECHANICALLY ROBUST AND POROUS ALL-INORGANIC ANTIREFLECTIVE COATINGS USING MICROPOROUS POLYMERS

In this chapter, we demonstrate the research using polymer of intrinsic microporosity 1 (PIM-1) to design single-layer and multilayered all-inorganic Antireflective coatings (ARCs) with excellent mechanical properties. Using PIM-1 as a template in sequential infiltration synthesis (SIS), we can fabricate highly uniform, mechanically stable conformal coatings of AlO_x with porosities of about 50% and a refractive index of 1.41 compared to 1.76 for nonporous AlO_x that is perfectly suited for substrates commonly used in high-end optical systems or touch screens (e.g., sapphire, conductive glass, bendable glass, etc.). We show that such films can be used as a single-layer ARC capable of reduction of the Fresnel reflections of sapphire to as low as 0.1% at 500 nm being deposited only on one side of the substrate. We also demonstrate that deposition of the second layer with higher porosity using block copolymers (BCP) enables the design of graded-index double-layered coatings. AlO_x structures with just two layers and a total thickness of less than 200 nm are capable of reduction of Fresnel reflections under normal illumination to below 0.5% in a broad spectral range with 0.1% reflection at 700 nm. Additionally, and most importantly, we show that highly porous single-layer and graded-index double-layered ARCs are characterized by high hardness and scratch resistivity. The hardness and the maximum reached load were 7.5 GPa and 13 mN with a scratch depth of about 130 nm, respectively, that is very promising for the structures consisting of two porous AlO_x layers with 50% and 85% porosities, correspondingly.

This chapter is mainly reproduced from Ji et al.[104], with the permission of ACS Publications.

7.1 Introduction: Antireflective Coatings

Antireflective coatings (ARCs) are widely used to reduce the light reflection at interfaces, and thereby enhance the transmittance of light.[171,172] ARCs with low refractive indices are important for a broad range of applications such as solar cells, displays (mobile phones, computer and television screens), telescope lenses, cameras, and eyeglasses. The optical components in such devices are often made out of different types of glass with varying refractive indices, n, (e.g., fused glass (n = 1.458), sapphire glass (n = 1.768), Gorilla glass (n = 1.50), indium tin oxide (ITO) glass (n = 1.827) at 630 nm). According to the Fresnel equation,[173] to minimize the reflectance of glass substrates in the visible range of the light spectrum, a single-layer ARC with n about 1.2 to 1.4 is required. The optimal thickness of the ARC for a given wavelength λ is at normal incidence for destructive interference, which leads to minimal reflectance over the spectral range around λ.

Bulk inorganic materials with n less than 1.4 are limited and mainly restricted to fluorides. For example, MgF_2[174] with n about 1.38 in the visible range can lower the reflectance of each side of the float glass from 4.3% to 1%. However, MgF_2 thin film deposition involves the use of hydrofluoric acid or other aggressive precursors of fluorine.[175,176] Additionally, MgF_2 is soluble in water (about 0.013 g/100 mL) and exposure to inorganic fluorides can be associated with health concerns.[177] These factors reasonably impose some constraints on the applicability of fluorides in the fabrication of touchable devices and optical systems exposed to the environment. To achieve safe, nontoxic and stable coatings with lower refractive indexes, nanoporous thin films have been introduced for the fabrication of ARCs.[111,178] According to effective medium theory, the refractive index of the thin composite film is determined by the fractions of different materials as long as the feature sizes are much smaller than the wavelength of the incident light.[179] In the case of dry porous films, their refractive indices will be determined by the refractive index of the inorganic material and air with the refractive index of 1. The higher porosity will be associated with the smaller refractive index. Therefore, proper control over the porosity is the key to nanoporous ARCs with the desired antireflectivity.

Compared to the single-layered ARCs, multilayered ARCs consisting of several alternating layers with different thicknesses and refractive indices can provide a better antireflection performance by minimizing the light reflection in a broad spectral range as a result of the destructive interference of wavefronts reflected at each interface. In turn, a gradual decrease of the refractive index (graded-index ARCs) allows for avoiding a sharp transition between interfacing optical media resulting in minimal Fresnel reflection losses.[180] The novel techniques, including nanoporous thin film via polymer with porosities[111] and lithography-produced nanostructure coatings,[181] have been researched for high-quality graded-index ARCs. However, porosity can compromise the mechanical properties of materials resulting in increased brittleness, lower hardness and scratch resistance. Moreover, due to the high optical contrast between scratched and unscratched areas originated from differences in the refractive index, the ARCs are subject to high scratch visibility. It is equally important for optical coatings to have adequate mechanical properties in terms of hardness and abrasion resistance in order to withstand day-to-day handling.[182] Therefore, it is critical to develop approaches that can finely tune the refractive index and thickness of the nanoporous inorganic coatings used to design graded-index multilayer ARCs, while preserving the low cost and suitability for large-scale manufacturing of advanced thin films with good resistance to mechanical wear.

7.2 Fabrication of Porous Coatings: Utilizing Polymer Templates for ALD Deposition

7.2.1 Materials

Substrates in the experiments were silicon, sapphire, and Gorilla glass. The silicon substrates with 300 nm thermal oxide were purchased from Silicon Valley Microelectronics, Inc. The half-inch sapphire glass windows were purchased from Meller Optics. Gorilla glass was purchased from Abrisa Technologies. The polymer of intrinsic microporosity such as PIM-1 was synthesized in DMAc at 160 °C following the previously reported procedure.[183] Dimethylacetamide (DMAc, Sigma-Aldrich) and anhydrous potassium carbonate (K_2CO_3, Sigma-Aldrich) were used as received. 5,5,6,6-Tetrahydroxy-3,3,3,3-tetramethylspirobisindane (TTSBI, Sigma-Aldrich) was purified by crystallization from methanol. Tetrafluoroterephthalonitrile (TFTPN, Sigma-Aldrich) was purified by vacuum sublimation at 150 °C under an inert atmosphere. The block copolymer poly(styrene-block-4-vinylpyridine) (PS-P4VP) (specifically in this study (PS(79)-PVP(36.5)) was purchased from Polymer Source, Inc.

7.2.2 Polymer Film Deposition

The dry PIM-1 powder was dissolved in anhydrous chloroform with a concentration of 20 mg/mL. The dry PS(79)-PVP(36.5) powder was dissolved in toluene to obtain 13 mg/mL. After dissolution, the polymer solutions were filtered through a polytetrafluoroethylene (PTFE) 0.45 μm pore size filter and spin-coated onto the clean substrate at 2000 and 4000 rpm for PIM-1 and PS(79)-PVP(36.5), respectively. The cleaning process of the substrates was the following: sonication in DI water (2 min), followed by sonication in acetone (2 min) and in isopropyl alcohol (2 min).

7.2.3 Solution Treatment of the Deposited Polymer

For PIM thin films, the substrates with the deposited coatings were immersed in methanol heated to 55 °C for about 1 h and then kept at room temperature overnight in a fume hood. For BCP thin films, the samples were immersed in ethanol heated to 75 °C for 2 h. After completion, the samples were dried under nitrogen gas flow and used for infiltration with inorganic precursors from the vapor phase immediately.

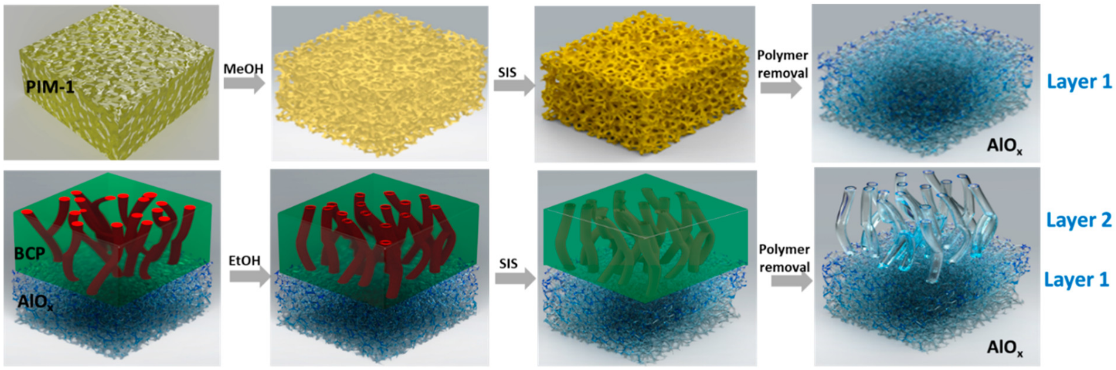

Figure 7.1: Depiction of the steps involved in the fabrication of single-layer and double-layered AlO_x ARCs. PIM-1 serves as a template for the synthesis of the porous AlO_x (Layer 1). More porous structures can be deposited on the top of Layer 1 using BCP as a template (Layer 2) for the formation of more porous double-layered structures.

7.2.4 Infiltration of the Polymer Templates with Alumina Precursors to Form ARCs

The infiltration of polymer templates with alumina precursors was performed using a SIS method that has been described earlier.[111] A GEMStar thermal atomic layer deposition (ALD) system was used for the process for convenience, though we note that our process is not an ALD process (deposition rates are much higher and the deposition is not atomic layer-by-layer) and could be carried out in other appropriately configured chemical vapor deposition systems as well. TMA and H_2O were used as gas-phase precursors. In the first half of a SIS cycle (about 400s), the TMA vapors (0.08 s pulse length through the ALD actuator) infiltrate into the polymer template, selectively binding to the functional groups. (13) The selectively bound precursors then react with water vapor (0.08 s pulse length through the ALD actuator) locally producing AlO_x in the next half of the synthesis cycle (about 120 s). At the end of each SIS cycle, the unreacted gases are purged out of the chamber with 200 sccm N2 gas flow for 20 s. The procedure was repeated 10 times. The infiltration was performed at 90 °C.

The single-layer alumina ARCs (further referred as AlO_x^{PIM}) were prepared following the procedures described above. The graded-index double-layered alumina ARCs, further referred as $\mathrm{AlO}_x^{PIM/BCP}$, were prepared via spin-coating of a solution of PS(79)-PVP(36.5) on the top of the porous AlO_x^{PIM} film, with the BCP layer prepared same as above. For double-layered ARCs, 10 cycles of SIS were exerted both on the PIM and the BCP templates to obtain Layer 1 and Layer 2, respectively. Hexamethyldisilazane (HMDS) treatment was performed using YES-3/5TA. The process parameters were 150 °C, pressure 1 Torr, and 3 cycles of N2 and HMDS purging for 5 min.

After SIS, the samples were annealed at 500 °C for 1 to 3 h to remove the polymer template under airflow in the quartz tube in a Thermolyne 21100 Tube Furnace.

The overall fabrication process of the single-layer and double-layered $\mathrm{AlO_x}$ ARCs are depicted in Figure 7.1.

7.3 Characterization of Porous Coating Thin Films

7.3.1 Refractive Index of the Infiltrated Thin Films

A Horiba Jobin Yvon UVISEL spectroscopic ellipsometer was used to measure the film thickness, porosity, and refractive index of the nanoporous thin films. Measurements on approximately five samples show that Layer 1 (AlO_x^{PIM}), formed via 10 SIS cycles, has a porosity of about 50%, resulting in a refractive index of approximately 1.41 over the 300 – 1000 nm spectral range (see Fig. 7.2). This refractive index is ideal for minimizing reflectance on high-index substrates such as sapphire (n = 1.768) or ITO glass (n = 1.827). In contrast, ellipsometry estimates indicate that Layer 2 (AlO_x^{BCP}) has a porosity of around 85%, which yields a lower refractive index of about 1.1 (see Fig. 7.2).

Furthermore, the typical thicknesses of Layer 1 (AlO_x^{PIM}) and Layer 2 (AlO_x^{BCP}) are approximately 80 nm and 105 nm, respectively. These thicknesses can be tuned by adjusting the spin-coated polymer template. According to the quarter-wavelength optimization theory

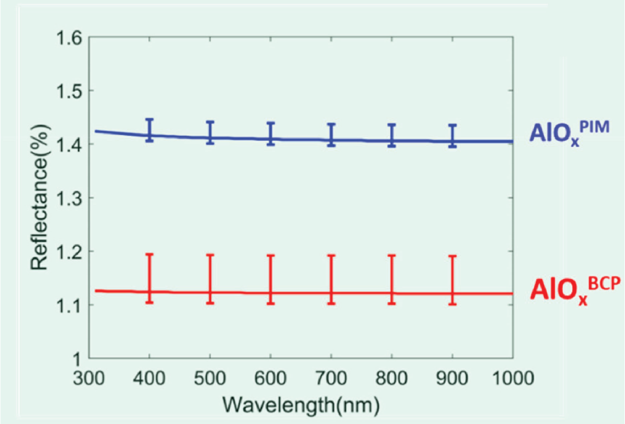

Figure 7.2: The refractive indices of AlO_x^{PIM} and AlO_x^{BCP} versus different wavelengths. The data is measured using ellipsometry. The nanoporous AlOx films are obtained via infiltration of PIM-1 (AlO_x^{PIM}) and PS(79)-PVP(36.5) (AlO_x^{PIM}) followed by polymer removal via annealing as described in the fabrication details.

for ARCs, these layer thicknesses are designed to enable destructive interference for visible wavelengths on glass substrates such as Gorilla glass (n = 1.5) and sapphire glass (n = 1.768). Together, these results demonstrate that multilayer graded-index ARC coatings can be precisely engineered to achieve optimal optical performances.

7.3.2 Electron Microscopy and X-Ray Characterization

Scanning Electron Microscopy (SEM) and Small-Angle X-ray Scattering (SAXS) are used to analyze the nanostructure and morphology of the infiltration thin films after anneal.

For Layer 1 (AlO_x^{PIM}), the SEM data indicates that the obtained alumina films (deposited on silicon) are smooth (Fig. 7.3a). SAXS data show that AlOx obtained using the PIM-1 template has a mesoscale poorly ordered structure (Figure 7.3e). A very broad peak at the higher Q region suggests the presence of spherical features of about 10 nm with a rather broad size distribution in the AlOx layer that agrees with the SEM data (Fig. 7.3a). During the spin-coating process, the PIM-1 layer may trap air between the polymer and the substrate. Upon thermal annealing, polymer removal leads to slight deflation of these air-trapped regions, forming dark circular features in the SEM images of AlO_x^{PIM} (Fig.

7.3d).

In contrast, the SEM data of Layer 2 (AlO$_x^{BCP}$) indicated that alumina coatings obtained using PS-P4VP templates consisted of rather tangled porous tubular micelles (Fig. 7.3). To visualize the interface between AlO$_x^{PIM}$ and AlO$_x^{BCP}$ in AlO$_x^{PIM/BCP}$, we prepared the sample shown in Figure 7.3d in which we mechanically removed the fragment of PS(79)-PVP(36.5) film spin-coated on the top of AlO$_x^{PIM}$ before SIS. Analysis of delaminated fragments of the AlO$_x^{PIM}$ films by SEM points to an uniform nature of the porous coating. Importantly, such features do not affect the deposition of the consecutive layers (Fig. 7.3d).

SAXS data indicates that being deposited on porous AlO$_x^{PIM}$ (Layer 1), AlO$_x^{BCP}$ (Layer 2) has a smaller domain spacing as compared to that deposed directly on the Si substrate. The SAXS pattern from of AlO$_x^{BCP}$ grown directly on Si and the position of the diffraction peak from its microphase separated cylindrical structure, q = 0.0089 A–1 corresponding to d-spacing of 70.5 nm (Figure 7.3e), are similar to those of neat PS-PVP. On the other hand, the SAXS peak from the AlO$_x^{PIM/BCP}$ appears at a much higher q, suggesting that the degree of microphase separation of the BCP is suppressed on PIM. However, the SAXS pattern of the AlO$_x^{PIM/BCP}$ also shows a diminished peak at the same position as AlO$_x^{BCP}$ at q = 0.0089 A–1. Therefore, we conclude that the structures of both samples are not much different from each other at their top surfaces as seen from SEM images (Fig. 7.3b,c), where the morphologies are affected more by the polymer/air interaction than the polymer/substrate interaction.

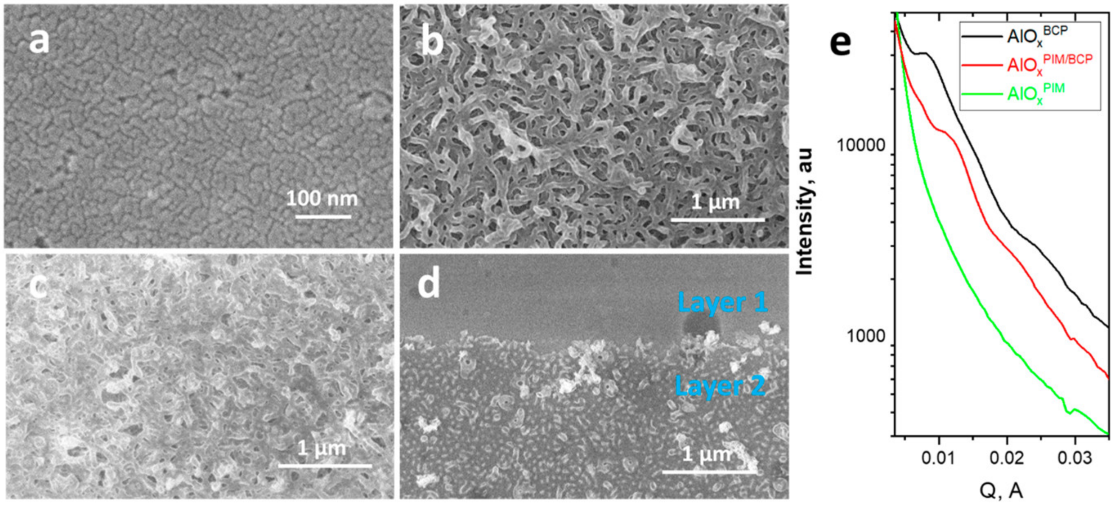

Figure 7.3: SEM and SAXS measurements results. (a-b) SEM images of single 80 and 105 nm thin $\mathrm{AlO_x}$ layers formed as a result of 10 SIS cycles on PIM-1 (AlO_x^{PIM}, Layer 1, shown in panel (a)) and (AlO_x^{BCP}, Layer 2, shown in panel(b)). (c) SEM image of the double-layered AlOx ARC ($\mathrm{AlO}_x^{PIM/BCP}$). (d) Top view SEM image showing the interface between $\mathrm{AlO_x}$ layers with different porosities in double-layered $\mathrm{AlO_x}$ ARC (bottom and top layers were about 80 and 105 nm, respectively). (e) SAXS data obtained for $\mathrm{AlO_x}$ layers shown in panels (a–c).

7.4 Antireflective Properties of Single-Layer and Graded-Index Double-Layer ARC Coatings

This section presents the optical performance of single-layered and graded-index double-layered ARCs. To assess their effectiveness, the ARC coatings were applied to sapphire glass and Gorilla Glass, enabling a direct comparison of their anti-reflectivity and transparency improvements.

Sapphire glass is an extremely durable, scratch-resistant, and optically transparent material composed of crystalline aluminum oxide ($\mathrm{Al_2O_3}$). With a high hardness (Mohs scale around 9), exceptional chemical stability, and superior optical clarity, it is widely used in luxury watches, aerospace optics, and consumer electronics.[184]

Similarly, Gorilla Glass, developed by Corning Inc., is a chemically strengthened glass known for its durability, scratch resistance, and optical clarity. It is extensively used in smartphones, tablets, laptops, and other electronic displays.[185]

By demonstrating ARC performance on these two widely used glass substrates, we aim to highlight the broad applicability of our coatings for various industrial and commercial products.

7.4.1 Optical Performance on Sapphire Glass

The refractive index of 1.41 characteristic to a porous alumina single layer with 50% porosity obtained with PIM-1 template (Fig. 7.2) is well suited to minimize the reflectance of high refractive index substrates such as sapphire (n = 1.768) or ITO glass (n = 1.827). Indeed, Figure 7.4 demonstrates that the reflectance of sapphire can be lowered from about 7.9% to 0.1% at 500 nm due to the porous alumina coating on only one side of sapphire while the transmittance increased from 85% to about 90 - 91% in the spectral range between 380 and 650 nm (Fig. 7.4a-b).

In double-layered ARC coating the thicknesses of Layer 1 and Layer 2 were 80 and 105 nm, respectively. According to the quarter wavelength optimized thickness theory for ARC, these layers should enable destructive interference for the wavelengths in the visible range. Two layers of porous alumina resulted in the design of the graded-index ARC for a sapphire substrate that lowered its reflectance from 7.9% to below 0.5% in a broad spectral range (Fig. 7.4a). Moreover, the reflectance of sapphire was lowered to 0.1% at around 700 nm. The light transmission of sapphire was increased from about 85% to 91 – 93% just as a result of deposited ARC on one side of the sapphire. Note that such a significant reduction of the reflectance and increase in the transparency of the sapphire was realized by deposition of only two gradient-index layers with a total thickness smaller than 200 nm. Photographs of the uncoated and coated sapphire glass are shown in Figure 7.4c-d to visualize the performance of the single-layer and graded-index double-layered $\mathrm{AlO}_x^{PIM/BCP}$ and to highlight the better transparency and less reflection of the sapphire coated with porous ARCs.

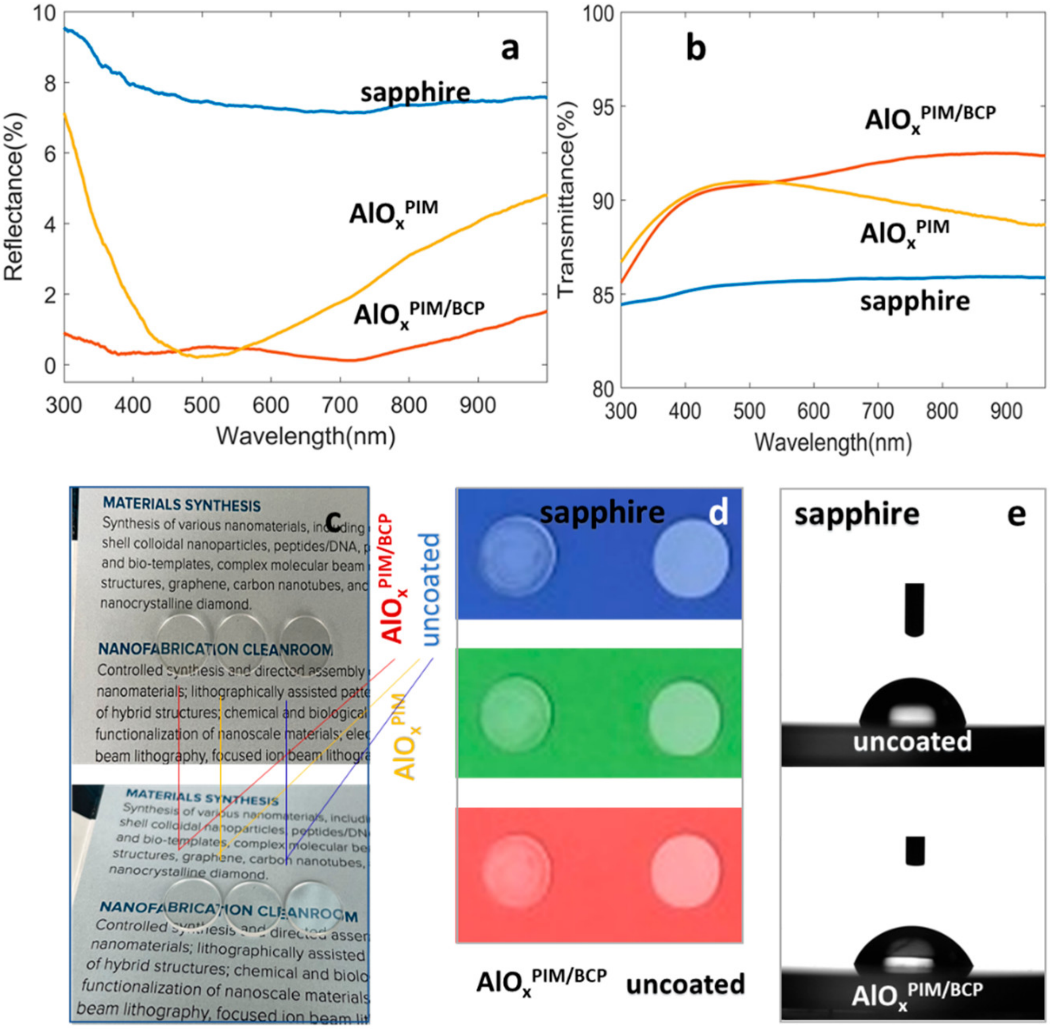

Figure 7.4: Optical performance of single (AlO_x^{PIM}) and graded-index double-layered ($AlO_x^{PIM/BCP}$) ARCs deposited on sapphire glass: the reflectance (a) and the transmittance (b) data; (c-d) The optical micrographs visualizing the performance of the porous ARCs. The images were taken at normal incidence and at an of 45° angle (top and bottom, respectively). Images shown in panel (d) were taken at an of 45° angle to the substrate. (e) Contact angle measurements on sapphire and sapphire coated with graded-index double-layered ($AlO_x^{PIM/BCP}$) after hexamethyldisilazane (HMDS) treatment.

7.4.2 Optical Performance on Gorilla Glass

The double-layered ARC worked well also for the Gorilla glass (n = 1.50). With only just two layers of porous $\mathrm{AlO_x}$, we observed in our double-layered structure ($\mathrm{AlO}_x^{PIM/BCP}$) a significant reduction of the reflectance at normal incidence from 4% to below 0.8% over the visible range (Fig. 7.5a). The transmittance was improved from 92% to above 95% in the visible range with just a single side coating (Fig. 7.5b). Figure 7.5c shows the optical image of Gorilla glass coated with graded-index double-layered ARC, demonstrating the transparency of the coated sample and elimination of the light reflection at the substrate coated with double-layered $\mathrm{AlO}_x^{PIM/BCP}$ ARC. One can see no reflection of the light at the coated substrate, while surrounding uncoated Gorilla glass samples demonstrate the pronounced reflection (Figure 7.5c, bottom image).

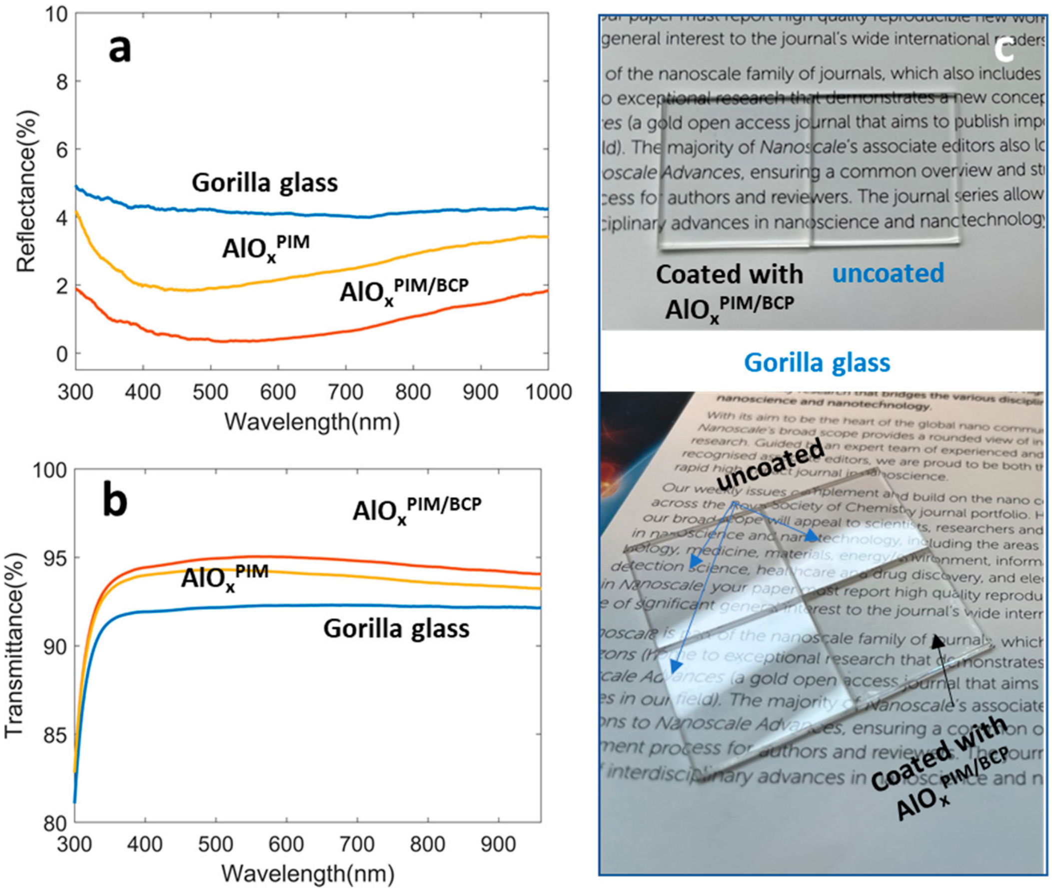

Figure 7.5: Optical performance of single (AlO$_x^{PIM}$) and graded-index double-layered (AlO$_x^{PIM/BCP}$) ARCs deposited on Gorilla glass: the reflectance (a) and the transmittance (b) data; (c) Optical images of Gorilla glass sample with graded-index double-layered (AlO$_x^{PIM/BCP}$) ARCs obtained at normal incidence (top image) and at about 30° angle (bottom image). The bottom images shows the elimination of the reflection at the coated substrate while the reflection of the fluorescent light tube is pronounced at the surrounding uncoated substrates.

7.5 Mechanical Stability of Single-Layer and Graded-Index Double-Layer ARC Coatings

Mechanical properties of the ARC coatings need to be appropriate for protection against scratches and abrasion during their use. We measured the hardness and scratch resistance of our films, parameters commonly used to characterize the mechanical performance of the optical coatings. While we were mostly interested in the mechanical properties of graded-index double-layered porous films on sapphire, we also studied such structures deposited on Si.

7.5.1 Methods - Nanoindenter

The mechanical properties of the thin films were characterized by a KLA iNano nanoindenter. The fused silica reference material was tested for instrument verification. The hardness tests were performed with the Berkovich tip. The scratch tests were performed with a conical tip with a radius of 5 μm by continuously increasing the load on the film as the indenter moved along the surface of the substrate with a velocity of 20 μm/s. The ramp-load started at 0.04 mN and ended upon reaching a load necessary to cause some identifiable film failure (critical load) or until reaching 20 mN if the film did not deform. All scratch tests were run using the same parameters to compare the critical load values from different samples more accurately. The critical load was automatically determined by the instrument using acoustic emission feedback picked by a piezoelectric detector arranged next to the indenter. A critical load was defined as the load value at which the acoustic emission suddenly increased. Depth profiles of the scratch vectors were also recorded and analyzed.

7.5.2 Thin Film Hardness

Our hardness and scratch test results (Fig. 7.6) indicate that despite the porous nature our PIM-templated and PIM/BCP double-layered coatings have excellent mechanical properties and are superior to the BCP-only coatings. Figure 7.6a shows the plots of the hardness versus the nanoindentation depth. The hardness of graded-index double-layered ARC structures ($\mathrm{AlO}_x^{PIM/BCP}$) on sapphire at a nanoindentation of 150 nm can be as high as 7.5 GPa (Fig. 7.6b), which is, in fact, higher than the hardness of, for example, bulk fused silica glass (about 6 GPa).[186] Conducting the hardness measurements on $\mathrm{AlO_x}$ deposited on different substrates, we observed the effect of the substrate on the hardness that is expected for thin films.[187] Interestingly, at smaller loads $\mathrm{AlO_x}$ deposited on sapphire shows a higher tendency toward its deformation, as evidenced by lower hardness than coatings deposited on the Si (Figure 7.6b). Since sapphire has a higher hardness than Si, the effect of the substrate only should result in the opposite trend. However, at higher loadings the hardness values of both coatings start to be similar for graded-index double-layered porous coatings deposited on sapphire and Si substrates and therefore we propose that this observation can be associated with the position of sharp Berkovich-type indenter with respect to the pores in the top layer and orientation of the pores. In general, in order to minimize the effect of the substrate, it is recommended to analyze samples in which the deformation takes place only in the top 10 – 20% of the volume.[187] This is, however, an unreasonable condition for our structures that have a thickness below 200 nm, dictated by the optical needs of the application.

7.5.3 Thin Film Scratch Resistivity

Figure 7.6c shows the scratch load during the scratching tests. In such tests the critical load can be used as a measure to compare the scratch resistivity of different coatings if the experimental parameters are kept constant. The maximum load is detected by the instrument using acoustic emission feedback picked by a piezoelectric detector arranged

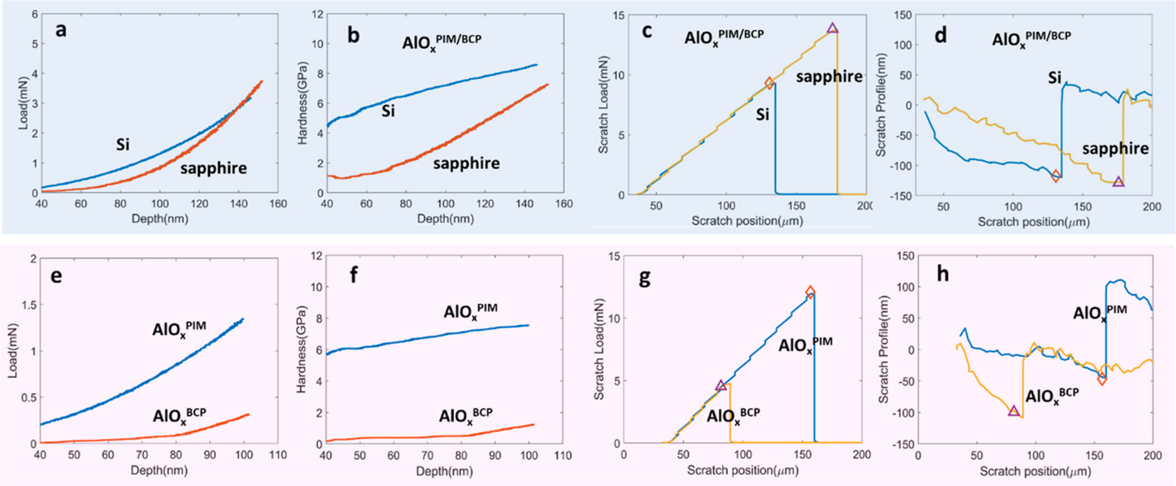

Figure 7.6: Mechanical properties of the graded-index double-layered 185 nm ARCs structures (AlO$_x^{PIM/BCP}$) deposited on different substrates (Si and sapphire) (a–d): (a) the exerted load vs nanoindentation depth and (b) the thin film hardness vs nanoindentation depth. (c) The scratch load vs the scratch position during the nano scratch test. The critical markers show the point when the pinhead is lifted off the surface. (d) The vertical scratch profile vs the scratch position during the nano scratch test shown in panel c. The comparison of the mechanical properties of AlO$_x^{PIM}$ (Layer 1 in double-layered ARC) and AlO$_x^{BCP}$ (Layer 2 in double-layered ARC) on Si (e–h): (e) The exerted load vs nanoindentation depth. (f) The thin film hardness vs nanoindentation depth. (g) The scratch load vs the scratch position during the nano scratch test. The critical markers show the point when the pinhead is lifted off the surface. (h) The vertical scratch profile vs the scratch position during the nano scratch test, shown in panel g. The comparison shows that the AlO$_x^{PIM}$ layer has much higher hardness and scratch resistance as compared to AlO$_x^{BCP}$.

next to the indenter. The maximum reached load was 13 mN with a scratch depth of about 130 nm (Figure 7.6d), which is much higher than that of the porous anodic aluminum oxide (AAO) ARC structures in which the indenter can penetrate down to 350 nm at 2 mN load [188]. The scratch tests indicated higher scratch resistivity of coatings deposited on the sapphire substrate as compared to coatings on Si (Figure 7.6c,d) that is reasonable since sapphire and the graded-index double-layered coating have a similar chemical composition that can result in their better adhesion of the coatings to the substrate.

7.5.4 Discussion of Results

Our results indicate that the films containing PIM (whether single layer or double-layered) are significantly harder (Figures 7.6a,e). The advanced mechanical properties of graded-index ARC are most likely due to the underlying AlO_x^{PIM} (Layer 1) formed via infiltration of PIM-1 (Figure 7.6f). The hardness of AlO_x^{PIM} is much higher than that of AlO_x^{BCP} and comparable to the hardness of the double-layered ARCs on Si (Figure 7.6b). The scratch test data demonstrate the same trend (Figure 7.6c). Therefore, Layer 1 fabricated via SIS in PIM not only served as the first antireflection layer with a higher refractive index as expected but also performed as a mechanical supporting layer for the porous film above it. The higher hardness and scratch resistance of the AlO_x^{PIM} films as compared to AlO_x^{BCP} films can be attributed to their lower porosity and smaller size of the pores.

7.6 Concluding Remarks of This Chapter

In conclusion, PIM-1 serves as a highly effective template for the robust deposition of uniform, porous $\mathrm{AlO_x}$ conformal films via SIS. The resulting 50% porosity and refractive index of 1.41 make these films well-suited for high-refractive-index substrates such as sapphire and other optical components. Furthermore, these layers can be integrated into more complex multilayer architectures to enhance optical performance.

We also demonstrate that incorporating a second, higher-porosity layer using block copolymers enables the fabrication of graded-index double-layered coatings, effectively reducing Fresnel reflections to below 0.5% across a broad spectral range, with reflections as low as 0.1% at 700 nm. This is achieved using nontoxic, stable $\mathrm{AlO_x}$ structures with just two layers and a total thickness of under 200 nm.

Importantly, the mechanical durability of these graded-index coatings is enhanced by the mechanically robust AlO_x^{PIM} layer, which results from PIM-1 infiltration with a metal oxide precursor. The coatings exhibit a maximum load capacity of 13 mN with a scratch depth of 130 nm, making them highly promising for applications requiring both optical efficiency and mechanical resilience.

This study highlights the potential of PIM-1-based templating for the cost-effective and scalable fabrication of high-performance optical coatings with exceptional optical and mechanical properties, paving the way for future advancements in anti-reflective coatings and functional nanostructured films.

CHAPTER 8

CONCLUSION OF THIS JOURNEY

8.1 Summary of Key Findings

This thesis explored the integration of erbium (Er) ions with silicon photonics for quantum memory applications, with a focus on device fabrication, material engineering, optical characterization, and system performance evaluation. The research spanned from quantum memory development (**Chapters 2–5**) to broader photonics applications (**Chapters 6–7**), demonstrating both fundamental advancements and technological innovations.

In **Chapter 2**, we demonstrated the material deposition method ALD for Er:TiO_2, which is compatible with CMOS integration for quantum applications. **Chapter 3** focuses on the design, simulation, and fabrication of photonic chips, particularly photonic cavities, to enhance atom-photon interactions and achieve Purcell enhancement of the emission rate. Building upon these foundations, **Chapter 4** presents the successful integration of Er-doped materials into photonic structures, where we experimentally probe the Purcell effect and explore the rich cavity QED physics by varying the input laser power. To further establish the potential of Er-ion-based quantum memory, **Chapter 5** demonstrates the isolation of single erbium ions via optical measurements, marking a crucial step toward individual qubit readout in a quantum memory system. Overall, this research advances Er-ion-based quantum memory, pushing the frontier of CMOS-compatible integration while demonstrating its strong potential as a quantum repeater processor for future industrial-scale quantum technologies.

Furthermore, classical photonics research also drives the technological innovation. In **Chapter 6**, we introduce a novel ARS-based dynamic quenching method, which achieves a 10× improvement over traditional passive quenching techniques. This advancement holds great potential for future integration into SPAD chips, significantly enhancing their performance. In **Chapter 7**, we explore nanoporous coatings for display technologies, demonstrating a fabrication technique for ultra-thin films (about 200 nm) that exhibit remarkable anti-reflectivity and mechanical durability. This research was successfully filed as a U.S. patent and presents a promising avenue for next-generation screen technologies.

This thesis contributes to the development of quantum photonic memory, bridging fundamental research in materials and nanophotonics with technological innovations in photon detection and optical coatings. By advancing erbium-based quantum memory, this work lays the foundation for scalable, fiber-network-compatible quantum information systems. Furthermore, the demonstrated ARS-based SPAD technology and graded-index ARCs open new possibilities in communication, sensing, and high-performance optics.

8.2 Future Research Outlook

While this thesis successfully demonstrated key milestones in Er-ion integration with photonic devices, several challenges still remain to solve towards a real quantum memory system. Here, I propose a few points that may be worth to investigate in the future.

I. Enhancing Single-Ion Control and Coherence. The current optical coherence (about 170 MHz) is not yet sufficient for direct quantum memory applications. To address this limitation, further optimization is required, potentially involving advancements in materials engineering, optical system design, and cryogenic system refinement. How do material defects influence spectral diffusion and optical linewidth broadening? How can fabrication processes be optimized to minimize defects and improve coherence? How can the system be refined to reduce environmental fluctuations and enhance stability? Addressing these questions is crucial for advancing single-ion control and achieving the coherence necessary for practical quantum memory applications.

II. Remote Entanglement with Erbium Quantum Memories. Achieving remote entanglement is a critical milestone for demonstrating a functional quantum memory or repeater system, essential for quantum network applications. To reach this goal, not only are indistinguishable photons required, but communication efficiency also plays a key role in ensuring the success of such experiments. In this research, our primary focus is on optimizing communication efficiency. Moving forward, deeper exploration of spin-photon interactions within the cavity-ion coupling system will be necessary. Additionally, further investigations into controlling photon properties, such as detuning, will be crucial for enhancing the performance and scalability of erbium-based quantum networks.

III. Chip-Scale Integration with Electronic Components. While this research primarily focuses on integrating Er-doped materials with silicon photonics, achieving a fully functional quantum memory system will require further integration with electronic components. Key elements such as electro-optic modulators, photodetectors, and control circuits will play a critical role in enabling practical implementation. This level of integration extends beyond material processing and demands a comprehensive approach that combines materials science with systematic electronic and photonic engineering expertise. Developing such a hybrid system will be essential for realizing scalable and efficient quantum memory systems.

IV. Expanding Beyond Erbium. The primary advantage of erbium lies in its natural optical transitions within the telecom C-band, making it highly suitable for photonic quantum memory applications. However, as a Kramers ion, its electron spin coherence is inherently limited. To achieve longer coherence times, alternative qubit systems, such as nuclear spins or non-Kramers ion electron spins, may be necessary. Therefore, a key challenge remains: how can Er ions be efficiently coupled to these long-coherence candidates? While this issue is yet to be resolved, leveraging Er as the central spin-photon interface for quantum memory systems holds great promise. Such an approach could drive significant advancements in the field and open the door to new quantum memory technologies.

V. Integration with Hybrid Quantum Systems. Erbium is a strong candidate for quantum memory in quantum networks. However, for broader applications in quantum computing, integrating it with hybrid quantum systems remains both promising and challenging. While some studies have explored Er-diamond systems and Er-based quantum transduction, their efficiency and fidelity still require significant improvement for practical implementation. Advancing novel design strategies and integration techniques will be key to overcoming these limitations, potentially unlocking new capabilities for Er-based quantum technologies and expanding their role in next-generation quantum applications.

REFERENCES

[1] He-Liang Huang, Dachao Wu, Daojin Fan, and Xiaobo Zhu. Superconducting quantum computing: a review. *Science China Information Sciences*, 63(8):180501, 2020. doi:10.1007/s11432-020-2881-9. URL `https://doi.org/10.1007/s11432-020-2881-9`.

[2] Peiying Zhang, Ning Chen, Shigen Shen, Shui Yu, Sheng Wu, and Neeraj Kumar. Future quantum communications and networking: A review and vision. *IEEE Wireless Communications*, 31(1):141–148, 2024. doi:10.1109/MWC.012.2200295.

[3] Jasminder S. Sidhu, Siddarth K. Joshi, Mustafa Gündoğan, Thomas Brougham, David Lowndes, Luca Mazzarella, Markus Krutzik, Sonali Mohapatra, Daniele Dequal, Giuseppe Vallone, Paolo Villoresi, Alexander Ling, Thomas Jennewein, Makan Mohageg, John G. Rarity, Ivette Fuentes, Stefano Pirandola, and Daniel K. L. Oi. Advances in space quantum communications. *IET Quantum Communication*, 2(4): 182–217, 2021. doi:https://doi.org/10.1049/qtc2.12015. URL `https://ietresearch.onlinelibrary.wiley.com/doi/abs/10.1049/qtc2.12015`.

[4] Stefano Pirandola. End-to-end capacities of a quantum communication network. *Communications Physics*, 2(1):51, 2019. doi:10.1038/s42005-019-0147-3. URL `https://doi.org/10.1038/s42005-019-0147-3`.

[5] C. L. Degen, F. Reinhard, and P. Cappellaro. Quantum sensing. *Rev. Mod. Phys.*, 89: 035002, Jul 2017. doi:10.1103/RevModPhys.89.035002. URL `https://link.aps.org/doi/10.1103/RevModPhys.89.035002`.

[6] Yudong Cao, Jonathan Romero, Jonathan P. Olson, Matthias Degroote, Peter D. Johnson, Mária Kieferová, Ian D. Kivlichan, Tim Menke, Borja Peropadre, Nicolas P. D. Sawaya, Sukin Sim, Libor Veis, and Alán Aspuru-Guzik. Quantum chemistry in the age of quantum computing. *Chemical Reviews*, 119(19):10856–10915, 2019. doi:10.1021/acs.chemrev.8b00803. URL `https://doi.org/10.1021/acs.chemrev.8b00803`. PMID: 31469277.

[7] Daniel J. Bernstein and Tanja Lange. Post-quantum cryptography. *Nature*, 549(7671): 188–194, 2017. doi:10.1038/nature23461. URL `https://doi.org/10.1038/nature23461`.

[8] Raihan Ur Rasool, Hafiz Farooq Ahmad, Wajid Rafique, Adnan Qayyum, Junaid Qadir, and Zahid Anwar. Quantum computing for healthcare: A review. *Future Internet*, 15(3), 2023. ISSN 1999-5903. doi:10.3390/fi15030094. URL `https://www.mdpi.com/1999-5903/15/3/94`.

[9] Román Orús, Samuel Mugel, and Enrique Lizaso. Quantum computing for finance: Overview and prospects. *Reviews in Physics*, 4:100028, 2019. ISSN 2405-4283. doi:https://doi.org/10.1016/j.revip.2019.100028. URL `https://www.sciencedirect.com/science/article/pii/S2405428318300571`.

[10] Yu-Ao Chen, Qiang Zhang, Teng-Yun Chen, Wen-Qi Cai, Sheng-Kai Liao, Jun Zhang, Kai Chen, Juan Yin, Ji-Gang Ren, Zhu Chen, Sheng-Long Han, Qing Yu, Ken Liang, Fei Zhou, Xiao Yuan, Mei-Sheng Zhao, Tian-Yin Wang, Xiao Jiang, Liang Zhang, Wei-Yue Liu, Yang Li, Qi Shen, Yuan Cao, Chao-Yang Lu, Rong Shu, Jian-Yu Wang, Li Li, Nai-Le Liu, Feihu Xu, Xiang-Bin Wang, Cheng-Zhi Peng, and Jian-Wei Pan. An integrated space-to-ground quantum communication network over 4,600 kilometres. *Nature*, 589(7841):214–219, 2021. doi:10.1038/s41586-020-03093-8. URL `https://doi.org/10.1038/s41586-020-03093-8`.

[11] M. K. Bhaskar, R. Riedinger, B. Machielse, D. S. Levonian, C. T. Nguyen, E. N. Knall, H. Park, D. Englund, M. Lončar, D. D. Sukachev, and M. D. Lukin. Experimental demonstration of memory-enhanced quantum communication. *Nature*, 580(7801):60–64, 2020. doi:10.1038/s41586-020-2103-5. URL `https://doi.org/10.1038/s41586-020-2103-5`.

[12] Mouzhe Xie, Xiaofei Yu, Lila V. H. Rodgers, Daohong Xu, Ignacio Chi-Durán, Adrien Toros, Niels Quack, Nathalie P. de Leon, and Peter C. Maurer. Biocompatible surface functionalization architecture for a diamond quantum sensor. *Proceedings of the National Academy of Sciences*, 119(8):e2114186119, 2022. doi:10.1073/pnas.2114186119. URL `https://www.pnas.org/doi/abs/10.1073/pnas.2114186119`.

[13] Jacob S. Feder, Benjamin S. Soloway, Shreya Verma, Zhi Z. Geng, Shihao Wang, Bethel Kifle, Emmeline G. Riendeau, Yeghishe Tsaturyan, Leah R. Weiss, Mouzhe Xie, Jun Huang, Aaron Esser-Kahn, Laura Gagliardi, David D. Awschalom, and Peter C. Maurer. A fluorescent-protein spin qubit, 2024. URL `https://arxiv.org/abs/2411.16835`.

[14] David D. Awschalom, Hannes Bernien, Rex Brown, Aashish Clerk, Eric Chitambar, Alan Dibos, Jennifer Dionne, Mark Eriksson, Bill Fefferman, Greg David Fuchs, Jay Gambetta, Elizabeth Goldschmidt, Supratik Guha, F. Joseph Heremans, Kent David Irwin, Ania Bleszynski Jayich, Liang Jiang, Jonathan Karsch, Mark Kasevich, Shimon Kolkowitz, Paul G. Kwiat, Thaddeus Ladd, Jay Lowell, Dmitri Maslov, Nadya Mason, Anne Y. Matsuura, Robert McDermott, Rod van Meter, Aaron Miller, Jason Orcutt, Mark Saffman, Monika Schleier-Smith, Manish Kumar Singh, Phil Smith, Martin Suchara, Farzam Toudeh-Fallah, Matt Turlington, Benjamin Woods, and Tian Zhong. A roadmap for quantum interconnects. Technical report, Argonne National Lab. (ANL), Argonne, IL (United States), 2022.

[15] D. Main, P. Drmota, D. P. Nadlinger, E. M. Ainley, A. Agrawal, B. C. Nichol, R. Srinivas, G. Araneda, and D. M. Lucas. Distributed quantum computing across an optical network link. *Nature*, 2025. doi:10.1038/s41586-024-08404-x. URL `https://doi.org/10.1038/s41586-024-08404-x`.

[16] Charles H. Bennett and Gilles Brassard. Quantum cryptography: Public key distribution and coin tossing. *Theoretical Computer Science*, 560:7–11, 2014. ISSN 0304-3975.

doi:https://doi.org/10.1016/j.tcs.2014.05.025. URL `https://www.sciencedirect.com/science/article/pii/S0304397514004241`. Theoretical Aspects of Quantum Cryptography – celebrating 30 years of BB84.

[17] Stefano Pirandola, Carlo Ottaviani, Gaetana Spedalieri, Christian Weedbrook, Samuel L Braunstein, Seth Lloyd, Tobias Gehring, Christian S Jacobsen, and Ulrik L Andersen. High-rate measurement-device-independent quantum cryptography. *Nature Photonics*, 9(6):397–402, 2015. ISSN 1749-4893. doi:10.1038/nphoton.2015.83. URL `https://doi.org/10.1038/nphoton.2015.83`.

[18] David P DiVincenzo. The physical implementation of quantum computation. *Fortschritte der Physik: Progress of Physics*, 48(9-11):771–783, 2000.

[19] Sheng-Kai Liao, Wen-Qi Cai, Wei-Yue Liu, Liang Zhang, Yang Li, Ji-Gang Ren, Juan Yin, Qi Shen, Yuan Cao, Zheng-Ping Li, Feng-Zhi Li, Xia-Wei Chen, Li-Hua Sun, Jian-Jun Jia, Jin-Cai Wu, Xiao-Jun Jiang, Jian-Feng Wang, Yong-Mei Huang, Qiang Wang, Yi-Lin Zhou, Lei Deng, Tao Xi, Lu Ma, Tai Hu, Qiang Zhang, Yu-Ao Chen, Nai-Le Liu, Xiang-Bin Wang, Zhen-Cai Zhu, Chao-Yang Lu, Rong Shu, Cheng-Zhi Peng, Jian-Yu Wang, and Jian-Wei Pan. Satellite-to-ground quantum key distribution. *Nature*, 549(7670):43–47, Sep 2017. ISSN 1476-4687. doi:10.1038/nature23655. URL `https://doi.org/10.1038/nature23655`.

[20] Ji-Gang Ren, Ping Xu, Hai-Lin Yong, Liang Zhang, Sheng-Kai Liao, Juan Yin, Wei-Yue Liu, Wen-Qi Cai, Meng Yang, Li Li, Kui-Xing Yang, Xuan Han, Yong-Qiang Yao, Ji Li, Hai-Yan Wu, Song Wan, Lei Liu, Ding-Quan Liu, Yao-Wu Kuang, Zhi-Ping He, Peng Shang, Cheng Guo, Ru-Hua Zheng, Kai Tian, Zhen-Cai Zhu, Nai-Le Liu, Chao-Yang Lu, Rong Shu, Yu-Ao Chen, Cheng-Zhi Peng, Jian-Yu Wang, and Jian-Wei Pan. Ground-to-satellite quantum teleportation. *Nature*, 549(7670):70–73, Sep 2017. ISSN 1476-4687. doi:10.1038/nature23675. URL `https://doi.org/10.1038/nature23675`.

[21] Joe Lykken and David Awschalom. Quantum link: Building the u.s. quantum superhighway. *OSTI*, 10 2018. URL `https://www.osti.gov/biblio/1569247`.

[22] Rajni Bala, Sooryansh Asthana, and V. Ravishankar. Combating errors in quantum communication: an integrated approach. *Scientific Reports*, 13(1):2979, 2023. doi:10.1038/s41598-023-30178-x. URL `https://doi.org/10.1038/s41598-023-30178-x`.

[23] Sreraman Muralidharan, Jungsang Kim, Norbert Lütkenhaus, Mikhail D. Lukin, and Liang Jiang. Ultrafast and fault-tolerant quantum communication across long distances. *Phys. Rev. Lett.*, 112:250501, Jun 2014. doi:10.1103/PhysRevLett.112.250501. URL `https://link.aps.org/doi/10.1103/PhysRevLett.112.250501`.

[24] Gary Wolfowicz, F. Joseph Heremans, Christopher P. Anderson, Shun Kanai, Hosung Seo, Adam Gali, Giulia Galli, and David D. Awschalom. Qubit guidelines for solid-state spin defects, 2020.

[25] Ching-Fuh Lin. *Optical Amplifiers*, pages 107–138. Springer US, Boston, MA, 2004. ISBN 978-1-4757-4178-0. doi:10.1007/978-1-4757-4178-0_4. URL `https://doi.org/10.1007/978-1-4757-4178-0_4`.

[26] Vladimir Bužek and Mark Hillery. Quantum copying: Beyond the no-cloning theorem. *Physical Review A*, 54(3):1844, 1996.

[27] David Awschalom, Karl K. Berggren, Hannes Bernien, Sunil Bhave, Lincoln D. Carr, Paul Davids, Sophia E. Economou, Dirk Englund, Andrei Faraon, Martin Fejer, Saikat Guha, Martin V. Gustafsson, Evelyn Hu, Liang Jiang, Jungsang Kim, Boris Korzh, Prem Kumar, Paul G. Kwiat, Marko Lončar, Mikhail D. Lukin, David A.B. Miller, Christopher Monroe, Sae Woo Nam, Prineha Narang, Jason S. Orcutt, Michael G. Raymer, Amir H. Safavi-Naeini, Maria Spiropulu, Kartik Srinivasan, Shuo Sun, Jelena Vučković, Edo Waks, Ronald Walsworth, Andrew M. Weiner, and Zheshen Zhang. Development of quantum interconnects (quics) for next-generation information technologies. *PRX Quant.*, 2(1):017002, 2021. doi:10.1103/PRXQuantum.2.017002.

[28] Manish Kumar Singh, Liang Jiang, David D. Awschalom, and Supratik Guha. Key device and materials specifications for a repeater enabled quantum internet. *IEEE Transactions on Quantum Engineering*, 2:1–9, 2021. doi:10.1109/TQE.2021.3098440.

[29] H.-J. Briegel, W. Dür, J. I. Cirac, and P. Zoller. Quantum repeaters: The role of imperfect local operations in quantum communication. *Phys. Rev. Lett.*, 81:5932–5935, Dec 1998. doi:10.1103/PhysRevLett.81.5932. URL `https://link.aps.org/doi/10.1103/PhysRevLett.81.5932`.

[30] Sreraman Muralidharan, Linshu Li, Jungsang Kim, Norbert Lütkenhaus, Mikhail D. Lukin, and Liang Jiang. Optimal architectures for long distance quantum communication. *Scientific Reports*, 6(1):20463, Feb 2016. ISSN 2045-2322. doi:10.1038/srep20463. URL `https://doi.org/10.1038/srep20463`.

[31] Andreas Reiserer and Gerhard Rempe. Cavity-based quantum networks with single atoms and optical photons. *Rev. Mod. Phys.*, 87:1379–1418, Dec 2015. doi:10.1103/RevModPhys.87.1379. URL `https://link.aps.org/doi/10.1103/RevModPhys.87.1379`.

[32] W J Munro, A M Stephens, S J Devitt, K A Harrison, and Kae Nemoto. Quantum communication without the necessity of quantum memories. *Nature Photonics*, 6(11): 777–781, 2012. ISSN 1749-4893. doi:10.1038/nphoton.2012.243. URL `https://doi.org/10.1038/nphoton.2012.243`.

[33] Koji Azuma, Kiyoshi Tamaki, and Hoi-Kwong Lo. All-photonic quantum repeaters. *Nature Communications*, 6(1):6787, 2015. ISSN 2041-1723. doi:10.1038/ncomms7787. URL `https://doi.org/10.1038/ncomms7787`.

[34] Zheng-Da Li, Rui Zhang, Xu-Fei Yin, Li-Zheng Liu, Yi Hu, Yu-Qiang Fang, Yue-Yang Fei, Xiao Jiang, Jun Zhang, Li Li, Nai-Le Liu, Feihu Xu, Yu-Ao Chen, and

Jian-Wei Pan. Experimental quantum repeater without quantum memory. *Nature Photonics*, 13(9):644–648, 2019. ISSN 1749-4893. doi:10.1038/s41566-019-0468-5. URL `https://doi.org/10.1038/s41566-019-0468-5`.

[35] Argonne National Laboratory. New quantum loop provides long national testbed for quantum communication technology. *Argonne Press Release*, 2020. URL `https://www.anl.gov/article/new-quantum-loop-provides-long-national-testbed-for-quantum-communication-technology`.

[36] Xiao Min Hu, Yu Guo, Bi Heng Liu, Chuan Feng Li, and Guang Can Guo. Progress in quantum teleportation, 6 2023. ISSN 25225820.

[37] Stefanie Barz, Gunther Cronenberg, Anton Zeilinger, and Philip Walther. Heralded generation of entangled photon pairs. *Nature Photonics*, 4(8):553–556, 2010. ISSN 1749-4893. doi:10.1038/nphoton.2010.156. URL `https://doi.org/10.1038/nphoton.2010.156`.

[38] Nicolas Gisin and Rob Thew. Quantum communication. *Nature Photonics*, 1(3):165–171, 2007. doi:10.1038/nphoton.2007.22. URL `https://doi.org/10.1038/nphoton.2007.22`.

[39] Félix Bussières, Nicolas Sangouard, Mikael Afzelius, Hugues de Riedmatten, Christoph Simon, and Wolfgang Tittel and. Prospective applications of optical quantum memories. *Journal of Modern Optics*, 60(18):1519–1537, 2013. doi:10.1080/09500340.2013.856482. URL `https://doi.org/10.1080/09500340.2013.856482`.

[40] Lee C. Bassett, Audrius Alkauskas, Annemarie L. Exarhos, and Kai-Mei C. Fu. Quantum defects by design. *Nanophotonics*, 8(11):1867–1888, 2019. doi:doi:10.1515/nanoph-2019-0211. URL `https://doi.org/10.1515/nanoph-2019-0211`.

[41] Andreas Wallucks, Igor Marinković, Bas Hensen, Robert Stockill, and Simon Gröblacher. A quantum memory at telecom wavelengths. *Nature Physics*, 16:772–777, 7 2020. ISSN 17452481. doi:10.1038/s41567-020-0891-z.

[42] Holger P. Specht, Christian Nölleke, Andreas Reiserer, Manuel Uphoff, Eden Figueroa, Stephan Ritter, and Gerhard Rempe. A single-atom quantum memory. *Nature*, 473 (7346):190–193, 2011. doi:10.1038/nature09997. URL `https://doi.org/10.1038/nature09997`.

[43] A. Sipahigil, M. L. Goldman, E. Togan, Y. Chu, M. Markham, D. J. Twitchen, A. S. Zibrov, A. Kubanek, and M. D. Lukin. Quantum interference of single photons from remote nitrogen-vacancy centers in diamond. *Phys. Rev. Lett.*, 108:143601, Apr 2012. doi:10.1103/PhysRevLett.108.143601. URL `https://link.aps.org/doi/10.1103/PhysRevLett.108.143601`.

[44] Hannes Bernien, Lilian Childress, Lucio Robledo, Matthew Markham, Daniel Twitchen, and Ronald Hanson. Two-photon quantum interference from separate nitrogen vacancy centers in diamond. *Phys. Rev. Lett.*, 108:043604, Jan 2012. doi:10.1103/PhysRevLett.108.043604. URL `https://link.aps.org/doi/10.1103/PhysRevLett.108.043604`.

[45] Peng-Bo Li, Yong-Chun Liu, S.-Y. Gao, Ze-Liang Xiang, Peter Rabl, Yun-Feng Xiao, and Fu-Li Li. Hybrid quantum device based on *nv* centers in diamond nanomechanical resonators plus superconducting waveguide cavities. *Phys. Rev. Appl.*, 4:044003, Oct 2015. doi:10.1103/PhysRevApplied.4.044003. URL `https://link.aps.org/doi/10.1103/PhysRevApplied.4.044003`.

[46] W. L. Yang, Z. Q. Yin, Y. Hu, M. Feng, and J. F. Du. High-fidelity quantum memory using nitrogen-vacancy center ensemble for hybrid quantum computation. *Phys. Rev. A*, 84:010301, Jul 2011. doi:10.1103/PhysRevA.84.010301. URL `https://link.aps.org/doi/10.1103/PhysRevA.84.010301`.

[47] SangKook Choi, Manish Jain, and Steven G. Louie. Mechanism for optical initialization of spin in nv^- center in diamond. *Phys. Rev. B*, 86:041202, Jul 2012. doi:10.1103/PhysRevB.86.041202. URL `https://link.aps.org/doi/10.1103/PhysRevB.86.041202`.

[48] Y Matsuzaki, H Morishita, T Shimooka, T Tashima, K Kakuyanagi, K Semba, W J Munro, H Yamaguchi, N Mizuochi, and S Saito. Optically detected magnetic resonance of high-density ensemble of nv centers in diamond. *Journal of Physics: Condensed Matter*, 28(27):275302, may 2016. doi:10.1088/0953-8984/28/27/275302. URL `https://dx.doi.org/10.1088/0953-8984/28/27/275302`.

[49] Brian G Wybourne and William F Meggers. *Spectroscopic properties of rare earths.* American Institute of Physics, 1965. ISBN 9780470965078.

[50] Guokui Liu and Bernard Jacquier. *Spectroscopic properties of rare earths in optical materials*, volume 83 of *Springer Series in Materials Science.* Springer Science & Business Media, 2006. ISBN 9783642062834.

[51] Manjin Zhong, Morgan P Hedges, Rose L Ahlefeldt, John G Bartholomew, Sarah E Beavan, Sven M Wittig, Jevon J Longdell, and Matthew J Sellars. Optically addressable nuclear spins in a solid with a six-hour coherence time. *Nature*, 517 (7533):177–180, 2015. ISSN 1476-4687. doi:10.1038/nature14025. URL `https://doi.org/10.1038/nature14025`.

[52] Yang Liu, Zheru Qiu, Xinru Ji, Anton Lukashchuk, Jijun He, Johann Riemensberger, Martin Hafermann, Rui Ning Wang, Junqiu Liu, Carsten Ronning, and Tobias J. Kippenberg. A photonic integrated circuit–based erbium-doped amplifier. *Science*, 376(6599):1309–1313, 2022. doi:10.1126/science.abo2631. URL `https://www.science.org/doi/abs/10.1126/science.abo2631`.

[53] Angela B Seddon, Zhuoqi Tang, David Furniss, Slawomir Sujecki, and Trevor M Benson. Progress in rare-earth-doped mid-infrared fiber lasers. *Opt. Express*, 18(25): 26704–26719, Dec 2010. doi:10.1364/OE.18.026704. URL `https://opg.optica.org/oe/abstract.cfm?URI=oe-18-25-26704`.

[54] Yuechen Jia, Jiangwei Wu, Xiaoli Sun, Xiongshuo Yan, Ranran Xie, Lei Wang, Yuping Chen, and Feng Chen. Integrated photonics based on rare-earth ion-doped thin-film lithium niobate. *Laser & Photonics Reviews*, 16(9):2200059, 2022. doi:https://doi.org/10.1002/lpor.202200059. URL `https://onlinelibrary.wiley.com/doi/abs/10.1002/lpor.202200059`.

[55] Alexandre Fossati, Shuping Liu, Jenny Karlsson, Akio Ikesue, Alexandre Tallaire, Alban Ferrier, Diana Serrano, and Philippe Goldner. A frequency-multiplexed coherent electro-optic memory in rare earth doped nanoparticles. *Nano Letters*, 20(10):7087–7093, 10 2020. doi:10.1021/acs.nanolett.0c02200. URL `https://doi.org/10.1021/acs.nanolett.0c02200`.

[56] Alexander Ulanowski, Johannes Früh, Fabian Salamon, Adrian Holzäpfel, and Andreas Reiserer. Spectral multiplexing of rare-earth emitters in a co-doped crystalline membrane. *Advanced Optical Materials*, 12(15):2302897, 2024. doi:https://doi.org/10.1002/adom.202302897. URL `https://onlinelibrary.wiley.com/doi/abs/10.1002/adom.202302897`.

[57] Marianne Le Dantec, Miloš Rančić, Sen Lin, Eric Billaud, Vishal Ranjan, Daniel Flanigan, Sylvain Bertaina, Thierry Chaneliere, Philippe Goldner, Andreas Erb, Ren Bao Liu, Daniel Esteve, Denis Vion, Emmanuel Flurin, and Patrice Bertet. Twenty-three-millisecond electron spin coherence of erbium ions in a natural-abundance crystal. *Science Advances*, 7(51), 2021. ISSN 23752548. doi:10.1126/sciadv.abj9786.

[58] Tian Zhong, Jonathan M Kindem, Jake Rochman, and Andrei Faraon. Interfacing broadband photonic qubits to on-chip cavity-protected rare-earth ensembles. *Nature Communications*, 8(1):14107, 2017. ISSN 2041-1723. doi:10.1038/ncomms14107. URL `https://doi.org/10.1038/ncomms14107`.

[59] A. M. Dibos, M. Raha, C. M. Phenicie, and J. D. Thompson. Atomic source of single photons in the telecom band. *Phys. Rev. Lett.*, 120:243601, Jun 2018. doi:10.1103/PhysRevLett.120.243601. URL `https://link.aps.org/doi/10.1103/PhysRevLett.120.243601`.

[60] Christopher M. Phenicie, Paul Stevenson, Sacha Welinski, Brendon C. Rose, Abraham T. Asfaw, Robert J. Cava, Stephen A. Lyon, Nathalie P. de Leon, and Jeff D. Thompson. Narrow optical line widths in erbium implanted in tio2. *Nano Letters*, 19 (12):8928–8933, Dec 2019. ISSN 1530-6984. doi:10.1021/acs.nanolett.9b03831. URL `https://doi.org/10.1021/acs.nanolett.9b03831`.

[61] Manish Kumar Singh, Abhinav Prakash, Gary Wolfowicz, Jianguo Wen, Yizhong Huang, Tijana Rajh, David D. Awschalom, Tian Zhong, and Supratik Guha. Epitaxial Er-doped Y2O3 on silicon for quantum coherent devices. *APL Materials*, 8(3), 2020. ISSN 2166532X. doi:10.1063/1.5142611. URL `https://doi.org/10.1063/1.5142611`.

[62] E. M. Purcell, H. C. Torrey, and R. V. Pound. Resonance absorption by nuclear magnetic moments in a solid. *Phys. Rev.*, 69:37–38, Jan 1946. doi:10.1103/PhysRev.69.37. URL `https://link.aps.org/doi/10.1103/PhysRev.69.37`.

[63] Manish Kumar Singh, Gary Wolfowicz, Jianguo Wen, Sean E Sullivan, Abhinav Prakash, Alan M Dibos, David D Awschalom, F Joseph Heremans, and Supratik Guha. Development of a scalable quantum memory platform – materials science of erbium-doped tio_2 thin films on silicon. *arXiv*, **2022**, feb . DOI: 10.48550/arXiv.2202.05376 (accessed: April 10, 2022).

[64] Alan M. Dibos, Michael T. Solomon, Sean E. Sullivan, Manish K. Singh, Kathryn E. Sautter, Connor P. Horn, Gregory D. Grant, Yulin Lin, Jianguo Wen, F. Joseph Heremans, Supratik Guha, and David D. Awschalom. Purcell Enhancement of Erbium Ions in TiO_2 on Silicon Nanocavities. *Nano Lett.*, 22(16):6530–6536, 2022. ISSN 15306992. doi:10.1021/acs.nanolett.2c01561.

[65] Cheng Ji, Michael T Solomon, Gregory D Grant, Koichi Tanaka, Muchuan Hua, Jianguo Wen, Sagar Kumar Seth, Connor P Horn, Ignas Masiulionis, Manish Kumar Singh, Sean E Sullivan, F Joseph Heremans, David D Awschalom, Supratik Guha, and Alan M Dibos. Nanocavity-Mediated Purcell Enhancement of Er in TiO2 Thin Films Grown via Atomic Layer Deposition. *ACS Nano*, 18(14):9929–9941, apr 2024. ISSN 1936-0851. doi:10.1021/acsnano.3c09878. URL `https://doi.org/10.1021/acsnano.3c09878`.

[66] Shobhit Gupta, Shihan Liu, Chao-Fan Wang, Yizhong Huang, and Tian Zhong. Towards khz optical linewidth, millisecond spin coherence erbium telecom qubits in epitaxial thin films. In *CLEO: Fundamental Science*, pages FTh1A–2. Optica Publishing Group, 2023. doi:10.1364/CLEO_FS.2023.FTh1A.2.

[67] Salim Ourari, Łukasz Dusanowski, Sebastian P. Horvath, Mehmet T. Uysal, Christopher M. Phenicie, Paul Stevenson, Mouktik Raha, Songtao Chen, Robert J. Cava, Nathalie P. de Leon, and Jeff D. Thompson. Indistinguishable telecom band photons from a single er ion in the solid state. *Nature*, 620(7976):977–981, Aug 2023. ISSN 1476-4687. doi:10.1038/s41586-023-06281-4.

[68] Miloš Rančić, Morgan P Hedges, Rose L Ahlefeldt, and Matthew J Sellars. Coherence time of over a second in a telecom-compatible quantum memory storage material. *Nat. Phys.*, 14(1):50–54, 2018. doi:10.1038/nphys4254.

[69] Sebastian P Horvath, Christopher M Phenicie, Salim Ourari, Mehmet T Uysal, Songtao Chen, Łukasz Dusanowski, Mouktik Raha, Paul Stevenson, Adam T Turflinger, Robert J Cava, Nathalie P de Leon, and Jeff D Thompson. Strong purcell enhancement of an optical magnetic dipole transition. *arXiv preprint arXiv:2307.03022*, 2023.

[70] Jake Rochman, Tian Xie, John G Bartholomew, KC Schwab, and Andrei Faraon. Microwave-to-optical transduction with erbium ions coupled to planar photonic and superconducting resonators. *Nat. Commun.*, 14(1):1153, 2023. doi:10.1038/s41467-023-36799-0.

[71] Yong Yu, Dorian Oser, Gaia Da Prato, Emanuele Urbinati, Javier Carrasco Ávila, Yu Zhang, Patrick Remy, Sara Marzban, Simon Gröblacher, and Wolfgang Tittel. Frequency tunable, cavity-enhanced single erbium quantum emitter in the telecom band. *arXiv preprint arXiv:2304.14685*, 2023.

[72] Likai Yang, Sihao Wang, Mohan Shen, Jiacheng Xie, and Hong X. Tang. Controlling single rare earth ion emission in an electro-optical nanocavity. *Nature Communications*, 14, 12 2023. ISSN 20411723. doi:10.1038/s41467-023-37513-w.

[73] Likai Yang, Sihao Wang, and Hong X. Tang. Toward radiative-limited coherence of erbium dopants in a nanophotonic resonator. *Applied Physics Letters*, 123, 9 2023. ISSN 00036951. doi:10.1063/5.0165971.

[74] Lorenz Weiss, Andreas Gritsch, Benjamin Merkel, and Andreas Reiserer. Erbium dopants in nanophotonic silicon waveguides. *Optica*, 8(1):40–41, Jan 2021. doi:10.1364/OPTICA.413330.

[75] Stephan Rinner, Florian Burger, Andreas Gritsch, Jonas Schmitt, and Andreas Reiserer. Erbium emitters in commercially fabricated nanophotonic silicon waveguides. *Nanophotonics*, 12(17):3455–3462, 2023. doi:doi:10.1515/nanoph-2023-0287. URL `https://doi.org/10.1515/nanoph-2023-0287`.

[76] Wen Yang, Wen-Long Ma, and Ren-Bao Liu. Quantum many-body theory for electron spin decoherence in nanoscale nuclear spin baths. *Reports on Progress in Physics*, 80 (1):016001, nov 2016. doi:10.1088/0034-4885/80/1/016001. URL `https://dx.doi.org/10.1088/0034-4885/80/1/016001`.

[77] Andrei Faraon, Andrei Ruskuc, Ioana Craiciu, Jonathan M Kindem, John G Bartholomew, Jake H Rochman, and Mi Lei. Towards optical quantum networks based on rare-earth ions and nanophotonics. In *Quantum Computing, Communication, and Simulation*, volume 11699, page 116990Y. SPIE, 2021. doi:10.1117/12.2581709. URL `https://doi.org/10.1117/12.2581709`.

[78] Tian Zhong and Philippe Goldner. Emerging rare-earth doped material platforms for quantum nanophotonics. *Nanophotonics*, 8(11):2003–2015, 2019. doi:10.1515/nanoph-2019-0185. URL `https://doi.org/10.1515/nanoph-2019-0185`.

[79] Mouktik Raha, Songtao Chen, Christopher M. Phenicie, Salim Ourari, Alan M. Dibos, and Jeff D. Thompson. Optical quantum nondemolition measurement of a single rare earth ion qubit. *Nature Communications*, 11(1):1–6, 2020. ISSN 20411723. doi:10.1038/s41467-020-15138-7. URL `http://dx.doi.org/10.1038/s41467-020-15138-7`.

[80] Songtao Chen, Mouktik Raha, Christopher M. Phenicie, Salim Ourari, and Jeff D. Thompson. Parallel single-shot measurement and coherent control of solid-state spins below the diffraction limit. *Science*, 370(6516):592–595, 2020. ISSN 10959203. doi:10.1126/SCIENCE.ABC7821.

[81] Mehmet T. Uysal, Mouktik Raha, Songtao Chen, Christopher M. Phenicie, Salim Ourari, Mengen Wang, Chris G. Van de Walle, Viatcheslav V. Dobrovitski, and Jeff D. Thompson. Coherent control of a nuclear spin via interactions with a rare-earth ion in the solid state. *PRX Quantum*, 4:010323, Mar 2023. doi:10.1103/PRXQuantum.4.010323. URL `https://link.aps.org/doi/10.1103/PRXQuantum.4.010323`.

[82] Mehmet T. Uysal, Łukasz Dusanowski, Haitong Xu, Sebastian P. Horvath, Salim Ourari, Robert J. Cava, Nathalie P. de Leon, and Jeff D. Thompson. Spin-photon entanglement of a single er^{3+} ion in the telecom band, 2024. URL `https://arxiv.org/abs/2406.06515`.

[83] Jonathan M Kindem, Andrei Ruskuc, John G Bartholomew, Jake Rochman, Yan Qi Huan, and Andrei Faraon. Control and single-shot readout of an ion embedded in a nanophotonic cavity. *Nature*, 580(7802):201–204, 2020. ISSN 1476-4687. doi:10.1038/s41586-020-2160-9. URL `https://doi.org/10.1038/s41586-020-2160-9`.

[84] Chun-Ju Wu, Daniel Riedel, Andrei Ruskuc, Ding Zhong, Hyounghan Kwon, and Andrei Faraon. Near-infrared hybrid quantum photonic interface for ^{171}yb^{3+} solid-state qubits. *Phys. Rev. Appl.*, 20:044018, Oct 2023. doi:10.1103/PhysRevApplied.20.044018. URL `https://link.aps.org/doi/10.1103/PhysRevApplied.20.044018`.

[85] A. Ruskuc, C. J. Wu, E. Green, S. L. N. Hermans, W. Pajak, J. Choi, and A. Faraon. Multiplexed entanglement of multi-emitter quantum network nodes. *Nature*, 639(8053): 54–59, 2025. doi:10.1038/s41586-024-08537-z. URL `https://doi.org/10.1038/s41586-024-08537-z`.

[86] John G. Bartholomew, Tian Zhong, Jonathan M. Kindem, Raymond Lopez-Rios, Jake Rochman, Ioana Craiciu, Evan Miyazono, and Andrei Faraon. Controlling rare-earth ions in a nanophotonic resonator using the ac stark shift. *Physical Review A*, 97, 6 2018. ISSN 24699934. doi:10.1103/PhysRevA.97.063854.

[87] Ioana Craiciu, Mi Lei, Jake Rochman, Jonathan M. Kindem, John G. Bartholomew, Evan Miyazono, Tian Zhong, Neil Sinclair, and Andrei Faraon. Nanophotonic quantum storage at telecommunication wavelength. *Phys. Rev. Applied*, 12:024062, Aug 2019. doi:10.1103/PhysRevApplied.12.024062. URL `https://link.aps.org/doi/10.1103/PhysRevApplied.12.024062`.

[88] Ioana Craiciu, Mi Lei, Jake Rochman, John G. Bartholomew, and Andrei Faraon. Multifunctional on-chip storage at telecommunication wavelength for quantum networks. *Optica*, 8(1):114–121, Jan 2021. doi:10.1364/OPTICA.412211. URL `http://www.osapublishing.org/optica/abstract.cfm?URI=optica-8-1-114`.

[89] M. Rančić, M. Le Dantec, S. Lin, S. Bertaina, T. Chanelière, D. Serrano, P. Goldner, R. B. Liu, E. Flurin, D. Estève, D. Vion, and P. Bertet. Electron-spin spectral diffusion in an erbium doped crystal at millikelvin temperatures. *Phys. Rev. B*, 106:144412, Oct 2022. doi:10.1103/PhysRevB.106.144412. URL `https://link.aps.org/doi/10.1103/PhysRevB.106.144412`.

[90] Ionuț Gabriel Balașa, María Alejandra Arranz-Martinez, Pauline Perrin, Midrel Ngandeu Ngambou, Alexandre Hebbrecht, Diana Serrano, Jocelyn Achard, Alexandre Tallaire, and Philippe Goldner. Rare earth-diamond hybrid structures for optical quantum technologies. *Advanced Optical Materials*, 12(31):2401487, 2024. doi:https://doi.org/10.1002/adom.202401487. URL `https://advanced.onlinelibrary.wiley.com/doi/abs/10.1002/adom.202401487`.

[91] Andreas Gritsch, Lorenz Weiss, Johannes Früh, Stephan Rinner, and Andreas Reiserer. Narrow Optical Transitions in Erbium-Implanted Silicon Waveguides. *Phys. Rev. X*, 12(4):041009, oct 2022. ISSN 2160-3308. doi:10.1103/PhysRevX.12.041009. URL `https://link.aps.org/doi/10.1103/PhysRevX.12.041009`.

[92] Andreas Gritsch, Alexander Ulanowski, and Andreas Reiserer. Purcell Enhancement of Single-Photon Emitters in Silicon. *Optica*, 10(6):783, jun 2023. ISSN 2334-2536. doi:10.1364/OPTICA.486167. URL `https://opg.optica.org/abstract.cfm?URI=optica-10-6-783`.

[93] Andreas Gritsch, Alexander Ulanowski, Jakob Pforr, and Andreas Reiserer. Optical single-shot readout of spin qubits in silicon. *Nature Communications*, 16(1):64, 2025. doi:10.1038/s41467-024-55552-9. URL `https://doi.org/10.1038/s41467-024-55552-9`.

[94] Shun Kanai, F. Joseph Heremans, Hosung Seo, Gary Wolfowicz, Christopher P. Anderson, Sean E. Sullivan, Giulia Galli, David D. Awschalom, and Hideo Ohno. Generalized Scaling of Spin Qubit Coherence in over 12,000 Host Materials. *Proc. Natl. Acad. Sci.*, 119(15):e2121808119, apr 2021. ISSN 0027-8424. doi:10.1073/PNAS.2121808119. URL `http://arxiv.org/abs/2102.02986`.

[95] Gregory D Grant, Jiefei Zhang, Ignas Masiulionis, Swarnabha Chattaraj, Kathryn E Sautter, Sean E Sullivan, Rishi Chebrolu, Yuzi Liu, Jessica B Martins, Jens Niklas, et al. Optical and microstructural characterization of er3+ doped epitaxial cerium oxide on silicon. *APL Materials*, 12(2), 2024.

[96] Jiefei Zhang, Gregory D. Grant, Ignas Masiulionis, Michael T. Solomon, Jonathan C. Marcks, Jasleen K. Bindra, Jens Niklas, Alan M. Dibos, Oleg G. Poluektov, F. Joseph

Heremans, Supratik Guha, and David D. Awschalom. Optical and spin coherence of er spin qubits in epitaxial cerium dioxide on silicon. *npj Quantum Information*, 10(1): 119, 2024. doi:10.1038/s41534-024-00903-z. URL `https://doi.org/10.1038/s41534-024-00903-z`.

[97] Rikuto Fukumori, Yizhong Huang, Jun Yang, Haitao Zhang, and Tian Zhong. Sub-kilohertz optical homogeneous linewidth and dephasing mechanisms in er^{3+}:$\mathrm{y}_2\mathrm{o}_3$ ceramics. *Phys. Rev. B*, 101:214202, Jun 2020. doi:10.1103/PhysRevB.101.214202. URL `https://link.aps.org/doi/10.1103/PhysRevB.101.214202`.

[98] Shobhit Gupta, Yizhong Huang, Shihan Liu, Yuxiang Pei, Natasha Tomm, Richard J. Warburton, and Tian Zhong. Dual epitaxial telecom spin-photon interfaces with correlated long-lived coherence, 2023. URL `https://arxiv.org/abs/2310.07120`.

[99] Ian R. Berkman, Alexey Lyasota, Gabriele G. de Boo, John G. Bartholomew, Shao Q. Lim, Brett C. Johnson, Jeffrey C. McCallum, Bin-Bin Xu, Shouyi Xie, Nikolay V. Abrosimov, Hans-Joachim Pohl, Rose L. Ahlefeldt, Matthew J. Sellars, Chunming Yin, and Sven Rogge. Millisecond electron spin coherence time for erbium ions in silicon, 2023. URL `https://arxiv.org/abs/2307.10021`.

[100] Manish K. Singh, Gregory D. Grant, Gary Wolfowicz, Jianguo Wen, Sean E. Sullivan, Abhinav Prakash, Alan M. Dibos, F. Joseph Heremans, David D. Awschalom, and Supratik Guha. Optical and microstructural studies of erbium-doped tio2 thin films on silicon, srtio3, and sapphire. *Journal of Applied Physics*, 136(12):124402, 09 2024. ISSN 0021-8979. doi:10.1063/5.0224010. URL `https://doi.org/10.1063/5.0224010`.

[101] Michael T. Solomon, Martin Koppenhöfer, Mikhail Mamaev, Cheng Ji, Gregory Grant, Ignas Masiulionis, Sean E. Sullivan, F. Joseph Heremans, Supratik Guha, David D. Awschalom, Aashish A. Clerk, and Alan M. Dibos. Anomalous purcell decay of strongly driven inhomogeneous emitters coupled to a cavity. *Optica Quantum*, 2(3):196–205, Jun 2024. doi:10.1364/OPTICAQ.520843. URL `https://opg.optica.org/opticaq/abstract.cfm?URI=opticaq-2-3-196`.

[102] Cheng Ji, Robert M. Pettit, Shobhit Gupta, Gregory D. Grant, Ignas Masiulionis, Ananthesh Sundaresh, Skylar Deckoff-Jones, Max Olberding, Manish K. Singh, F. Joseph Heremans, Supratik Guha, Alan M. Dibos, and Sean E. Sullivan. Isolation of individual er quantum emitters in anatase tio2 on si photonics. *Applied Physics Letters*, 125(8):084001, 08 2024. ISSN 0003-6951. doi:10.1063/5.0222269. URL `https://doi.org/10.1063/5.0222269`.

[103] Jiyuan Zheng, Xingjun Xue, Cheng Ji, Yuan Yuan, Keye Sun, Daniel Rosenmann, Lai Wang, Jiamin Wu, Joe C Campbell, and Supratik Guha. Dynamic-Quenching of a Single-Photon Avalanche Photodetector Using an Adaptive Resistive Switch. *Nat. Commun.*, 13(1):1517, 2022. ISSN 2041-1723. doi:10.1038/s41467-022-29195-7. URL `https://doi.org/10.1038/s41467-022-29195-7`.

[104] Cheng Ji, Zhongbo Zhang, Khalil D. Omotosho, Diana Berman, Byeongdu Lee, Ralu Divan, Supratik Guha, and Elena V. Shevchenko. Porous but mechanically robust all-inorganic antireflective coatings synthesized using polymers of intrinsic microporosity. *ACS Nano*, 16(9):14754–14764, 09 2022. doi:10.1021/acsnano.2c05592. URL `https://doi.org/10.1021/acsnano.2c05592`.

[105] Richard W. Johnson, Adam Hultqvist, and Stacey F. Bent. A brief review of atomic layer deposition: from fundamentals to applications. *Materials Today*, 17(5):236–246, 2014. ISSN 1369-7021. doi:https://doi.org/10.1016/j.mattod.2014.04.026. URL `https://www.sciencedirect.com/science/article/pii/S1369702114001436`.

[106] Steven M. George. Atomic layer deposition: An overview. *Chemical Reviews*, 110(1):111–131, 01 2010. doi:10.1021/cr900056b. URL `https://doi.org/10.1021/cr900056b`.

[107] Necmi Biyikli and Ali Haider. Atomic layer deposition: An enabling technology for the growth of functional nanoscale semiconductors. *Semicond. Sci. Technol.*, 32(9):093002, aug 2017. doi:10.1088/1361-6641/aa7ade. URL `https://dx.doi.org/10.1088/1361-6641/aa7ade`.

[108] David I. Shahin, Marko J. Tadjer, Virginia D. Wheeler, Andrew D. Koehler, Travis J. Anderson, Jr. Eddy, Charles R., and Aris Christou. Electrical Characterization of ALD HfO_2 High-k Dielectrics on $(\overline{2}01)$ β-Ga_2O_3. *Appl. Phys. Lett.*, 112(4):042107, 01 2018. ISSN 0003-6951. doi:10.1063/1.5006276. URL `https://doi.org/10.1063/1.5006276`.

[109] Rafaiel A. Ovanesyan, Ekaterina A. Filatova, Simon D. Elliott, Dennis M. Hausmann, David C. Smith, and Sumit Agarwal. Atomic Layer Deposition of Silicon-Based Dielectrics for Semiconductor Manufacturing: Current Status and Future Outlook. *J. Vac. Sci. Technol.*, 37(6):060904, 09 2019. ISSN 0734-2101. doi:10.1116/1.5113631. URL `https://doi.org/10.1116/1.5113631`.

[110] Bhaswar Chakrabarti, Henry Chan, Khan Alam, Aditya Koneru, Thomas E. Gage, Leonidas E. Ocola, Ralu Divan, Daniel Rosenmann, Abhishek Khanna, Benjamin Grisafe, Toby Sanders, Suman Datta, Ilke Arslan, Subramanian K. R. S. Sankaranarayan, and Supratik Guha. Nanoporous dielectric resistive memories using sequential infiltration synthesis. *ACS Nano*, 15(3):4155–4164, 2021. doi:10.1021/acsnano.0c03201. URL `https://doi.org/10.1021/acsnano.0c03201`.

[111] Diana Berman, Supratik Guha, Byeongdu Lee, Jeffrey W. Elam, Seth B. Darling, and Elena V. Shevchenko. Sequential infiltration synthesis for the design of low refractive index surface coatings with controllable thickness. *ACS Nano*, 11(3):2521–2530, 03 2017. doi:10.1021/acsnano.6b08361. URL `https://doi.org/10.1021/acsnano.6b08361`.

[112] John Rönn, Lasse Karvonen, Christoffer Kauppinen, Alexander Pyymaki Perros, Nasser Peyghambarian, Harri Lipsanen, Antti Säynätjoki, and Zhipei Sun. Atomic Layer Engineering of Er-Ion Distribution in Highly Doped Er:Al_2O_3 for Photoluminescence Enhancement. *ACS Photonics*, 3(11):2040–2048, nov 2016. ISSN 23304022. doi:10.1021/acsphotonics.6b00283.

[113] John Rönn, Weiwei Zhang, Anton Autere, Xavier Leroux, Lasse Pakarinen, Carlos Alonso-Ramos, Antti Säynätjoki, Harri Lipsanen, Laurent Vivien, Eric Cassan, and Zhipei Sun. Ultra-high on-chip optical gain in erbium-based hybrid slot waveguides. *Nat. Commun.*, 10(1):432, 2019. doi:10.1038/s41467-019-08369-w. URL `https://doi.org/10.1038/s41467-019-08369-w`.

[114] Christian Dette, Miguel A Pérez-Osorio, Christopher S Kley, Paul Punke, Christopher E Patrick, Peter Jacobson, Feliciano Giustino, Soon Jung Jung, and Klaus Kern. TiO_2 Anatase with a Bandgap in the Visible Region. *Nano Lett.*, 14(11):6533–6538, nov 2014. ISSN 1530-6984. doi:10.1021/nl503131s. URL `https://doi.org/10.1021/nl503131s`.

[115] Paul Stevenson, Christopher M. Phenicie, Isaiah Gray, Sebastian P. Horvath, Sacha Welinski, Austin M. Ferrenti, Alban Ferrier, Philippe Goldner, Sujit Das, Ramamoorthy Ramesh, Robert J. Cava, Nathalie P. de Leon, and Jeff D. Thompson. Erbium-implanted materials for quantum communication applications. *Phys. Rev. B*, 105: 224106, Jun 2022. doi:10.1103/PhysRevB.105.224106. URL `https://link.aps.org/doi/10.1103/PhysRevB.105.224106`.

[116] Kidae Shin, Isaiah Gray, Guillaume Marcaud, Sebastian P. Horvath, Frederick J. Walker, Jeff D. Thompson, and Charles H. Ahn. Er-Doped Anatase TiO_2 Thin Films on $LaAlO_3$ (001) for Quantum Interconnects (QuICs). *Appl. Phys. Lett.*, 121(8):081902, 08 2022. ISSN 0003-6951. doi:10.1063/5.0107071. URL `https://doi.org/10.1063/5.0107071`.

[117] Janne-Petteri Niemelä, Giovanni Marin, and Maarit Karppinen. Titanium dioxide thin films by atomic layer deposition: A review. *Semicond. Sci. Technol.*, 32(9):093005, aug 2017. doi:10.1088/1361-6641/aa78ce. URL `https://dx.doi.org/10.1088/1361-6641/aa78ce`.

[118] Ryan A. Hackler, Gyeongwon Kang, George C. Schatz, Peter C. Stair, and Richard P. Van Duyne. Analysis of tio_2 atomic layer deposition surface chemistry and evidence of propene oligomerization using surface-enhanced raman spectroscopy. *J. Am. Chem. Soc.*, 141(1):414–422, 01 2019. doi:10.1021/jacs.8b10689. URL `https://doi.org/10.1021/jacs.8b10689`.

[119] S O'Donnell, F Jose, K Shiel, M Snelgrove, C McFeely, E McGill, and R O'Connor. Thermal and plasma enhanced atomic layer deposition of ultrathin tio_2 on silicon from amide and alkoxide precursors: Growth chemistry and photoelectrochemical

performance. *J. Phys. D: Appl. Phys.*, 55(8):085105, nov 2021. doi:10.1088/1361-6463/ac360c. URL `https://dx.doi.org/10.1088/1361-6463/ac360c`.

[120] Hayeong Kim, Jihyeok An, SeonJeong Maeng, Jae-Soo Shin, Eunmi Choi, and Ju-Young Yun. Decomposition characteristics of the ttip (tetraisopropyl orthotitanate) precursor for atomic layer deposition. *Materials*, 15(9):DOI: 10.3390/ma15093021, 2022. ISSN 1996-1944. doi:10.3390/ma15093021. URL `https://www.mdpi.com/1996-1944/15/9/3021`.

[121] Trinh Tu Van, John R. Bargar, and Jane P. Chang. Er coordination in y_2o_3 thin films studied by extended x-ray absorption fine structure. *J. Appl. Phys.*, 100(2):023115, 7/25/2023 2006. doi:10.1063/1.2214299. URL `https://doi.org/10.1063/1.2214299`.

[122] J. Hoang, T. T. Van, M. Sawkar-Mathur, B. Hoex, M. C. M. Van de Sanden, W. M. M. Kessels, R. Ostroumov, K. L. Wang, J. R. Bargar, and J. P. Chang. Optical Properties of Y_2O_3 Thin Films Doped with Spatially Controlled Er^{3+} by Atomic Layer Deposition. *J. Appl. Phys.*, 101(12):123116, 06 2007. ISSN 0021-8979. doi:10.1063/1.2748629. URL `https://doi.org/10.1063/1.2748629`.

[123] T. T. Van, J. Hoang, R. Ostroumov, K. L. Wang, J. R. Bargar, J. Lu, H.-O. Blom, and J. P. Chang. Nanostructure And Temperature-Dependent Photoluminescence Of Er-Doped Y_2O_3 Thin Films for Micro-Optoelectronic Integrated Circuits. *J. Appl. Phys.*, 100(7):073512, 10 2006. ISSN 0021-8979. doi:10.1063/1.2349477. URL `https://doi.org/10.1063/1.2349477`.

[124] Trinh Tu Van and Jane P. Chang. Controlled Erbium Incorporation and Photoluminescence of Er-Doped Y_2O_3. *Appl. Phys. Lett.*, 87(1):011907, 07 2005. ISSN 0003-6951. doi:10.1063/1.1984082. URL `https://doi.org/10.1063/1.1984082`.

[125] Jaan Aarik, Aleks Aidla, Teet Uustare, and Väino Sammelselg. Morphology and structure of tio_2 thin films grown by atomic layer deposition. *J. Cryst. Growth*, 148(3):268–275, 1995. ISSN 0022-0248. doi:https://doi.org/10.1016/0022-0248(94)00874-4. URL `https://www.sciencedirect.com/science/article/pii/0022024894008744`.

[126] Samantha Roberts, Xingchen Ji, Jaime Cardenas, Mateus Corato-Zanarella, and Michal Lipson. Measurements and modeling of atomic-scale sidewall roughness and losses in integrated photonic devices. *Advanced Optical Materials*, 10(18):2102073, 2022. doi:https://doi.org/10.1002/adom.202102073. URL `https://onlinelibrary.wiley.com/doi/abs/10.1002/adom.202102073`.

[127] Salvatore Surdo and Giuseppe Barillaro. Impact of Fabrication and Bioassay Surface Roughness on the Performance of Label-Free Resonant Biosensors Based On One-Dimensional Photonic Crystal Microcavities. *ACS Sensors*, 5(9):2894–2902, sep 2020. doi:10.1021/acssensors.0c01183. URL `https://doi.org/10.1021/acssensors.0c01183`.

[128] Aliaksandr Sharstniou, Stanislau Niauzorau, Anna L. Hardison, Matthew Puckett, Neil Krueger, Judson D. Ryckman, and Bruno Azeredo. Roughness suppression in electrochemical nanoimprinting of si for applications in silicon photonics. *Advanced Materials*, 34(43):2206608, 2022. doi:https://doi.org/10.1002/adma.202206608. URL `https://advanced.onlinelibrary.wiley.com/doi/abs/10.1002/adma.202206608`.

[129] Konstantin Lomakin, Gerald Gold, and Klaus Helmreich. Analytical waveguide model precisely predicting loss and delay including surface roughness. *IEEE Transactions on Microwave Theory and Techniques*, 66(6):2649–2662, 2018. doi:10.1109/TMTT.2018.2827383.

[130] Juan E Sicre, J T Dubois, K J Eisentraut, and R E Sievers. Volatile Lanthanide Chelates. ii. Vapor Pressures, Heats of Vaporization, and Heats of Sublimation. *J. Am. Chem. Soc.*, 91(13):3476–3481, jun 1969. ISSN 0002-7863. doi:10.1021/ja01041a011. URL `https://doi.org/10.1021/ja01041a011`.

[131] M. Horprathum, P. Chindaudom, P. Limnonthakul, P. Eiamchai, N. Nuntawong, V. Patthanasettakul, A. Pokaipisit, and P. Limsuwan. Fabrication and characterization of hydrophilic tio_2 thin films on unheated substrates prepared by pulsed dc reactive magnetron sputtering. *J. Nanomater.*, 2010:DOI: 10.1155/2010/841659, jan 2010. ISSN 1687-4110. doi:10.1155/2010/841659. URL `https://doi.org/10.1155/2010/841659`.

[132] Peter Zaumseil. High-Resolution Characterization of the Forbidden Si 200 and Si 222 Reflections. *J. Appl. Crystallogr.*, 48(Pt 2):528–532, apr 2015. ISSN 0021-8898 (Print). doi:10.1107/S1600576715004732.

[133] Ahti Niilisk, Mart Moppel, Martti Pärs, Ilmo Sildos, Taavi Jantson, Tea Avarmaa, Raivo Jaaniso, and Jaan Aarik. Structural study of tio_2 thin films by micro-raman spectroscopy. *Open Phys.*, 4(1):105–116, 2006. doi:doi:10.1007/s11534-005-0009-3. URL `https://doi.org/10.1007/s11534-005-0009-3`.

[134] M. P. Hehlen, N. J. Cockroft, T. R. Gosnell, A. J. Bruce, G. Nykolak, and J. Shmulovich. Uniform upconversion in high-concentration er^{3+}-doped soda lime silicate and aluminosilicate glasses. *Opt. Lett.*, 22(11):772–774, Jun 1997. doi:10.1364/OL.22.000772. URL `https://opg.optica.org/ol/abstract.cfm?URI=ol-22-11-772`.

[135] A. Vonderhaar, M. P. Stone, J. Campbell, T. W. Hawkins, J. Ballato, and P. D. Dragic. Concentration quenching and clustering effects in er:yag-derived all-glass optical fiber. *Opt. Mater. Express*, 11(10):3587–3599, Oct 2021. doi:10.1364/OME.437825. URL `https://opg.optica.org/ome/abstract.cfm?URI=ome-11-10-3587`.

[136] Wenqin Luo, Chengyu Fu, Renfu Li, Yongsheng Liu, Haomiao Zhu, and Xueyuan Chen. Er^{3+}-Doped Anatase TiO_2 Nanocrystals: Crystal-Field Levels, Excited-State

Dynamics, Upconversion, and Defect Luminescence. *Small*, 7(21):3046–3056, 2011. ISSN 16136810. doi:10.1002/smll.201100838.

[137] S. Sedky, A. Witvrouw, H. Bender, and K. Baert. Experimental determination of the maximum post-process annealing temperature for standard CMOS wafers. *IEEE Trans. Electron Devices*, 48(2):377–385, 2001. doi:10.1109/16.902741.

[138] Bahaa E A Saleh and Malvin Carl Teich. *Fundamentals of photonics; 2nd ed.* Wiley series in pure and applied optics. Wiley, New York, NY, 2007. URL `https://cds.cern.ch/record/1084451`.

[139] Serge Haroche, J. Raimond, and Pierre Meystre. Exploring the quantum: Atoms, cavities, and photons. *Physics Today - PHYS TODAY*, 60, 08 2007. doi:10.1063/1.2774103.

[140] G S Agarwal. *Quantum optics*. Cambridge University Press, 2012.

[141] Igor A. Sukhoivanov and Igor V. Guryev. *Introduction to Photonic Crystals*, pages 1–12. Springer Berlin Heidelberg, Berlin, Heidelberg, 2009. ISBN 978-3-642-02646-1. doi:10.1007/978-3-642-02646-1_1. URL `https://doi.org/10.1007/978-3-642-02646-1_1`.

[142] John D. Joannopoulos, Steven G. Johnson, Joshua N. Winn, and Robert D. Meade. *Photonic Crystals: Molding the Flow of Light*. Princeton University Press, USA, 2nd edition, 2008. ISBN 0691124566.

[143] Yoshihiro Akahane, Takashi Asano, Bong-Shik Song, and Susumu Noda. High-Q photonic nanocavity in a two-dimensional photonic crystal. *Nature*, 425(6961):944–947, 2003. ISSN 1476-4687. doi:10.1038/nature02063. URL `https://doi.org/10.1038/nature02063`.

[144] P. Lalanne, C. Sauvan, and J.P. Hugonin. Photon confinement in photonic crystal nanocavities. *Laser & Photonics Reviews*, 2(6):514–526, 2008. doi:https://doi.org/10.1002/lpor.200810018. URL `https://onlinelibrary.wiley.com/doi/abs/10.1002/lpor.200810018`.

[145] Jasper Chan. Laser cooling of an optomechanical crystal resonator to its quantum ground state of motion. 2012. URL `https://api.semanticscholar.org/CorpusID:124076949`.

[146] Ulrich H.P. Fischer-Hirchert. *Photonic packaging sourcebook: Fiber-chip coupling for optical components, basic calculations, modules*. 2015. ISBN 9783642253768. doi:10.1007/978-3-642-25376-8.

[147] Gyeongho Son, Seungjun Han, Jongwoo Park, Kyungmok Kwon, and Kyoungsik Yu. High-efficiency broadband light coupling between optical fibers and photonic integrated circuits. *Nanophotonics*, 7:1845–1864, 2018. ISSN 21928614. doi:10.1515/nanoph-2018-0075.

[148] Minhao Pu, Liu Liu, Haiyan Ou, Kresten Yvind, and Jørn M. Hvam. Ultra-low-loss inverted taper coupler for silicon-on-insulator ridge waveguide. *Optics Communications*, 283:3678–3682, 2010. ISSN 00304018. doi:10.1016/j.optcom.2010.05.034. URL `http://dx.doi.org/10.1016/j.optcom.2010.05.034`.

[149] Seán M. Meenehan, Justin D. Cohen, Simon Gröblacher, Jeff T. Hill, Amir H. Safavi-Naeini, Markus Aspelmeyer, and Oskar Painter. Silicon optomechanical crystal resonator at millikelvin temperatures. *Phys. Rev. A*, 90:011803, Jul 2014. doi:10.1103/PhysRevA.90.011803. URL `https://link.aps.org/doi/10.1103/PhysRevA.90.011803`.

[150] C. P. Michael, H. B. Yuen, V. A. Sabnis, T. J. Johnson, R. Sewell, R. Smith, A. Jamora, A. Clark, S. Semans, P. B. Atanackovic, and O. Painter. Growth, processing, and optical properties of epitaxial er_2o_3 on silicon. *Opt. Express*, 16(24):19649–19666, Nov 2008. doi:10.1364/OE.16.019649. URL `https://opg.optica.org/oe/abstract.cfm?URI=oe-16-24-19649`.

[151] Mi Lei, Rikuto Fukumori, Jake Rochman, Bihui Zhu, Manuel Endres, Joonhee Choi, and Andrei Faraon. Many-body cavity quantum electrodynamics with driven inhomogeneous emitters. *Nature*, 617(7960):271–276, May 2023. ISSN 1476-4687. doi:10.1038/s41586-023-05884-1. URL `https://doi.org/10.1038/s41586-023-05884-1`.

[152] F. De Martini, G. Innocenti, G. R. Jacobovitz, and P. Mataloni. Anomalous Spontaneous Emission Time in a Microscopic Optical Cavity. *Phys. Rev. Lett.*, 59(26): 2955–2958, December 1987. doi:10.1103/PhysRevLett.59.2955.

[153] S. Mosor, J. Hendrickson, B. C. Richards, J. Sweet, G. Khitrova, H. M. Gibbs, T. Yoshie, A. Scherer, O. B. Shchekin, and D. G. Deppe. Scanning a photonic crystal slab nanocavity by condensation of xenon. *Applied Physics Letters*, 87(14):141105, September 2005. ISSN 0003-6951. doi:10.1063/1.2076435.

[154] John G. Bartholomew, Karmel de Oliveira Lima, Alban Ferrier, and Philippe Goldner. Optical Line Width Broadening Mechanisms at the 10 kHz Level in Eu3+:Y2O3 Nanoparticles. *Nano Lett.*, 17(2):778–787, February 2017. ISSN 1530-6984. doi:10.1021/acs.nanolett.6b03949.

[155] Shuping Liu, Diana Serrano, Alexandre Fossati, Alexandre Tallaire, Alban Ferrier, and Philippe Goldner. Controlled size reduction of rare earth doped nanoparticles for optical quantum technologies. *RSC Adv.*, 8(65):37098–37104, November 2018. ISSN 2046-2069. doi:10.1039/C8RA07246A.

[156] A. N. Craddock, J. Hannegan, D. P. Ornelas-Huerta, J. D. Siverns, A. J. Hachtel, E. A. Goldschmidt, J. V. Porto, Q. Quraishi, and S. L. Rolston. Quantum interference between photons from an atomic ensemble and a remote atomic ion. *Phys. Rev. Lett.*, 123:213601, Nov 2019. doi:10.1103/PhysRevLett.123.213601. URL `https://link.aps.org/doi/10.1103/PhysRevLett.123.213601`.

[157] Sören Wengerowsky, Siddarth Koduru Joshi, Fabian Steinlechner, Hannes Hübel, and Rupert Ursin. An entanglement-based wavelength-multiplexed quantum communication network. *Nature*, 564(7735):225–228, 2018. doi:10.1038/s41586-018-0766-y. URL `https://doi.org/10.1038/s41586-018-0766-y`.

[158] Julián Tachella, Yoann Altmann, Nicolas Mellado, Aongus McCarthy, Rachael Tobin, Gerald S. Buller, Jean-Yves Tourneret, and Stephen McLaughlin. Real-time 3d reconstruction from single-photon lidar data using plug-and-play point cloud denoisers. *Nature Communications*, 10(1):4984, 2019. doi:10.1038/s41467-019-12943-7. URL `https://doi.org/10.1038/s41467-019-12943-7`.

[159] S. Cova, M. Ghioni, A. Lacaita, C. Samori, and F. Zappa. Avalanche photodiodes and quenching circuits for single-photon detection. *Appl. Opt.*, 35(12):1956–1976, Apr 1996. doi:10.1364/AO.35.001956. URL `https://opg.optica.org/ao/abstract.cfm?URI=ao-35-12-1956`.

[160] Jun Zhang, Mark A Itzler, Hugo Zbinden, and Jian-Wei Pan. Advances in ingaas/inp single-photon detector systems for quantum communication. *Light: Science & Applications*, 4(5):e286–e286, 2015. doi:10.1038/lsa.2015.59. URL `https://doi.org/10.1038/lsa.2015.59`.

[161] Zhongrui Wang, Saumil Joshi, Sergey E. Savel'ev, Hao Jiang, Rivu Midya, Peng Lin, Miao Hu, Ning Ge, John Paul Strachan, Zhiyong Li, Qing Wu, Mark Barnell, Geng-Lin Li, Huolin L. Xin, R. Stanley Williams, Qiangfei Xia, and J. Joshua Yang. Memristors with diffusive dynamics as synaptic emulators for neuromorphic computing. *Nature Materials*, 16(1):101–108, 2017. doi:10.1038/nmat4756. URL `https://doi.org/10.1038/nmat4756`.

[162] Sushant Sonde, Bhaswar Chakrabarti, Yuzi Liu, Kiran Sasikumar, Jianqiang Lin, Liliana Stan, Ralu Divan, Leonidas E. Ocola, Daniel Rosenmann, Pabitra Choudhury, Kai Ni, Subramanian K. R. S. Sankaranarayanan, Suman Datta, and Supratik Guha. Silicon compatible sn-based resistive switching memory. *Nanoscale*, 10:9441–9449, 2018. doi:10.1039/C8NR01540F. URL `http://dx.doi.org/10.1039/C8NR01540F`.

[163] Mario Lanza, H.-S. Philip Wong, Eric Pop, Daniele Ielmini, Dimitri Strukov, Brian C. Regan, Luca Larcher, Marco A. Villena, J. Joshua Yang, Ludovic Goux, Attilio Belmonte, Yuchao Yang, Francesco M. Puglisi, Jinfeng Kang, Blanka Magyari-Köpe, Eilam Yalon, Anthony Kenyon, Mark Buckwell, Adnan Mehonic, Alexander Shluger, Haitong Li, Tuo-Hung Hou, Boris Hudec, Deji Akinwande, Ruijing Ge, Stefano Ambrogio, Juan B. Roldan, Enrique Miranda, Jordi Suñe, Kin Leong Pey, Xing Wu, Nagarajan Raghavan, Ernest Wu, Wei D. Lu, Gabriele Navarro, Weidong Zhang, Huaqiang Wu, Runwei Li, Alexander Holleitner, Ursula Wurstbauer, Max C. Lemme, Ming Liu, Shibing Long, Qi Liu, Hangbing Lv, Andrea Padovani, Paolo Pavan, Ilia Valov, Xu Jing, Tingting Han, Kaichen Zhu, Shaochuan Chen, Fei Hui, and Yuanyuan Shi.

Recommended methods to study resistive switching devices. *Advanced Electronic Materials*, 5(1):1800143, 2019. doi:https://doi.org/10.1002/aelm.201800143. URL `https://advanced.onlinelibrary.wiley.com/doi/abs/10.1002/aelm.201800143`.

[164] Qi Lin, Yi Li, Ming Xu, Qu Cheng, Hang Qian, Jinlong Feng, Hao Tong, and Xiangshui Miao. Dual-layer selector with excellent performance for cross-point memory applications. *IEEE Electron Device Letters*, 39(4):496–499, apr 2018. doi:10.1109/led.2018.2808465. URL `https://doi.org/10.1109/led.2018.2808465`.

[165] Wouter Devulder, Karl Opsomer, Felix Seidel, Attilio Belmonte, Robert Muller, Bob De Schutter, Hugo Bender, Wilfried Vandervorst, Sven Van Elshocht, Malgorzata Jurczak, Ludovic Goux, and Christophe Detavernier. Influence of carbon alloying on the thermal stability and resistive switching behavior of copper-telluride based cbram cells. *ACS Applied Materials & Interfaces*, 5(15):6984–6989, 08 2013. doi:10.1021/am4010946. URL `https://doi.org/10.1021/am4010946`.

[166] Stephan Menzel, Moritz von Witzleben, Viktor Havel, and Ulrich Böttger. The ultimate switching speed limit of redox-based resistive switching devices. *Faraday Discuss.*, 213:197–213, 2019. doi:10.1039/C8FD00117K. URL `http://dx.doi.org/10.1039/C8FD00117K`.

[167] D. Marano, M. Belluso, G. Bonanno, S. Billotta, A. Grillo, S. Garozzo, G. Romeo, O. Catalano, G. La Rosa, G. Sottile, D. Impiombato, and S. Giarrusso. Silicon photomultipliers electrical model extensive analytical analysis. *IEEE Transactions on Nuclear Science*, 61(1):23–34, 2014. doi:10.1109/TNS.2013.2283231.

[168] Vitali Savuskan, Michael Javitt, Gil Visokolov, Igor Brouk, and Yael Nemirovsky. Selecting single photon avalanche diode (spad) passive-quenching resistance: An approach. *IEEE Sensors Journal*, 13(6):2322–2328, 2013. doi:10.1109/JSEN.2013.2253603.

[169] Henri Dautet, Pierre Deschamps, Bruno Dion, Andrew D. MacGregor, Darleene MacSween, Robert J. McIntyre, Claude Trottier, and Paul P. Webb. Photon counting techniques with silicon avalanche photodiodes. *Appl. Opt.*, 32(21):3894–3900, Jul 1993. doi:10.1364/AO.32.003894. URL `https://opg.optica.org/ao/abstract.cfm?URI=ao-32-21-3894`.

[170] Dalibor Biolek, Massimiliano Di Ventra, and Yuriy V. Pershin. Reliable spice simulations of memristors, memcapacitors and meminductors. *arXiv: Computational Physics*, 2013. URL `https://api.semanticscholar.org/CorpusID:3145654`.

[171] Jorik van de Groep, Pierpaolo Spinelli, and Albert Polman. Single-step soft-imprinted large-area nanopatterned antireflection coating. *Nano Letters*, 15(6):4223–4228, 06 2015. doi:10.1021/acs.nanolett.5b01623. URL `https://doi.org/10.1021/acs.nanolett.5b01623`.

[172] Shuliang Dou, Hongbo Xu, Jiupeng Zhao, Ke Zhang, Na Li, Yipeng Lin, Lei Pan, and Yao Li. Bioinspired microstructured materials for optical and thermal regulation. *Advanced Materials*, 33(6):2000697, 2021. doi:https://doi.org/10.1002/adma.202000697. URL `https://advanced.onlinelibrary.wiley.com/doi/abs/10.1002/adma.202000697`.

[173] Max Born, Emil Wolf, A. B. Bhatia, P. C. Clemmow, D. Gabor, A. R. Stokes, A. M. Taylor, P. A. Wayman, and W. L. Wilcock. *Principles of Optics: Electromagnetic Theory of Propagation, Interference and Diffraction of Light*. Cambridge University Press, 7 edition, 1999.

[174] Tero Pilvi, Esa Puukilainen, Ulrich Kreissig, Markku Leskelä, and Mikko Ritala. Atomic layer deposition of mgf2 thin films using taf5 as a novel fluorine source. *Chemistry of Materials*, 20(15):5023–5028, 08 2008. doi:10.1021/cm800948k. URL `https://doi.org/10.1021/cm800948k`.

[175] Younghee Lee, Huaxing Sun, Matthias J. Young, and Steven M. George. Atomic layer deposition of metal fluorides using hf–pyridine as the fluorine precursor. *Chemistry of Materials*, 28(7):2022–2032, 04 2016. doi:10.1021/acs.chemmater.5b04360. URL `https://doi.org/10.1021/acs.chemmater.5b04360`.

[176] Tero Pilvi, Timo Hatanpää, Esa Puukilainen, Kai Arstila, Martin Bischoff, Ute Kaiser, Norbert Kaiser, Markku Leskelä, and Mikko Ritala. Study of a novel ald process for depositing mgf2 thin films. *J. Mater. Chem.*, 17:5077–5083, 2007. doi:10.1039/B710903B. URL `http://dx.doi.org/10.1039/B710903B`.

[177] N. Li, Y. D. Li, Y. B. Wang, M. Li, Y. Cheng, Y. H. Wu, and Y. F. Zheng. Corrosion resistance and cytotoxicity of a mgf2 coating on biomedical mg–1ca alloy via vacuum evaporation deposition method. *Surface and Interface Analysis*, 45(8):1217–1222, 2013. doi:https://doi.org/10.1002/sia.5257. URL `https://analyticalsciencejournals.onlinelibrary.wiley.com/doi/abs/10.1002/sia.5257`.

[178] J. Q. Xi, Jong Kyu Kim, and E. F. Schubert. Silica nanorod-array films with very low refractive indices. *Nano Letters*, 5(7):1385–1387, 07 2005. doi:10.1021/nl050698k. URL `https://doi.org/10.1021/nl050698k`.

[179] Lu Han and Hongping Zhao. Surface antireflection properties of gan nanostructures with various effective refractive index profiles. *Opt. Express*, 22(26):31907–31916, Dec 2014. doi:10.1364/OE.22.031907. URL `https://opg.optica.org/oe/abstract.cfm?URI=oe-22-26-31907`.

[180] Matthias Kraus, Zhaolu Diao, Klaus Weishaupt, Joachim P. Spatz, Kerstin Täschner, Hagen Bartzsch, Ralph Schmittgens, and Robert Brunner. Combined ‘moth-eye’ structured and graded index-layer anti-reflecting coating for high index glasses. *Opt. Express*, 27(24):34655–34664, Nov 2019. doi:10.1364/OE.27.034655. URL `https://opg.optica.org/oe/abstract.cfm?URI=oe-27-24-34655`.

[181] P. Spinelli, M. A. Verschuuren, and A. Polman. Broadband omnidirectional antireflection coating based on subwavelength surface mie resonators. *Nature Communications*, 3(1):692, 2012. doi:10.1038/ncomms1691. URL `https://doi.org/10.1038/ncomms1691`.

[182] Michael Hausner. *Specifications and Standards for Optical Coating Durability*. 08 2019. ISBN 9781510630482. doi:10.1117/3.2537932.ch1.

[183] Naiying Du, Gilles P. Robertson, Jingshe Song, Ingo Pinnau, Sylvie Thomas, and Michael D. Guiver. Polymers of intrinsic microporosity containing trifluoromethyl and phenylsulfone groups as materials for membrane gas separation. *Macromolecules*, 41 (24):9656–9662, 12 2008. doi:10.1021/ma801858d. URL `https://doi.org/10.1021/ma801858d`.

[184] Elena R. Dobrovinskaya, Leonid A. Lytvynov, and Valerian Pishchik. *Application of Sapphire*, pages 1–54. Springer US, Boston, MA, 2009. ISBN 978-0-387-85695-7. doi:10.1007/978-0-387-85695-7_1. URL `https://doi.org/10.1007/978-0-387-85695-7_1`.

[185] Bekir Karasu, Oğuz Bereket, Ecenur Biryan, and Deniz Sanoğlu. The latest developments in glass science and technology. *El-Cezeri*, 4(2):209–233, 2017. doi:10.31202/ecjse.318204.

[186] Lianqing Zheng, Ansgar W. Schmid, and John C. Lambropoulos. Surface effects on young's modulus and hardness of fused silica by nanoindentation study. *Journal of Materials Science*, 42(1):191–198, 2007. doi:10.1007/s10853-006-1051-2. URL `https://doi.org/10.1007/s10853-006-1051-2`.

[187] Xi Chen, Yong Xiang, and Joost J. Vlassak. Novel technique for measuring the mechanical properties of porous materials by nanoindentation. *Journal of Materials Research*, 21(3):715–724, 2006. doi:10.1557/jmr.2006.0088. URL `https://doi.org/10.1557/jmr.2006.0088`.

[188] Hamzah Bakhti, Ayoub Laghrissi, Artjom Roth, Lahcen Azrar, and Mohammed Es-Souni. Nanomechanical characterization and modeling of anodized porous aluminum oxide thin films with photografted anti-biofouling polymer brushes on their pore walls. *Applied Nanoscience*, 10(7):2139–2151, 2020. doi:10.1007/s13204-020-01338-6. URL `https://doi.org/10.1007/s13204-020-01338-6`.